Search for Higgs boson pair production in the two bottom quarks plus two photons final state in pp collisions at $\sqrt{s} = 13$ TeV with the ATLAS detector

PhD Thesis

Iván Sayago Galván

Supervised by:

Dr. Luca Fiorini

Dr. Arantxa Ruiz Martínez

VNIVERSITAT DE VALÈNCIA

Departamento de Física Atómica, Molecular y Nuclear and IFIC

(Universitat de València - CSIC)

Programa de Doctorado en Física

April 2022

Los Drs. **Luca Fiorini**, Profesor Titular de la Universitat de València del *Departament de Física Atòmica, Molecular i Nuclear*, y **María Aránzazu Ruiz Martínez**, investigadora Ramón y Cajal del CSIC y asociada de la Universitat de València del *Departament Unidad Experimental*

INFORMAN:

Que la presente memoria titulada ***"Search for Higgs boson pair production in the two bottom quarks plus two photons final state in*** *pp* ***collisions at*** $\sqrt{s} = 13$ ***TeV with the ATLAS detector"***, ha sido realizada bajo nuestra dirección en la *Universitat de València* por **Iván Sayago Galván** y constituye su Tesis para optar al título de Doctor por la Universitat de València una vez cursados los estudios en el Doctorado en Física.

Y para que conste, en cumplimiento de la legislación vigente, firmamos el presente Certificado en Paterna a 20 de abril de 2022.

FIORINI --- LUCA - X7825643P

Digitally signed by FIORINI --- LUCA - X7825643P
Date: 2022.04.20 12:21:33 +02'00'

Firmado por RUIZ MARTINEZ MARIA ARANZAZU - 20466644W el día 21/04/2022 con un certificado emitido por AC FNMT Usuarios

Dr. Luca Fiorini

Dra. María Aránzazu Ruiz Martínez

Abstract

Search for Higgs boson pair production in the two bottom quarks plus two photons final state in pp collisions at $\sqrt{s} = 13$ TeV with the ATLAS detector

Iván Sayago Galván

This thesis presents a physics analysis performed with the ATLAS detector at the Large Hadron Collider with data from the Run 2 (2015-2018) period of proton-proton collision at a center-of-mass energy of 13 TeV, corresponding to an integrated luminosity used for physics analyses of 139 fb^{-1}. The analysis is a search for resonant and non-resonant Higgs boson pair production in the $b\bar{b}\gamma\gamma$ final state. Special focus is given to the event selection strategy for the resonant search using multi-variate techniques. In addition, the ATLAS upgrade for the Run 3 (2022-2025) period where the software is migrated to a multi-threading framework is extensively covered along with the new read-out upgrade for the High-Luminosity LHC that will be tested during Run 3.

Acknowledgements

I would like to acknowledge and give my warmest thanks to both of my supervisors, Luca Fiorini and Arantxa Ruiz Martínez, who made this work possible. I am grateful that they have guided me and offered me the flexibility, independence and confidence that I needed to develop my work. I am particularly thankful to them for encouraging me to be part of the Tile Calorimeter community as Tile Run Coordinator, since it has been the best time of my thesis.

I am deeply thankful to the IFIC TileCal group that have integrated me. Big thanks to Alberto Valero Biot, Fernando Carrió Argos, Antonio Gómez Delegido, Ximo Poveda, Paco García and Leonor Cerdá Alberich. I am particularly thankful to Adam, who was the first person to knock my door and offered going to lunch, being since then the first friend that I met at IFIC. I would also like to thank Jesus, Luismi and Florencia for making me feel more comfortable at Valencia.

I am very grateful to one of the nicest teams in ATLAS, the TileCal collaboration. Thanks to Oleg Solovyanov and Henric Wilkens for trusting and guiding me during my stay as TileCal Run Coordinator. Big thanks to Jalal Abdallah, Filipe Martins, Tomas Davidek, Stan Nemecek, Irakli Minashvili, Siarhei Harkusha, Sasha Solodkov and many others for their knowledge, kindness and patience.

I am thankful to a very long list of $b\bar{b}\gamma\gamma$ colleagues, with whom I have shared a lot of work. I am thankful to my analysis contacts, Valentina Cairo, Elisabeth Petit, Louis D'Eramo and Adelina D'Onofrio. I am grateful for having had the opportunity to present my work in the group, for their advice and for trusting me to take responsibilities within the group. Big thanks to the rest of the analyzers, Raphaël Hulsken, Marc Escalier, Alex Wang, Elena Mazzeo, Jannicke Pearkes, Belfkir Mohamed and Tyler Burch among many others. I would also like to be thankful to the HH team and conveners, Katharine Leney, Liza Brost, Alessandra Betti and Jason Robert Veatch.

Finally, I would like to thank my family for loving and supporting me throughout all my life. Gracias a mi padre, y a mi madre, por creerme siempre en mi, por apoyar mis decisiones y por estar ahí siempre que lo he necesitado. Gracias a mi hermano, Abel,

por abrirme camino, apoyarme, entenderme y protegerme. Gracias a Mer por ser como una hermana para mi. Gracias a Azucena y su familia por acogerme, aportar compañía y alegría. Thanks to all.

Contents

Preface

The work presented in this thesis has been done with data delivered by the Large Hadron Collider (LHC). The LHC is the most powerful particle accelerator ever built in the world. It is a 27 km underground accelerator located on the French-Swiss border close to Geneva. Protons are accelerated inside its circular beampipe and collided close to the speed of light.

The Higgs boson was discovered in 2012 by the ATLAS and CMS experiments, and it explains why other elementary particles have mass. This achievement has provided the missing key piece to the Standard Model (SM) of particle physics, probing the validity of the Higgs mechanism of the electroweak Spontaneous Symmetry Breaking. However, the SM theory is not a complete theory. It unifies only three of the four fundamental interactions leaving gravity a part. One part of the present LHC program is to measure the properties of the Higgs boson and compare them to the theoretical predictions so that deviations in cross section measurements or measurements of the Higgs could point to new physics Beyond the Standard Model (BSM).

The "A Toroidal LHC ApparatuS" (ATLAS) experiment is one of the four main experiments that records the collisions delivered by the LHC. The work reported in this thesis has been carried out during the "Long Shutdown 2" where the LHC has been undergoing a series of upgrades. Since the start of Run 2 until the end, in 2018, ATLAS has recorded a dataset of 147 fb^{-1}, out of them 139 fb^{-1} are good for physics. The LHC is foreseen to deploy the upgrades for the High Luminosity LHC (HL-LHC) during the "Long Shutdown 3" between 2026 and 2028. During the operating period of the HL-LHC, ATLAS is expected to collect more than 3000 fb^{-1} of pp collisions, providing an unprecedented setup for the possible discovery of BSM physics.

Chapter 1 presents a review of the SM of particle physics and provides the framework needed to understand the content of the thesis. It describes the phenomenological aspects of the Higgs boson in proton colliders with an emphasis on di-Higgs production.

Chapter 2 is an introduction to the LHC at CERN with an overview of the ATLAS experiment providing special attention to the Tile Calorimeter.

Chapter 3 explains the algorithms and the different methodologies that are used in the ATLAS experiment to reconstruct and identify the particles that are produced in the pp collisions.

Chapter 4 describes the Tile Calorimeter upgrades performed for Run 3 and the ones that are currently in progress for the HL-LHC. It explains the contribution to the AthenaMT migration foreseen for Run 3. It also contains the contribution to the HL-LHC for which the updated electronic needs the development of new bytestream decoder for the new data format and the development of new monitoring algorithms.

Chapter 5 presents a search for Higgs boson pair production in the $b\bar{b}\gamma\gamma$ final state with data collected by the ATLAS detector during 2015-2018. The author of this thesis has contributed to the analysis as one of the main analyzers for the resonant search and served as a internal note editor.

Chapter 1

Theory

The present chapter describes the theoretical scheme to motivate and understand the contents of the thesis. It first introduces the Standard Model (SM) of particle physics, a theory that describes the behaviour of the subatomic world.

1.1 The Standard Model

The Standard Model [1–4] constitutes the most powerful theoretical framework capable of describing the subatomic world. The SM is able to describe with high precision most of the known experimental observations in particle physics.

The SM is a Quantum Field Theory (QFT) whose Lagrangian is invariant under local gauge transformations, a so called Yang-Mills theory [5], based on the Lie's symmetry group $SU(3)_C \otimes SU(2)_L \otimes U(1)_Y$, where C is the colour charge, L is the weak isospin and Y is the hypercharge. The SM describes the interaction of three of the four forces of nature via the exchange of spin-1 gauge fields. The strong and electromagnetic (EM) interactions are described by eight massless gluons and one massless photon respectively. The weak interaction is described by three massive bosons: $W^{\pm}$ and Z^0.

Fermionic matter content is given by leptons and quarks, which are divided in three families or generations of increasing mass. Each generation is composed of a doublet. Free fermions are described by spin 1/2 fields, solution of Dirac's Equation 1.1:

$$(i\partial\!\!\!/ - m)\psi(x) = 0 \tag{1.1}$$

All known ordinary matter is made up of the first generation of fermions in form of electrons and u and d quarks forming protons and neutrons. The second and third generations are unstable and decay into lighter particles. The properties of the three families can be seen in Table 1.1

Fermions (Spin = 1/2)						
	Leptons			Quarks		
Generation	flavour	Charge (e)	Mass	flavour	Charge (e)	Mass
1st	e	-1	0.511 MeV	d	-1/3	4.7 MeV
	ν_e	0	<2 eV	u	+2/3	2.2 MeV
2nd	μ	-1	105.658 MeV	s	-1/3	96 MeV
	ν_μ	0	<0.19 MeV	c	+2/3	1.28 GeV
3rd	τ	-1	1776.86 MeV	b	-1/3	4.18 GeV
	ν_τ	0	<18.2 MeV	t	+2/3	173.1 GeV

Table 1.1: Fermions in the SM: leptons, quarks and some of their basic properties. Neutrinos are considered massless in the SM as a first approximation although present results indicate that they have a very small but non-zero mass.

Each lepton generation doublet includes an electrically charged particle (ℓ) and a corresponding neutral particle (ν). Leptons are assigned a leptonic quantum number, 1 for leptons and -1 for anti-leptons. Excluding the phenomenon of neutrino oscillations [6], quantum numbers are conserved, therefore the total number of leptons of the same family must remain equal in any particle interaction. It means that lepton can only be created in lepton/anti-lepton pairs of the same family.

Quarks (q) have a fractional electric charge, each doublet is formed by a $+2/3$ electric charged up-type quark and a $-1/3$ electric charged down-type quark. The six different types of quarks that exist are referred to as flavours. Quarks have assigned a "colour" quantum number that can be understood as a conserved charge in the SM, as the electric charge. Each flavour of quarks can have any of the three different colours; red (R), green (G) and blue (B), so that there are actually triple the number of quarks shown in Table 1.1. Quarks also have their antiparticle, so called antiquark ($\bar{q}$) carrying the anticolours $\bar{R}, \bar{G}, \bar{B}$.

Four fundamental forces exist in nature, with strengths spanning several orders

of magnitude determined by their coupling constant. The gravitational force is not described by the SM, but it is too weak to have a significant role in elementary particle physics at the energy scale achievable by the Large Hadron Collider. The EM force is the responsible for the interaction between charged particles, as the attraction between electrons and atomic nuclei bonding atoms. The strong force is the responsible for binding quarks into protons and neutrons and also keeping them bonded forming nuclei even if protons electric charge would repel each other. The weak force is the mechanism of interaction between subatomic particles, responsible for the radioactive decay of atoms as the nuclear β-decay. The forces explained by the SM are described by gauge theories so that the exchanging bosons are called gauge bosons.

Table 1.2 shows the main properties of the gauge bosons and the Higgs boson.

Bosons					
Name	Spin	Charge (e)	Mass (GeV)	Force	Relative strength
Gluon, g	1	0	0	Strong	1
Photon, γ	1	0	0	Electromagnetic	10^{-2}
$W^{\pm}$	1	$\pm$ 1	80.385	Weak	10^{-13}
Z	1	0	91.188		
H	0	0	125.09		

Table 1.2: Gauge bosons and fundamental forces in the SM. Particle masses from Ref. [7].

1.1.1 Standard Model Lagrangian

The Standard Model Lagrangian is factorized in terms that describe the following interactions: the electroweak interaction, the Higgs sector interaction, the Yukawa coupling and the strong interaction:

$$\mathcal{L}_{\mathcal{SM}} = \mathcal{L}_{strong} + \mathcal{L}_{EW} + \mathcal{L}_{H} + \mathcal{L}_{Yukawa}. \tag{1.2}$$

In this subsection the components of the SM Lagrangian are going to be briefly described.

1.1.2 Strong interaction

Quantum Chromodynamics (QCD) is the theory of the strong interaction based on the $SU(3)_C$ gauge symmetry group. Gluons are the mediators of the strong force, gluons are massless, spin-1 bosons with zero electric charge. Gluons couple to particles with colour charge, and can mediate the interactions between quarks. Gluons are colour charged and therefore can interact with each other unlike photons. There is a total of eight gluons with different colours that can be defined from pairs of colour and anti-colour. There are two important properties of the strong interaction.

The asymptotic freedom states that the strong coupling constant g_s is weaker at greater energy scales so that perturbative theory is only applicable at high energies. The second property is the confinement and it states that quarks are always bound in colourless states called hadrons and cannot exist as isolated states. There are two types of hadrons depending on the number of quarks in the bound state. Mesons are composed of quark-antiquark pairs while baryons are composed of three quarks or three antiquarks.

The confinement implies that when quarks are pulled apart the interaction becomes stronger and therefore quark-antiquark (pairs) are created from the vacuum originating the hadronization process, which for instance can create jets as products of the proton-proton (pp) collisions at the LHC.

The QCD Lagrangian can be written in covariant notation as:

$$\mathcal{L}_{Strong} = \sum_q \bar{\psi}_{q,i}(i\not{D}_{ij} - m_q\delta_{ij})\psi_{q,j} - \frac{1}{4}G^a_{\mu\nu}G^{\mu\nu}_a, \tag{1.3}$$

where $\bar{\psi}_{q,i}$ is the fermion field of flavour q and colour i and the covariant derivative operator D^μ and the gluon fields kinetic terms of the strong tensor $G^a_{\mu\nu}$ are given by:

$$D^\mu = \partial_\mu + ig_s t^a G^a_\mu, \tag{1.4}$$

$$G^a_{\mu\nu} = \partial_\mu G^a_\nu - \partial_\nu G^a_\mu - g_s f^{abc} G^b_\mu G^c_\nu, \tag{1.5}$$

where g_s is the strong running coupling constant, t^a are the Gell-Mann matrices

generators of $SU(3)$ and the a index indicates the colour change and f^{abc} are the $SU(3)$ structure constants given by commutation relations between the group generators $[t^a, t^b]$ $= if^{abc}t^c$.

1.1.3 Electroweak interaction

In 1979 Glashow, Salam and Weinberg [8–10] were awarded the Nobel Prize for the electroweak theory which describes the electromagnetic and weak interactions between charged particles, based on the gauge symmetry $SU(2)_L \otimes U(1)_Y$.

The electromagnetic interaction is mediated by photons which are massless, neutral spin-1 bosons that couple only to electrically charged particles. Therefore quarks and charged leptons can interact electromagnetically but neutral particles cannot.

While the charged current of the weak interaction is mediated by the $W^{\pm}$ bosons in the transitions between up-type and down-type quarks or charged leptons and neutrinos, energy and angular distribution analyses of β-decays have shown that only left-handed (right-handed) fermion (antifermion) helicities can happen in charged current interactions and therefore the weak interaction violates parity. Neutral current weak interactions are mediated by Z bosons and conserve flavour. The $W^{\pm}$ and Z bosons can couple between them, also $W^{\pm}$ have electrical charge and therefore can couple with photons and interact electromagnetically with other charged particles.

The electroweak Lagrangian can be written as:

$$\begin{aligned}\mathcal{L}_{EW} = &\sum_{flavours} i(\bar{L}\not{D}L + \bar{Q}\not{D}Q + \bar{\ell}_R\not{D}\ell_R + \bar{u}_R\not{D}u_R + \bar{d}_R\not{D}d_R) \\ &- \frac{1}{4}B_{\mu\nu}B^{\mu\nu} - \frac{1}{4}W^a_{\mu\nu}W_a^{\mu\nu},\end{aligned} \tag{1.6}$$

Where $SU(2)_L$ is described by left-handed doublets (L for leptonic fields and Q for quark fields) and $U(1)_Y$ are hypercharged singlets (being u, d and ℓ right-handed quark and lepton fields). D is defined as the covariant derivative, $\not{D} = D^{\mu}\gamma_{\mu}$, where γ are the Dirac's matrices. Finally, $B_{\mu\nu}$ and $W^a_{\mu\nu}$ are the gauge field kinetic terms that can be defined as:

$$B_{\mu\nu} = \partial_\mu B_\nu - \partial_\nu B_\mu, \tag{1.7}$$

$$W^a_{\mu\nu} = \partial_\mu W^a_\nu - \partial_\nu W^a_\mu + g\epsilon^{abc} W^b_\mu W^c_\nu, \tag{1.8}$$

The four gauge bosons associated to $U(1)_Y$ and $SU(2)_L$ are B_μ and W^a_μ, respectively. ϵ^{abc} is the three dimensional Levi-Cita tensor and g is the coupling constant for the weak isospin. The covariant derivative from Equation 1.6 can be written in terms of the Pauli matrices τ^a, the hypercharge Y and the coupling constant for the weak hypercharge g' as:

$$D_\mu = \partial_\mu - \frac{1}{2} i g' Y B_\mu + \frac{1}{2} i g \tau^a W^a_\mu, \tag{1.9}$$

The hypercharge is fixed by the Gell-Mann-Nishijima relation $Y/2 = Q - T_3$, where Q is the electric charge and T_3 is the eigenvalue of the third component of the weak isospin. The terms that are proportional to the weak isospin are null since right-handed fermions are singlets under $SU(2)$.

1.1.4 Spontaneous Symmetry Breaking and Yukawa couplings

The gauge invariance in a Yang-Mills theory requires that mass terms for fermions and bosons should be null. Therefore all particles in a Yang-Mills theory have to be massless in contrast with experimental observations.

The solution is to introduce a Spontaneous Symmetry Breaking mechanism in the electroweak theory. This mechanism generates the mass of the weak vector bosons and preserves renormalizability and unitarity. It introduces a complex, colourless scalar doublet under $SU(2)$ field, ϕ.

The Higgs boson does not mediate any fundamental interaction, has no charge and no spin and its mass is $m_H \simeq 125$ GeV. The Higgs boson couples to any particle with mass including itself and is the only fundamental particle of spin-0. The Higgs field

contributes with the Lagrangian terms:

$$\mathcal{L}_H = (D_\mu \phi)^2 - \mu^2 \phi^2 - \lambda \phi^4, \tag{1.10}$$

where it is required that the mass term, $\mu^2 < 0$, and, the self-coupling constant,$\lambda > 0$ such that the ϕ field has non-vanishing vacuum expectation values given by:

$$v = \sqrt{\frac{-\mu^2}{\lambda}}. \tag{1.11}$$

This symmetry breaking mechanism is referred to as the Brout-Englert-Higgs (BEH) mechanism as it was independently developed by François Englert and Robert Brout and by Peter Higgs [11–13].

The transition to the Higgs field minimum is the responsible for the spontaneous symmetry breaking mechanism, resulting in massive weak bosons.

Since the lagrangian is gauge invariant, the Higgs field can be described using an exponential decomposition:

$$\phi(x) = \frac{1}{\sqrt{2}} e^{i\tau_a \theta^a(x)/f} \begin{pmatrix} 0 \\ \rho(x) \end{pmatrix} \tag{1.12}$$

where $\theta^a(x)$ and $\rho(x)$ are real fields, τ_a are the $SU(2)$ generators and f is a normalization constant. The Higgs field can be expanded breaking the vacuum symmetry around the minimum of the Higgs field ν. The expanded field can be written as:

$$h(x) \equiv \rho(x) - \langle \phi \rangle_0 = \rho(x) - \nu \tag{1.13}$$

Since the minimum is degenerated, the symmetry is broken when any particular minimum is chosen. The simplest way to expand the Higgs field is to keep the minimum number of degrees of freedom, therefore all θ^a are set to 0, resulting in:

$$\phi(x) = \frac{1}{\sqrt{2}} \begin{pmatrix} 0 \\ \nu + h(x) \end{pmatrix} \tag{1.14}$$

Using this representation of the Higgs field in Equation 1.10:

$$\begin{aligned}\mathcal{L}_H = & \frac{1}{2}\left(\partial_\mu h\right)\left(\partial^\mu h\right) + \frac{1}{2}\left(2\mu^2\right)h^2 \\ & + \frac{1}{2}\left(\frac{g_{\mathrm{W}}^2 v^2}{4}\right)\left(W_\mu^1 W^{1\mu} + W_\mu^2 W^{2\mu}\right) \\ & + \frac{1}{8}v^2\left(g_{\mathrm{W}} W_\mu^3 - g_{\mathrm{B}} B_\mu\right)\left(g_{\mathrm{W}} W^{3\mu} - g_{\mathrm{B}} B^\mu\right) \\ & + \mathcal{O}(h^2)\end{aligned} \tag{1.15}$$

Quadratic terms are interpreted as the mass term of the particle associated to the field. However, in Equation 1.15 the gauge boson terms are not linearly independent, therefore they cannot be interpreted as observables. In order to obtain the physical bosons, the fields are rewritten in a different representation, combining the physical gauge boson fields result in the mix of the $SU(2)_L \otimes U(1)_Y$ generators (B_μ, W_μ^0, W_μ^1 and W_μ^2) and the degrees of freedom of the scalar field H. Therefore, the generators can be rewritten as:

$$W_\mu^\pm = \frac{1}{\sqrt{2}}\left(W_\mu^1 \mp i\, W_\mu^2\right) \tag{1.16}$$

$$Z_\mu = \cos(\theta_{W_\mu})\, W^3 - \sin(\theta_{W_\mu}) B_\mu \tag{1.17}$$

$$A_\mu = \cos(\theta_{W_\mu})\, B \quad + \sin(\theta_{W_\mu}) W_\mu^3 \tag{1.18}$$

where θ_W is the Weinberg angle that is defined in terms of the coupling constants:

$$\tan\theta_W \equiv \frac{g_B}{g_W} \tag{1.19}$$

Using this definition, the Lagrangian can be written as:

$$\begin{aligned}\mathcal{L}_H(\mathcal{O}(h^2)) = &\frac{1}{2}\left(\partial_\mu h\right)\left(\partial^\mu h\right) + \frac{1}{2}\underbrace{\left(2\mu^2\right)}_{m_H^2} h^2 \\ &+ \frac{1}{2}\underbrace{\left(\frac{g_W^2 v^2}{4}\right)}_{m_{W+}^2} W_\mu^+ W^{+\mu} + \frac{1}{2}\underbrace{\left(\frac{g_W^2 v^2}{4}\right)}_{m_{W-}^2} W_\mu^- W^{-\mu} \\ &+ \frac{1}{2}\underbrace{\left(\frac{g_W^2 v^2}{4\cdot\cos\theta_W}\right)}_{m_Z^2} Z_\mu Z^\mu + \underbrace{0}_{m_\gamma^2}\cdot A_\mu A^\mu\end{aligned} \tag{1.20}$$

Where the terms of mass are the quadratic terms of the resulting Lagrangian, that can be rewritten as:

$$m_W^\pm = \frac{1}{2}vg, \quad m_Z = \frac{m_W}{cos\ \theta_W}, \quad m_\gamma = 0, \tag{1.21}$$

where $v = 246$ GeV is the Higgs field vacuum expectation value, g is the coupling constant for the weak isospin and θ_W is the Weinberg angle.

The two massive vector bosons $W^\pm$ correspond to the weak charged current, the other massive boson, Z, is the weak current-neutral carrier. The photon results in a massless gauge boson, superposition of B_μ and W_μ^0, that remains massless since the Quantum Electrodynamics (QED) symmetry $U(1)$ is still unbroken.

The mass term for the scalar field H is:

$$m_H^2 = 2\mu^2 \tag{1.22}$$

where the mass terms depend on the free parameter μ^2 that can be measured experimentally and have been done with LHC Run 1 and Run 2 data by ATLAS and CMS [14]:

$$m_H = 125.09 \pm 0.24 \text{ GeV} \tag{1.23}$$

The Brout–Englert–Higgs mechanism is used to give mass to the bosons but it can also be used to add mass terms for the fermions so that the gauge invariance is preserved.

We can add the Yukawa terms [15] to the EW Lagrangian resulting in:

$$\mathcal{L}_{Yukawa} = \sum_{flavours} (-\lambda_\ell \bar{L}\phi\ell_R - \lambda_d \bar{Q}\phi d_R - \lambda_u \epsilon^{ab}\bar{Q}_a\phi_b^\dagger u_R + h.c.), \tag{1.24}$$

where λ_e, λ_d and λ_u are arbitrary parameters and ϵ^{ab} is the two dimensional total anti-symmetric tensor with $\epsilon^{12} = 1$. After symmetry breaking we get the following mass terms for the fermion fields:

$$m_\ell = \lambda_\ell \frac{v}{\sqrt{2}},\ m_d = \lambda_d \frac{v}{\sqrt{2}},\ m_u = \lambda_u \frac{v}{\sqrt{2}}. \tag{1.25}$$

1.2 Proton-proton collisions at hadron colliders

In this section the production of particles through proton collisions is described, including the proton's composition, the parton model and the phenomenological aspects of the LHC *pp* collisions.

1.2.1 Phenomenology of LHC pp collisions

The proton is a complex object composed by valence quarks, sea quarks and gluons. Those constituents are called partons. The quantum numbers of a proton are defined by their valence quarks, being two up-quarks and one down-quark. The sea quarks are originated by vacuum fluctuations and therefore they are short living quark / anti-quark pairs that can interact with other partons in a *pp* collision.

The hard process of interest is defined as the interaction of two protons with a large momentum transfer. There are also soft low-momentum transfer interactions between the partons of each proton that travel along the proton direction. These interactions define the underlying event (UE). Multi-parton interactions (MPI), meaning more than one hard interaction in a single *pp* collision are also possible.

Bremsstrahlung is usually present in high energy collisions since accelerated colour and EM charges are present. The Initial State Radiation (ISR) are emissions associated with the incoming colliding partons while Final State Radiation (FSR) are the ones associated to the outgoing partons produced in the collision.

The strong interaction in a collision increases with the distance of the final state partons and therefore they are forced to be confined in a colourless state. This process is called hadronization and results in multiple collimated hadrons referred to as "jet".

The proton's initial momentum is divided among its partons. The form factors $f(x, Q^2)$ for each parton inside the proton are defined, where x is the fraction of momentum carried by the parton and Q^2 is the momentum transfer squared. These functions are called parton distribution functions (PDFs). The PDF is strongly x-dependent while a small dependence on Q^2 is observed [16]. PDFs are measured experimentally in deep inelastic scattering processes [17].

The probability of a given scattering process for a set of initial and final conditions is proportional to the cross section of the process. The cross section in a pp process can be divided in two parts: the perturbative QCD calculation in orders of g_s of the hard-scatter process and the parton model that describes the physics of the proton. The factorization scale μ_F is the scale Q^2 to separate the two components. The strong coupling constant g_s is small for the hard scattering process and therefore can be treated in an approximated way using perturbative Quantum Chromodynamics (pQCD) [18], which is an expansion of observables in orders of g_s. On the other hand, the soft part of a collision is defined by low momentum transfer and thus is a non-perturbative process which means that precise calculations are not possible.

In a pp interaction between proton A and B with a hard scattering process between partons a and b with a final state $X(ab \to X)$, the cross section can be written as:

$$\sigma_{AB} = \int dx_a dx_b f_{a/A}\left(x_a, \mu_F^2\right) f_{b/B}\left(x_b, \mu_F^2\right) \times \left[\sigma_0 + \hat{\alpha}_S\left(\mu_R^2\right)\hat{\sigma}_1 + ...\right]_{ab\to X}. \quad (1.26)$$

Where $f_{a/A}$ and $f_{b/B}$ are the PDFs containing the non-perturbative component of the soft interaction. The PDFs describe the probability that a parton a carries a fraction x_a of the momentum of proton A and depends on the non-physical factorization scale μ_F. The renormalization scale is also a non-physical factor μ_R that is dependent on the value at which g_s is computed. The variation of those scales for a fixed order provides the theoretical uncertainties of the cross section. The dependence is weaker with increased

orders of calculations and it would vanish if the cross section was calculated at all orders in the perturbation theory. The results obtained at leading order (LO) have larger uncertainties and higher-order corrections (next-to-leading order, NLO, or higher) are more significant. The K-factor is defined as the ratio between the NLO and LO cross sections.

1.2.2 Monte Carlo generators

A Monte Carlo (MC) event generator is a program that simulates the complexity of a high energy particle collision [19]. It is used to predict observables, such as particle momenta, masses, angular distributions, etc., which can be compared to data. It implements the different steps of a collision and is a fundamental part of any physics analysis.

The Matrix Element (ME) Monte Carlo, convoluted with the PDFs, generates a hard-scatter process of $2 \to n$, where n is any number of partons in the final state at a fixed order (LO, NLO, etc.) It also accounts for short-lived resonances, where the decays to stable particles are also performed with the decay widths and all other properties.

The Parton Shower (PS) simulates the emission of soft radiation and therefore adds effects of higher orders in the perturbation theory to the event generator. The PS process is non-perturbative and therefore less precise than ME. Parton Shower generators are also used to simulate FSR and ISR.

The hadronization process is defined by different phenomenological models, as the Lund string model [20] or the cluster model [21], and is implemented in the MC generators. Models are derived from experimental input and can be tuned to provide better data predictions.

Pile-up is usually threated by overlying $2 \to 2$ scatterings referred to as minimum bias events. Since this is a non-perturbative process as the hadronization, it relies on tuning from data.

1.3 The Higgs boson

1.3.1 Higgs boson production

In Figure 1.1 the main production, at tree level, modes of the Higgs boson at a pp collision are presented. Figure 1.2 shows the cross section of each production mechanism given by the LHC Cross Section Working Group, as a function of the centre-of-mass energy $\sqrt{s}$ for a Higgs boson mass $m_H = 125$ GeV.

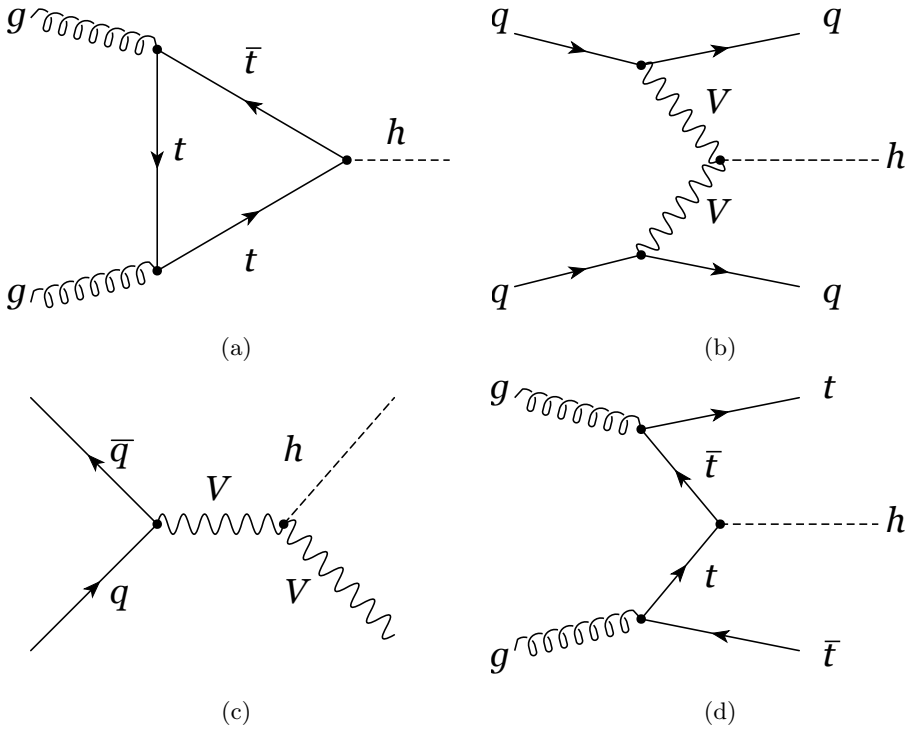

Figure 1.1: Leading-order Feynman diagrams of Higgs boson production modes, through a) gluon-gluon fusion via heavy quark loops, b) vector boson (W or Z) fusion with two forward jets, c) radiation of a Higgs boson (Higgs-strahlung) from a V (W or Z) boson and d) Higgs production in association with top quarks.

The main Higgs boson production channel at LHC at $\sqrt{s} = 13$ TeV is gluon-gluon fusion (ggF) representing the 87% of Higgs boson production. The cross section for ggF is known at Next-to-Next-to-Next-to-Leading-Order (N^3LO) [22] in QCD with soft gluon contributions up to NNLL with NLO EW corrections.

The second largest contribution to the Higgs boson production at $\sqrt{s} = 13$ TeV is vector boson fusion (VBF), responsible of 6.8% of the total cross section. The nature of this process is quite different from ggF since it involves the exchange of vector bosons

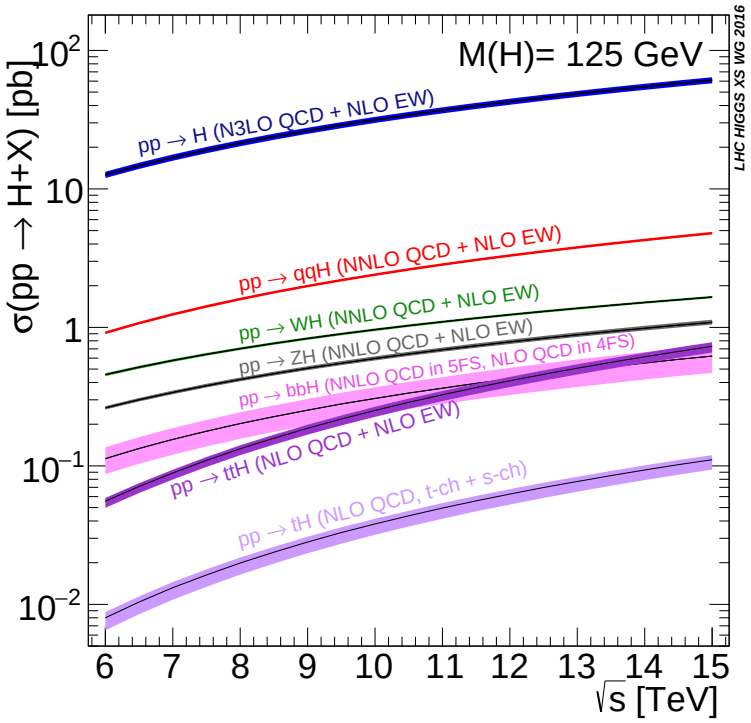

Figure 1.2: Cross sections for the different production mechanisms of the SM Higgs boson at the LHC, as a function of the centre-of-mass energy and for a Higgs boson mass of 125 GeV [22].

and has two hard jets in the forward region, while the Higgs is typically produced between the jets in the central region of the detector. The VBF cross section is known at NNLO in QCD and NLO in EW. This is an electroweak process and therefore the theoretical uncertainties are smaller than for ggF and the higher order corrections in QCD are less significant.

The third most common contributions are called Higgs-strahlung and are associated to vector boson (WH, ZH) providing a 4% of the Higgs boson production at $\sqrt{s} =$ 13 TeV. The cross section is calculated at Next-to-Next-to-Leading-Order (NNLO) in QCD and NLO in EW.

Top associated productions ($t\bar{t}H$ and tH) are one of the rarest production modes of the Higgs boson at $\sqrt{s} = 13$ TeV. The cross section is estimated at NLO in QCD and EW. This production mode provides direct access to the top Yukawa coupling.

An additional production mode of the Higgs boson is the associated with heavy fermions ($b\bar{b}H$), as top associated production modes, these modes have neither a sig-

nificant SM cross-section at LHC nor a clear signature, and due to the large b-quark background from QCD processes, their identification is troublesome.

1.3.2 Higgs boson decays

As mentioned in the Section 1.1.4, the coupling of the Higgs boson to fermions is proportional to the fermion mass. The interaction with fermions is linearly dependant with the fermion mass, while in boson interactions, HWW and HZZ vertices are proportional to m_W^2 and m_Z^2 respectively. Therefore, the decays of the Higgs boson to light particles is less probable than to heavier particles. Figure 1.3 shows the branching ratios of the SM Higgs boson decays for different values of the Higgs boson mass. This section is based on the Higgs boson branching ratios ($\mathcal{B}$) from [22] for a Higgs boson mass of $m_H = 125.09$ GeV.

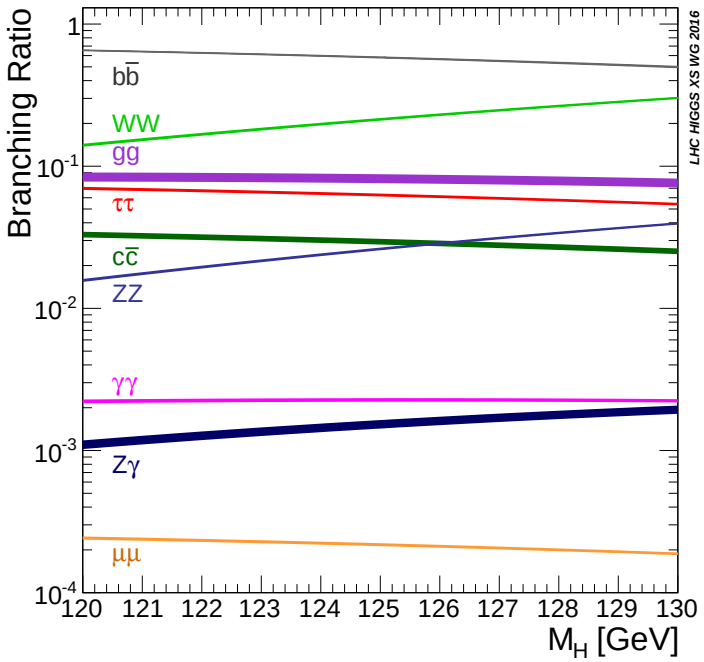

Figure 1.3: Branching ratios of the SM Higgs boson decays as a function of its mass [22].

The most abundant decay with $\mathcal{B}(H \to b\bar{b}) \approx 0.581$ is the $H \to b\bar{b}$ since the Higgs boson mass is below the W^+W^- production threshold. The fermionic decay channel $H \to \tau^+\tau^-$ with $\mathcal{B}(H \to \tau^+\tau^-) \approx 0.0626$ is the third dominant decay mode, these decay channels are useful to measure the Higgs boson coupling to different types of fermions.

The Higgs boson can also decay into gauge bosons, $H \to W^+W^-$ (where one of the W boson is off-shell) with $\mathcal{B}(H \to W^+W^-) \approx 0.215$, this decay is characterized by a poor mass resolution due to neutrinos in the final state. The Higgs boson also decays into $H \to ZZ$ with $\mathcal{B}(H \to ZZ) \approx 0.0264$ and is characterized by a very high signal to background ratio.

The Higgs boson can also decay into two photons $H \to \gamma\gamma$ via one-loop radiative transition with a virtual top-antitop quark pair that can also be replaced with a W boson loop. This decay has one of the lowest branching ratios $\mathcal{B}(H \to \gamma\gamma) \approx 0.227\%$ but is a very relevant decay in the Higgs boson studies of LHC, because of the good signal to background ratio compared to other decay modes. The Higgs boson can also decay into $H \to gg$ although it is not measurable directly at the LHC due to the overwhelming multijet background. Another Higgs boson decay is $H \to \bar{c}c$ with $\mathcal{B}(H \to \bar{c}c) \approx 0.02884$, but is difficult to measure since $\mathcal{B}(H \to \bar{b}b)/\mathcal{B}(H \to \bar{c}c) \approx 20$ and complex algorithms are required to differentiate between b-quarks and c-quarks. Finally, the decay mode $H \to \mu\mu$ has a $\mathcal{B}(H \to \mu\mu) \approx 0.02171\%$ and has not been observed experimentally yet. Diagrams for fermions and vector bosons can be seen in Figure 1.4.

1.3.3 Discovery and properties of the Higgs boson

Since there is no theoretical prediction of the Higgs boson mass in the SM, it needs to be measured experimentally. The lower bound of 114.4 GeV at 95% Confidence Level (CL) on the Higgs boson mass [23] was set by the combination of the data from the four detectors of the Large Electron-Positron collider. Later, TeVatron data was used to exclude masses between 100 and 109 GeV and between 158 and 175 GeV at 95% CL [24]. Finally the discovery of the Higgs boson was made using data from the Large Hadron Collider. ATLAS and CMS experiments presented the discovery of a particle with Higgs-like properties and a mass of approximately 125 GeV [25, 26] on July 4th 2012, as can be seen in Figure 1.5.

The decay channels $H \to \gamma\gamma$ and $H \to ZZ \to 4\ell$ provided the most precise measurement of the Higgs boson mass since the energy of all final state particles (photons, electrons and muons) can be measured with a very high precision and therefore the Higgs candidate can be fully reconstructed. The measured mass with the combination

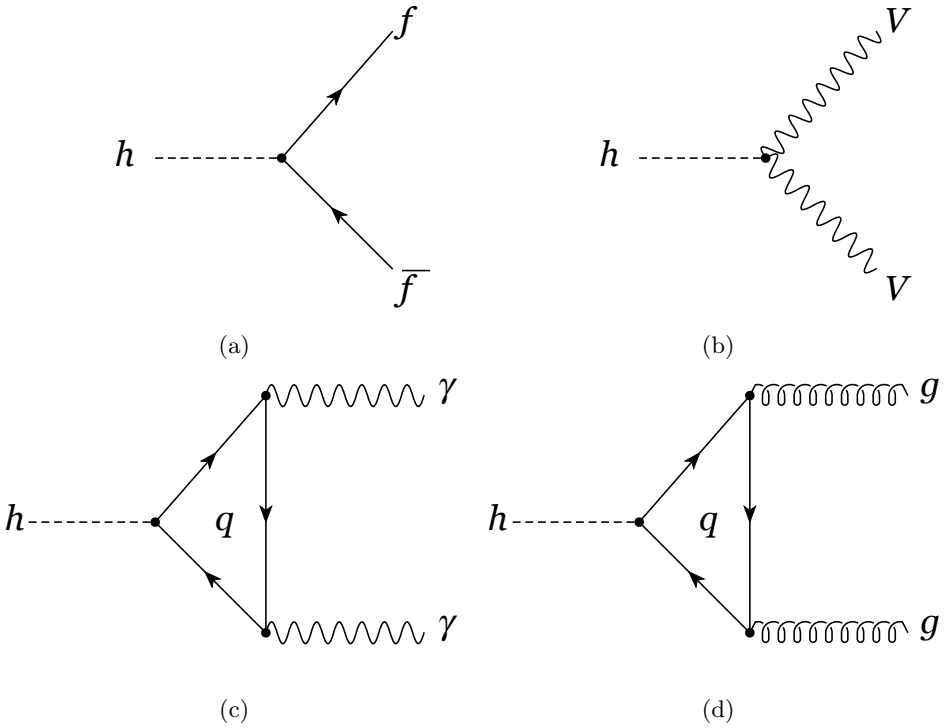

Figure 1.4: Feynman diagrams for the decay modes of the SM Higgs boson into: a) fermion-antifermion pairs, b) WW or ZZ spin-1 boson pairs, c) two photons via virtual quark loop (which can also be replaced with a W boson loop) and d) two gluons.

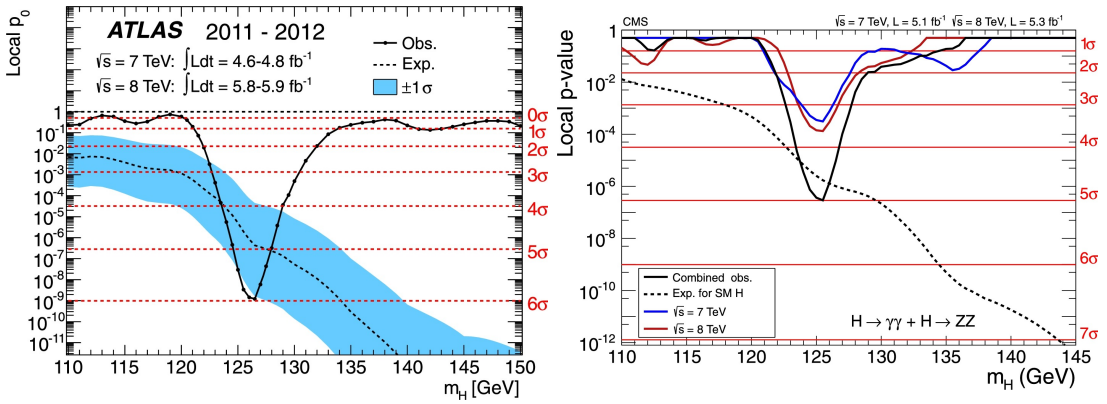

(a) (b)

Figure 1.5: The local probability p_0 measured by a) ATLAS [25] and b) CMS [26] for a background-only experiment to be more signal-like than the observation, for 7 and 8 TeV data and their combination in the low mass range of a) $110 < m_{\gamma\gamma} < 150$ GeV and b) $110 < m_{\gamma\gamma} < 145$ GeV. The full curve gives the observed combined p_0. The dashed curve shows the median expected value under the hypothesis of a SM Higgs boson signal at that mass. The horizontal lines indicate the p_0 corresponding to different significances.

of these decay channels, with the ATLAS and CMS experiments using the Run 1 dataset was found to be:

$$m_H = 125.09 \ \pm 0.21\,(\text{stat.}) \pm 0.11\,(\text{syst.}). \tag{1.27}$$

The ATLAS and CMS collaborations also combined results to measure the production and decay modes of the Higgs boson using the Run 1 data set. This measurement is usually presented in terms of the signal strength that is defined for each production and decay mode as:

$$\mu = \frac{\sigma \times \mathcal{B}}{\sigma_{SM} \times \mathcal{B}_{SM}}, \tag{1.28}$$

Where $\sigma \times \mathcal{B}$ is the measured cross section times branching ratio and $\sigma_{SM} \times \mathcal{B}_{SM}$ is the SM expectation. The production modes considered were ggF, VBF, WH, ZH and $t\bar{t}H$ and the decay modes were ZZ, $\gamma\gamma$, W^+W^-, $\tau^+\tau^-$ and $b\bar{b}$. It is only possible to measure individual production modes if we assume that the decay modes are equal to their SM expectations. Similarly, measurements of individual decay modes are only possible if we assume that the production modes are equal to their SM expectations. The combined results from ATLAS and CMS for the production and decay signal strengths can be seen in Figures 1.6 and 1.7 using the Run 1 data set. All measurements are found to be in good agreement with their SM predictions being the measured combined signal strength $\mu = 1.09 \pm 0.11$ [27].

1.3.4 Higgs boson pair production

The simplest production process that is sensitive to the self-coupling constant λ is the Higgs boson pair production [28]. It also provides the possibility of probing higher dimensional interactions and the existence of heavier states coupled to the Higgs boson. Therefore it plays a very important role that would allow the understanding of the potential that results from the BEH spontaneous symmetry breaking mechanism.

The SM predictions of Higgs boson pair production rates are very low at the LHC centre of mass energy of $\sqrt{s} = 13$ TeV and therefore it is needed a very high integrated luminosity to observe them. However, searches for Higgs boson pair production are

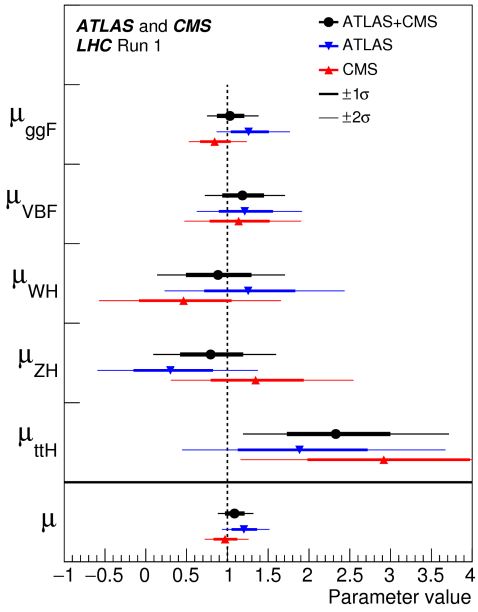

Figure 1.6: Best fit results for the production signal strengths for the combination of ATLAS and CMS data. Also shown are the results from each experiment. The error bars indicate the 1σ (thick lines) and 2σ (thin lines) intervals. The measurements of the global signal strength μ are also shown [27].

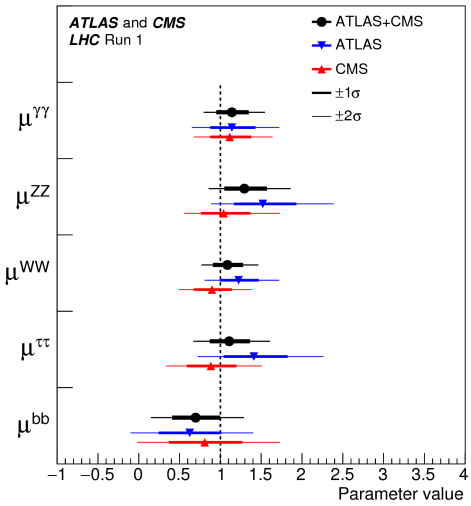

Figure 1.7: Best fit results for the decay signal strengths for the combination of ATLAS and CMS data. Also shown are the results from each experiment. The error bars indicate the 1σ (thick lines) and 2σ (thin lines) intervals [27].

still relevant since deviations from the SM could produce sizeable enhancements in the production rate. There are two possibilities to enhance the production rate: non-resonant and resonant production.

There are several production channels that could lead to a final state with two Higgs bosons. The dominant production modes are the gluon gluon fusion via virtual top quarks in a box and the triangle diagrams, as can be seen in Figure 1.8. Of these two, only the triangle production mode has dependence on the Higgs self-coupling λ. Other channels cross section are at least one order of magnitude smaller, although they provide different sensitivity to λ and to new physics.

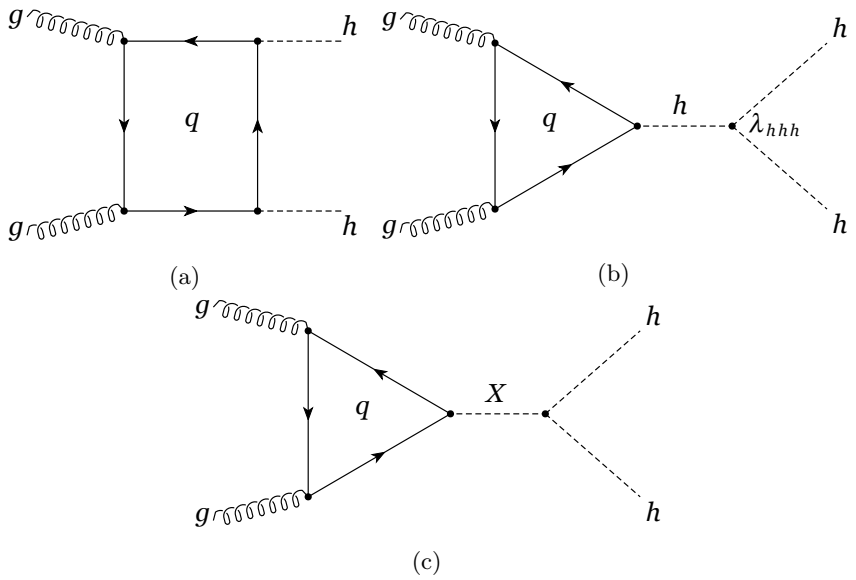

Figure 1.8: Feynman diagrams for the leading order production modes for SM Higgs boson pair production through: a) a heavy quark loop ("box diagram") and b) the Higgs boson self-coupling ("trilinear diagram"). BSM Higgs boson pair production can occur by changing the SM couplings in a) and b) or through c) an intermediate particle, X.

The rate predictions at NLO for all the relevant Higgs boson pair production modes in the SM as a function of the centre-of-mass energy can be seen in Figure 1.9 for values of 8 TeV $< \sqrt{s} <$ 100 TeV. The thickness of the curves represents the scale and PDF uncertainties. As opposed to the single Higgs case, the top-pair associated channel becomes the third largest production mode at $sqrts$ = 10 TeV, becoming the second largest to at $sqrts$ = 100 TeV. The theoretical uncertainties in the most important processes (ggF, VBF and associated production) are reduced by NLO corrections.

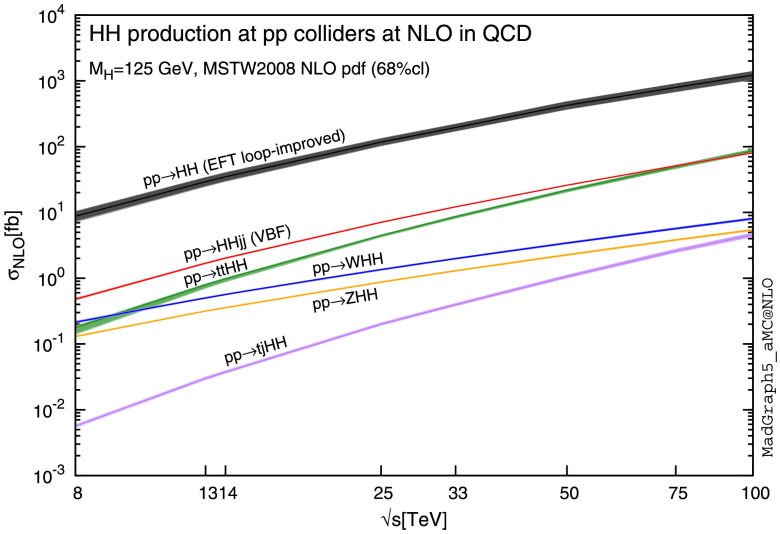

Figure 1.9: Total cross sections at the NLO in QCD for the six largest HH production modes at pp colliders [28]. The bands denote the scale and PDF uncertainties.

Figure 1.10 shows the branching ratio of the Higgs boson pair decay channels assuming that $m_H = 125.09$ GeV [22]. Among the several searches for Higgs boson pair production, the $HH \to b\bar{b}b\bar{b}$ final state exploits the high rate of the $H \to b\bar{b}$ decay but has a very large multijet background. This final state provides the highest sensitivity for high resonance masses. The $HH \to b\bar{b}\ell\ell$ final state includes $HH \to b\bar{b}W(\ell\nu)W(\ell\nu)$, $HH \to b\bar{b}Z(\ell\ell)Z(\nu\nu)$ and $HH \to b\bar{b}\tau^+(\ell\nu)\tau^-(\ell\nu)$ signals, in both cases there are neutrinos in the final state that degrades the invariant mass resolution on the Higgs boson. For this decay mode the most relevant background is the top-quark pair production decaying leptonically. The $HH \to b\bar{b}\tau\tau$ provides a good compromise between the branching ratio and the background rejection. It also contains neutrinos in the final state which provides a poor $m_{b\bar{b}\tau\tau}$ resolution. For this search the main backgrounds are $t\bar{t}$, Drell-Yan and multijet production. The $HH \to b\bar{b}\gamma\gamma$ channel provides a very high signal purity since $H \to \gamma\gamma$ reduces the multijet background, and it is combined with $H \to b\bar{b}$ to have larger yields.

1.3.5 Resonant production

Many BSM theories predict the existence of heavy particles decaying into a Higgs boson pair that can be seen as resonances in the Higgs boson pair invariant mass spectrum.

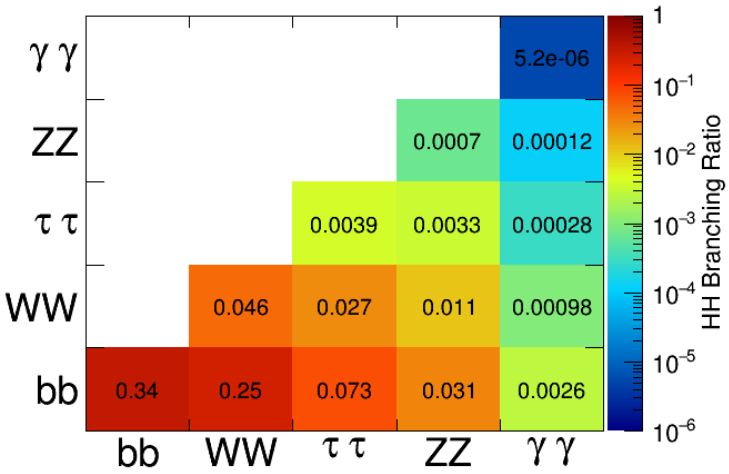

Figure 1.10: Branching ratios of the most relevant HH decay channels given a Higgs boson mass of 125.09 GeV.

There are several models with two Higgs boson doublets [29], as the minimal supersymmetric extension of the SM (MSSM) [30], composite boson Higgs models [31, 32] which involve an additional complex scalar doublet or the twin Higgs boson model [33]. Figure 1.8c shows a possible production mode of a resonance through the ggF process, where "X" would be a new intermediate boson.

Two-Higgs-doublet model

One of the simplest extensions of the SM are the two Higgs doublet models (2HDM). They consist in adding a second Higgs boson doublet which leads to five physical scalar states: the CP-odd pseudoscalar A, two charged Higgs bosons $H^{\pm}$ and the CP-even neutral Higgs bosons h and H (being H heavier than h). This model assumes that the discovered Higgs boson of $m_H = 125$ GeV is the lightest CP-even neutral Higgs boson h.

The couplings of the light boson h are SM-like in the alignment limit $\beta - \alpha = \pi/2$, where tanβ is the ratio between the vacuum expectation value ν and α is the mixing angle of the two CP-even neutral Higgs bosons.

The Glashow-Weinberg condition that requires that each group of fermions couples to one of the two doublets is sufficient to avoid flavour-changing neutral currents that

the Two-Higgs-doublet model can introduce.

Two-Higgs-doublet models are divided in classes according to the fermions couplings with the double ϕ as is stated in Table 1.3.

Type	Description	u-type quarks couple to	d-type quarks couple to	Charged leptons couple to
Type I	Fermiophobic	ϕ_2	ϕ_2	ϕ_2
Type II	MSSM-like	ϕ_2	ϕ_1	ϕ_1
X	Lepton-specific	ϕ_2	ϕ_2	ϕ_1
Y	Flipped	ϕ_2	ϕ_1	ϕ_2

Table 1.3: Classification of Two-Higgs-doublet models which lead to a natural flavour conservation. By convention, ϕ_2 is the doublet to which up-type quarks couple [34].

1.3.6 Non-resonant production

For the gluon-gluon fusion processes shown in Figure 1.8 both the box and trilinear diagrams are dominant HH production mechanisms. The amplitude of the interference of both production mechanisms is sensitive to the HHH coupling and therefore modifying any SM couplings would vary the Higgs boson pair production rate. If the self-coupling constant $\lambda_{HHH} = 0$ the Higgs boson pair production rate would be doubled in the ggF channel and changing its sign would quadruplicate it [35].

The maximum destructive interference of the amplitudes are at $\lambda_{HHH} \approx 2.45\lambda^{SM}_{HHH}$. Total LO and NLO cross sections of the dominant Higgs boson pair production channels at LHC for $\sqrt{s} = 13$ TeV are shown in Figure 1.11 as a function of the self-coupling λ. The dashed (solid) lines and light (dark) colour bands correspond to the LO (NLO) results and to the PDF uncertainty added linearly. The SM value corresponds to $\kappa_\lambda = \lambda/\lambda_{SM} = 1$.

1.3.7 ATLAS searches for Higgs boson pair production

The ATLAS collaboration has performed searches for resonant and non-resonant Higgs boson pair production in the $b\bar{b}b\bar{b}$, $b\bar{b}WW$, $b\bar{b}\tau\tau$, $WWWW$, $WW\gamma\gamma$ and $b\bar{b}\gamma\gamma$ final states using the Run 2 data set at a centre-of-mass energy of $\sqrt{s} = 13$ TeV. These searches are combined and no evidence of HH production has been found [36] in neither the resonant nor the non-resonant search.

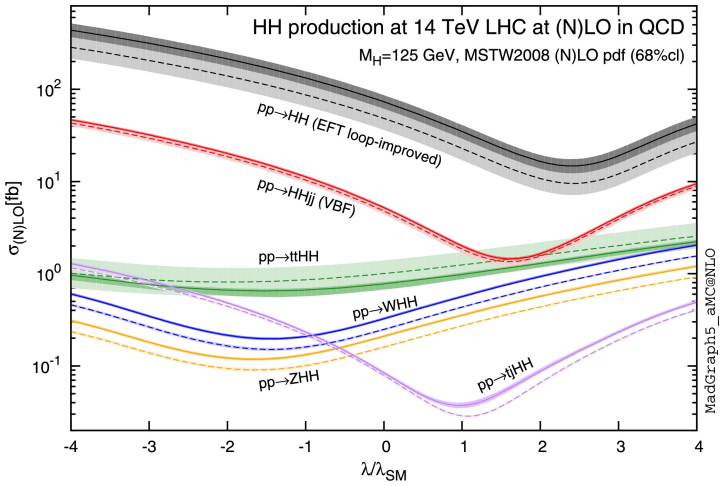

Figure 1.11: Total cross sections at LO and NLO in QCD for HH production modes, at the $\sqrt{s}$ = 14 TeV LHC as a function of the self-interaction coupling constant λ [28].

Figure 1.12 shows the combined and expected upper limits at 95% CL on the resonant production cross section as a function of the resonance mass m_s with 27.5-36.1 fb^{-1} of $\sqrt{s} = 13$ TeV of data. In the low mass region 260-500 GeV, the $b\bar{b}\tau\tau$ and $b\bar{b}\gamma\gamma$ channels show the highest sensitivity, while for resonance masses above 500 GeV the $b\bar{b}b\bar{b}$ final state takes the lead being the most sensitive channel among all.

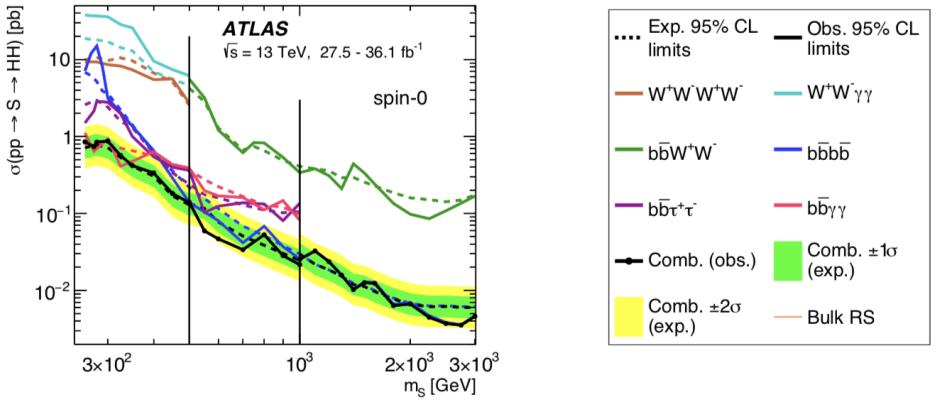

Figure 1.12: The combined observed and expected 95% CL upper limits on the resonant production cross section, $\sigma\ (g\text{-}g \to X) \times \mathcal{B}\ (X \to HH)$ as a function of m_S. The expected limits from the individual analyses are also shown [36].

In the combination, there is no significant deviation from the background expectation for the mass range of 260-3000 GeV. Systematic uncertainties have a sizeable

effect on the upper limits depending on the probed resonance mass. The total impact of systematics or the impact of a single systematic uncertainty are evaluated by computing the percentage reduction of the upper limit obtained by removing all systematic uncertainties or a particular source. Overall the systematic uncertainties affect the limit by 12% (11%) for a resonance mass of 1 (3) TeV.

For the non-resonant search using 27.5-36.1 fb^{-1} of $\sqrt{s} = 13$ TeV data, the observed and expected upper limits at 95% CL on the cross section of SM Higgs boson pair production are shown for each individual analysis and for the combination in Table 1.4. The combined observed (expected) upper limit on σ ($gg \to HH$) is 6.9 (10) times the cross section predicted by the SM. Upper limits on the $pp \to HH$ cross-section are also computed as a function of the Higgs boson self-coupling modifier $\kappa_\lambda = \lambda_{HHH}/\lambda_{SM}$, by combining the $b\bar{b}b\bar{b}$, $b\bar{b}\tau\tau$ and $b\bar{b}\gamma\gamma$ final states. The combination excludes κ_λ values outside the range $5.0 < \kappa_\lambda < 12.0$ ($5.8 < \kappa_\lambda < 12.0$) at 95% confidence level in observation (expectation) as shown in Table 1.5. The $HH \to b\bar{b}b\bar{b}$ analysis has the best expected sensitivity followed by the $HH \to b\bar{b}\gamma\gamma$ analysis.

For comparison, the CMS combination [37] of the final states $b\bar{b}\gamma\gamma$, $b\bar{b}\tau\tau$, $b\bar{b}b\bar{b}$ and $b\bar{b}VV$ performed with LHC pp collisions at $\sqrt{s} = 13$ TeV, corresponding to an integrated luminosity of 35.9 fb^{-1}, obtains a 95% CL observed (expected) upper limit on the non-resonant HH production cross section of 22.2 (12.8) times the SM value. The combination excludes κ_λ values outside the range $11.8 < \kappa_\lambda < 18.8$ ($7.1 < \kappa_\lambda < 13.6$) at 95% CL in observation (expectation).

Analysis	$b\bar{b}\tau\tau$	$b\bar{b}b\bar{b}$	$b\bar{b}\gamma\gamma$	$WWWW$	$WW\gamma\gamma$	$b\bar{b}WW$	Combination
Upper limit on the cross section normalised to its SM expectation at 95% CL							
Observed	12.5	12.9	20.3	160	230	305	6.9
Expected	15	21	26	120	170	305	10
Expected Stat	12	18	26	77	160	240	8.8

Table 1.4: The expected and observed 95% CL upper limits on the cross sections of non-resonant Higgs boson pair production at $\sqrt{s} = 13$ TeV from the individual ATLAS analyses and their combinations. SM values are assumed for the Higgs boson decay branching ratios. The cross section limits normalized to the SM value are also included [36].

Analysis	$b\bar{b}b\bar{b}$	$b\bar{b}\tau\tau$	$b\bar{b}\gamma\gamma$	Combination
Allowed κ_λ interval at 95% CL				
Observed	-10.9 - 20.1	7.4 — 15.7	8.1 — 13.1	5.0 — 12.0
Expected	11.6 — 18.8	8.9 — 16.8	8.1 — 13.1	5.8 — 12.0
Expected Stat	9.8 — 16.3	7.8 — 15.5	7.9 — 12.9	5.3 — 11.5

Table 1.5: The expected and observed 95% CL upper limits on the cross sections of non-resonant Higgs boson pair production at $\sqrt{s} = 13$ TeV from the individual ATLAS analyses and their combinations. SM values are assumed for the Higgs boson decay branching ratios. The cross section limits normalized to the SM value are also included [36].

1.3.8 Implication of the Higgs boson discovery

The Standard Model is capable of describing and predicting the behaviour of the subatomic world with the highest precision ever reached. However, the SM is still a theory that is far from complete as it cannot describe the gravitational interaction and there are fundamental problems that require searches for new Physics Beyond the Standard Model. Some examples are the dark matter and dark energy phenomena [38], which compose the 96% of the Universe or the matter-antimatter asymmetry that is still unexplained by the SM.

The discovery of the Higgs boson has theoretical consequences, being the most relevant one the hierarchy problem, related to the tuning of the free parameters of the SM. Higgs boson mass is quadratically divergent with one-loop radiative corrections, which makes the Higgs boson heavier. If new particles are found at the TeV scale it would cancel the divergences reducing the needed tuning.

An important part of the LHC effort for these years has been to measure properties of the Higgs boson with greater precision and to compare them with the theoretical predictions. New physics can be found in deviations in cross section measurements and Higgs boson couplings and self-coupling measurements among others.

Chapter 2

The LHC and the ATLAS experiment

In this chapter the experimental setup needed for the analysis of this thesis is presented. The CERN research complex and the LHC machine delivering pp collisions are described. The ATLAS detector and its sub-systems are then described.

2.1 Conseil Européen pour la Recherche Nucléaire (CERN)

CERN is the European research organization operating the largest particle physics laboratory in the world. It was established in 1954 and is based in the northwest side of Geneva close to the Franco-Swiss border. Currently it is supported by 23 member states.

It is home of more than two thousand scientific, technical and administrative staff members and host of more than thirteen thousand users from more than 70 countries, being the biggest scientific community of the world.

Since its foundation, CERN has achieved several discoveries. In 1973 the neutral currents in the Gargamelle bubble chamber were discovered [39, 40], ten years later the UA1 and UA2 experiments observed the W and Z bosons [41]. In 1995 the first antihydrogen atoms were created in the PS210 experiment [42]. In 1999 the direct CP

violation in the NA31 experiment was observed [43]. In 2010 the PS210 experiment was capable of isolate 38 antihydrogen atoms [44] and in 2011 antihydrogen was maintained stable for 15 minutes [45]. In 2012 a Higgs boson with a mass of 125 GeV was first observed [46, 47].

Several of these discoveries have been awarded with the Nobel Prize. In 1984 S. Van Der Meer was given the Nobel Prize for the technique of stochastic cooling of particle beams and C. Rubbia for the discovery of the carriers of the weak interaction. In 1992 G. Charpak for the drift chamber for particle detection. Finally in 2013 P. Higgs and F. Englert for the theorization of the Brout-Englert-Higgs field.

It is also home of several non-particle physics achievements being the development of the World Wide Web the most renown one or the invention of touch screens, but also many other programming challenges and developments have been achieved at CERN.

2.2 The Large Hadron Collider

Located at CERN, the Large Hadron Collider (LHC) [48] is an underground two-ring-superconducting-hadron accelerator and collider. It is approximately circular with a circumference of 27 km that crosses the border between France and Switzerland outside Geneva. It delivers pp collisions at unprecedented conditions of energy and luminosity that allows the exploration of the Standard Model in the TeV energy scale, searching for the Higgs boson and for possible new physics beyond the Standard Model.

Protons are injected into the LHC in different steps following a chain of particle accelerators. First, hydrogen atoms are ionized, the protons are accelerated up to 50 MeV by the linear accelerator LINAC. They are injected in the Proton Synchrotron Booster (PSB) followed by the Proton Synchrotron (PS) and the Super Proton Synchrotron (SPS) accelerating the protons to energies of 1.4 GeV, 26 GeV and 450 GeV, respectively. The LHC injection chain can be seen in Figure 2.1. Protons are delivered in bunches by the PS and SPS. They are separated by 25 ns and a total of 2808 bunches can be injected into the LHC ring. There is about 10^{11} protons in each bunch. Inside the LHC, proton bunches are kept circulating using superconducting magnets cooled to 1.9 K with liquid helium. Particles are accelerated from 450 GeV to 7 TeV using

radiofrequency (RF) cavities with a maximum frequency of 400 MHz.

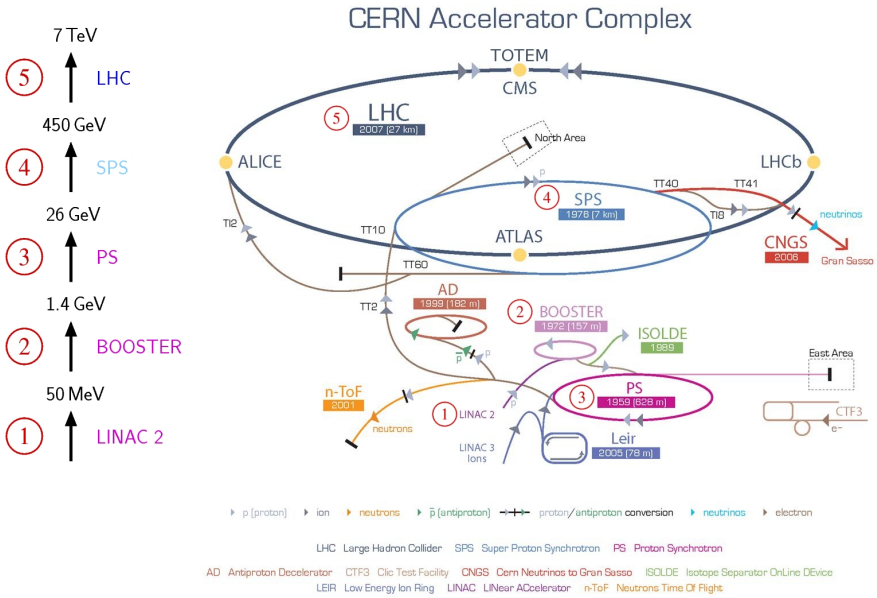

Figure 2.1: The Large Hadron Collider, its injection chain, and the four main experiments, ATLAS, ALICE, CMS, and LHCb, to which it delivers collisions [49].

The LHC is composed of eight arcs and eight straight sections between the arcs. Straight sections are 528 meters long. Each straight section connects the surface with the underground installations with lifts. These locations are defined as the LHC points. The four main experiments are situated at point 1 (ATLAS), point 2 (ALICE), point 5 (CMS) and point 8 (LHCb). The injection of clockwise (anti-clockwise) beam takes place at point 2 (8). Main collimators are installed at points 3 and 7, the beam dump system is situated at point 6 and the Radio-Frequency (RF) system can be found at point 4 as shown in Figure 2.2. Each one of the different sectors of LHC can be cooled and powered independently.

The instantaneous luminosity is defined as the number of pp interactions per second and unit of surface area. It can be written in terms of the beam parameters:

$$L = \frac{1}{4\pi} \frac{N^2 \, f_{\text{rev}} \, n_{\text{bunch}}}{\sigma_x \sigma_y} \sim 10^{34} \text{ cm}^{-2} \text{ s}^{-1}, \tag{2.1}$$

where in the context of the LHC, $N = 10^{11}$ is the number of protons per bunch, $f_{rev} = 11245$ Hz is the LHC revolution frequency, $n_{\text{bunch}} = 2808$ is the number of

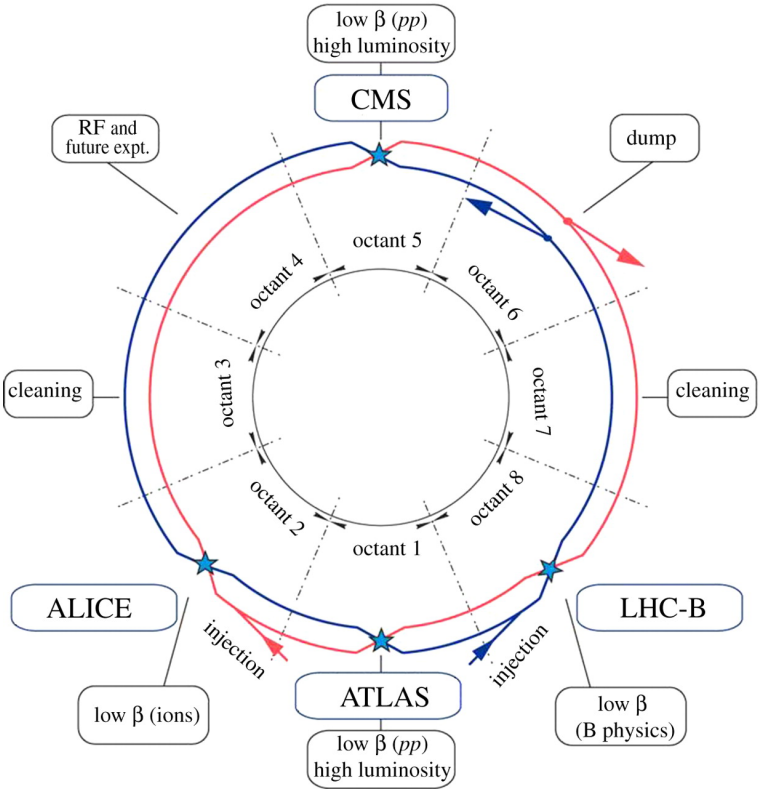

Figure 2.2: Layout of the main LHC ring [50].

bunches and σ_x and σ_y are the dimensions of the bunch, which is of the order of μm at the ATLAS interaction point (IP).

Figure 2.3 (a) reports the integrated luminosity delivered to ATLAS in each year of data taking from 2011 to 2018, and Figure 2.3 (b) shows the cumulative luminosity delivered to and recorded by ATLAS during the years 2015-2018. LHC design luminosity $1 \times 10^{34}\text{cm}^{-2}\text{s}^{-1}$ was already exceeded in 2016 and doubled during 2017 and 2018.

A consequence of a high instantaneous luminosity is that the mean number of inelastic *pp* collisions in a single bunch crossing in one of the IPs is larger than one. This effect is known as "pile-up". The mean number of interactions in each bunch crossing is the mean of the Poisson distribution on the number of interactions per crossing for each bunch. It is dependent on the instantaneous per bunch luminosity:

$$\mu = \frac{L_{\text{bunch}}\ \sigma_{\text{inel}}}{f_{\text{rev}}}, \tag{2.2}$$

where L_{bunch} is the per bunch instantaneous luminosity, σ_{inel} is the inelastic cross

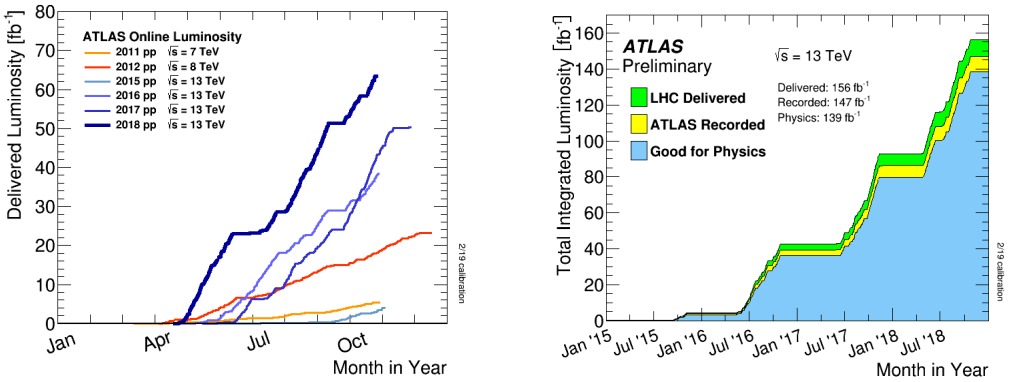

(a) (b)

Figure 2.3: a) Cumulative *pp* collision luminosity delivered to the ATLAS detector versus month of the year, separately for years between 2011 and 2018 and b) cumulative luminosity versus time delivered by the LHC (green), recorded by ATLAS (yellow) and used for physics (blue) during stable beams for *pp* collisions at 13 TeV centre-of-mass energy in years 2015-2018 [51].

section that is 80.0 mb for 13 TeV collisions [52], and f_{rev} is the LHC revolution frequency.

Figure 2.4 shows the distribution of the mean number of interactions per bunch crossing in ATLAS for the 2015-2018 data taking periods. The combined mean number of interactions per crossing is $\langle\mu\rangle = 33.7$ with tails up to 70.

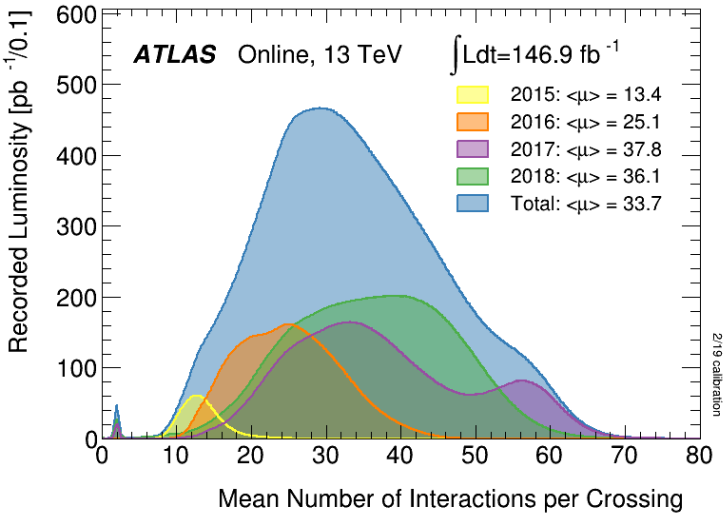

Figure 2.4: Luminosity-weighted distribution of the mean number of interactions per crossing for the 2015-2018 *pp* collision data at 13 TeV centre-of-mass energy [51].

2.3 The ATLAS experiment

ATLAS (A Toroidal LHC Apparatus) [53] is a general purpose detector that is designed to reconstruct the events that result from colliding hadronic particles at the LHC. It is 44 meters long, more than 25 meters high and wide and weights approximately 7000 tonnes. The detector is built with cylindrical symmetry that provides coverage of almost 4π solid angle.

The ATLAS detector is designed to measure the momentum of charged particles, the energy and momentum of electromagnetically interacting particles (electrons and photons), hadronic jets and muons. The detector is composed of several cylindrical sub-system as can be seen in Figure 2.5. From inside-out, the tracking system measures the momentum of charged particles while is trying to absorb as little of the particle's energy as possible. Next is a system of calorimeters that stops the electrons, photons and hadronic jets while measuring their energy in the process. The electromagnetic calorimeter is closer to the IP and absorbs almost all the energy from electrons and photons. The hadronic jets are stopped by both the electromagnetic and hadronic calorimeters.

Muons escape both calorimeters and reach the outermost layer of the ATLAS detector which is composed by tracking detectors and toroidal magnets that measure muons' momentum.

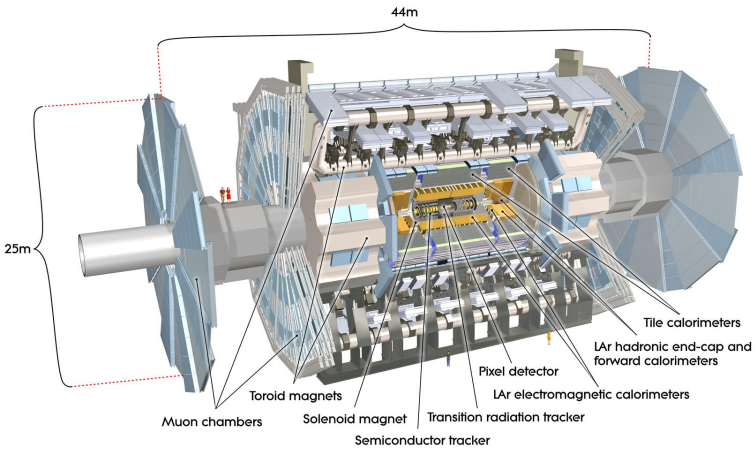

Figure 2.5: Cut-away view of the ATLAS detector [53].

ATLAS coordinate system is based on the beam direction that defines the z-axis and is centered at the IP. The A-side of the detector is defined as the positive z while the C-side by the negative. The positive x-axis is defined pointing to the centre of the LHC ring and the positive y-axis points upwards. So that the $x-y$ plane is orthogonal to the beam direction and defines the transverse plane. The projection of quantities as the momentum p over the transverse plane are defined as transverse momentum p_{T}. The azimuthal angle ϕ is defined around the beam axis and the polar angle θ is the angle from the beam axis. The rapidity y and pseudorapidity η are defined as:

$$y = \frac{1}{2}\ln\left(\frac{E+p_z}{E-p_z}\right) \text{ and } \eta = -\ln\left(\tan\left(\frac{\theta}{2}\right)\right), \tag{2.3}$$

where E denotes the energy and p_z the component of the momentum along the beam direction. The rapidity is invariant under Lorentz boosts along the beam axis. In the limit of massless particles, the rapidity y reduces to the pseudorapidity η. The distance ΔR in the $\eta-\phi$ coordinate space is commonly used and is defined as:

$$\Delta R = \sqrt{\Delta\eta^2 + \Delta\phi^2}. \tag{2.4}$$

2.3.1 Inner Detector

Figure 2.6 shows the Inner Detector, which is the innermost layer of ATLAS [53]. This detector is composed of three different sectors that decrease in granularity as we move outward from the interaction point. The closest one to the interaction point is the Pixel detector and is composed by four layers of silicon pixel detectors. The second innermost detector is the Semi-Conductor Tracker (SCT) and is built by four layers of silicon strips. The outermost layer is the Transition Radiation Tracker (TRT) formed by straw tubes.

The Pixel and SCT detectors are divided along the beam axis into a barrel region and two end-caps sections. In the end-cap region, detectors are located on disks perpendicular to the beam axis while in the barrel region, the detectors surround the beam axis in concentric cylinders so that Pixel and SCT cover the $|\eta| \leq 2.5$ region.

A particle leaving the IP will first interact with the Pixel detector. The sensors are

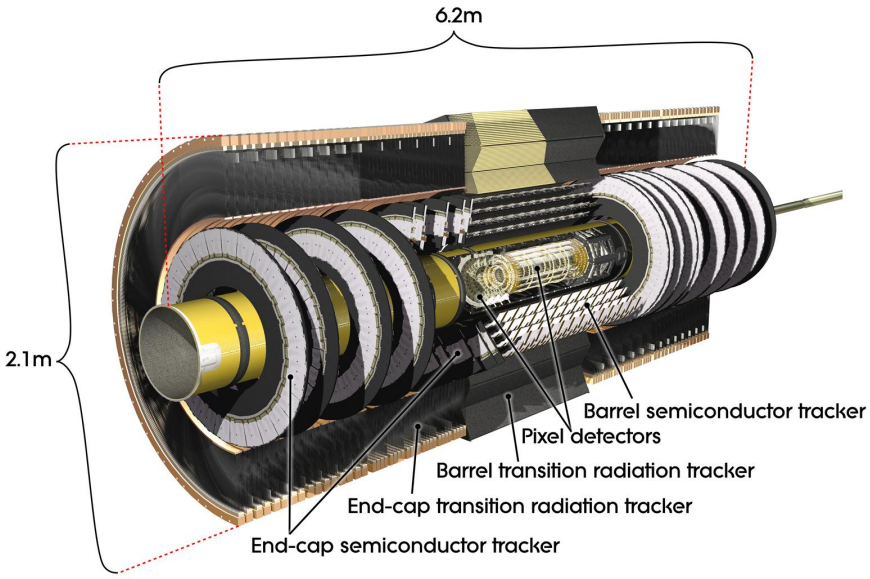

Figure 2.6: Cut-away view of the ATLAS Inner Detector [53].

segmented in $R-\phi$ and z with four pixel layers usually crossed by each particle. In the first layer the segmentation is of 50 μm$(R-\phi) \times 250$ μm(z) while for the other layers is 50 μm$(R-\phi) \times 400$ μm(z). The Pixel detector is equipped with more than 80 millions readout channels to provide a precise measurement for this segmentation level.

The Insertable B-Layer (IBL) [54] is the innermost pixel layer in the barrel and was installed between Run 1 and Run 2. It has a radius of only 33 mm. The original Pixel detector design was thought for a peak luminosity of 10^{34} cm^{-2}s^{-1} and this luminosity was exceeded during Run 2. This additional inner layer provides a better tracking, vertex reconstruction and b-tagging performance, as can be seen in Figure 2.7 that shows the resolution comparison on the transverse impact parameter (distance d_0 in the $x-y$ plane between the closest track to the z-axis and the z-axis) and the longitudinal impact parameter (the distance in the z-axis of the closest point to the z-axis) as a function of the transverse momentum p_{T}.

Normally, in the SCT detector [56] each track crosses eight strips layers. SCT uses a small angle (40 mrad) stereo strips in the barrel region with one set of strips parallel to the beam direction in order to measure both coordinates $R-\phi$. Stereo strips consist of two 6.4 cm long daisy-chained sensors with a strip pitch of 80 μm. Meanwhile, in the

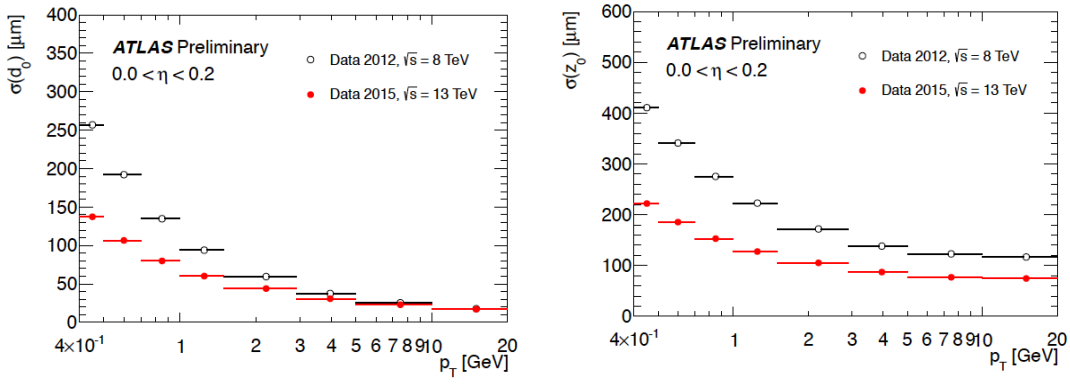

(a) (b)

Figure 2.7: a) Transverse impact parameter and b) longitudinal impact parameter resolution measured with data taken in 2015 at $\sqrt{s} = 13$ TeV, with the Inner Detector including the IBL, as a function of p_{T}, for values of $|\eta| < 0.2$, compared to those measured with 2012 data at $\sqrt{s} = 8$ TeV [55].

end-cap region the set of strips are running radially with another set at an angle of 40 mrad with a mean strip pitch of 80 μm. The total number of readout channels in the SCT is 6.3 million.

TRT contains a 4 mm diameter Xe-based gas mixture straw tubes covering $|\eta| < 2.0$. TRT only provides $R-\phi$ coverage with an accuracy of 130 μm per straw. In the barrel region the straws are parallel to the beam axis and are 144 cm long, the gold-plated wires are divided in two halves at $\eta = 0$. For the end-cap region the 37 cm straws are arranged radially in the wheels. The total number of readout channels of TRT is 351,000. For Run 2 there have been several upgrades to TRT in order to improve the response for the luminosity and to mitigate Xe-based gas mixture leaks.

The overall ID momentum resolution achieved during Run 1 was approximately [57]:

$$\frac{\sigma_{p_{\mathrm{T}}}}{p_{\mathrm{T}}} = 0.05\% \cdot p_{\mathrm{T}} \oplus 1\% \tag{2.5}$$

2.3.2 Calorimeters

The ATLAS calorimeter system is composed of electromagnetic and hadronic detectors with a full ϕ coverage. It is cylindrically placed around the ID and the solenoid magnet as shown in Figure 2.8.

The Liquid Argon (LAr) calorimeter is the innermost part of the calorimeter system and is composed by an electromagnetic barrel calorimeter covering $|\eta| < 1.5$, an electromagnetic end-cap calorimeter (EMEC) covering $1.4 < |\eta| < 3.2$, a hadronic end-cap calorimeter (HEC) covering $1.375 < |\eta| < 3.2$ and a forward calorimeter (FCal) covering $3.1 < |\eta| < 4.9$.

The Tile Calorimeter is the hadronic calorimeter in the outermost layer of the calorimeter system and is formed by a central long barrel (LB) covering $|\eta| < 1$ and two extended barrels (EB) in each side covering the region $0.8 < |\eta| < 1.7$.

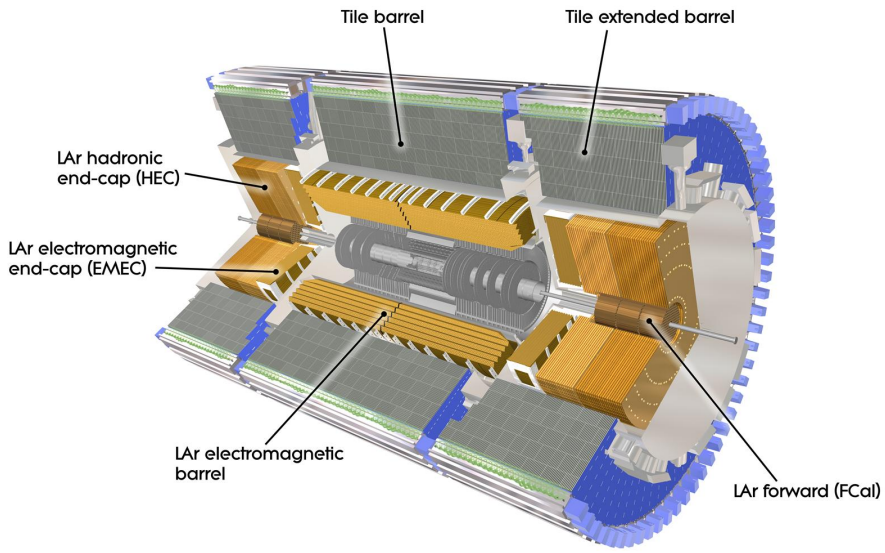

Figure 2.8: Cut-away view of the ATLAS calorimeter system [53].

Longitudinal length and lateral width characterize calorimeter showers that vary according to the type of the incident particle and the nature of the absorber of the calorimeter. Electrons and photons crossing the absorber material initiate an electromagnetic shower: photons convert in e^+e^- pairs and electrons emit bremsstrahlung photon radiation. The resulting electrons and photons then also interact with the absorber contributing to the development of the shower. The longitudinal depth of the ATLAS electromagnetic calorimeter is more than 20 radiation lengths. The Molière radius, which defines the lateral width of the shower in which 90% of the shower is

contained, is in average:

$$R_{\mathrm{M}} = \frac{X_0 E_{\mathrm{S}}}{\epsilon} = \frac{21_{\mathrm{MeV}} X_0}{\epsilon} = \frac{7A}{Z}\mathrm{gcm}^{-2} \tag{2.6}$$

where X_0 is the radiation length, E_{S} is the scattering energy, ϵ is the critical energy, A is the mass number and Z is the atomic number of the medium where the shower is developed.

On the other hand hadrons interact via the strong interaction. The shower is developed in a cascade of decay products, being on average 30% π^0 that decay electromagnetically so that the hadronic shower has a significant electromagnetic component.

The Liquid Argon Electromagnetic Calorimeter

The LAr electromagnetic calorimeter, as its name indicates, uses liquid argon as active material and lead plates as absorber. Liquid argon is characterized by his linear behavior, stability response over time and radiation-hardness. The absorber geometry follows an accordion-shape that provides a full ϕ coverage without azimuthal cracks.

The LAr calorimeter is divided in three regions, the barrel region (EMB, $|\eta| \leq 1.475$) and two end-caps regions (EMEC, $1.375 \leq |\eta| \leq 3.2$), each of these regions are housed with their own cryostat at 90 K. The EMB region is divided in two half-barrels separated by a gap of 4 mm at $z = 0$. For the EMEC regions they are each divided in two coaxial wheels, the outer wheel covers the region $1.375 \leq |\eta| \leq 2.5$ while the inner wheel covers $2.5 \leq |\eta| \leq 3.2$. The thickness of the EM calorimeter in the barrel region is $> 22\ X_0$ while in the end-cap regions is > 24 times the radiation length. In region $|\eta| \leq 1.8$ a presampler detector is used to correct the energy lost by electrons and photons upstream of the calorimeter. The presampler is an active liquid argon layer of 1.1 cm (0.5 cm) in the barrel (end-cap) region.

The geometry of the LAr EM calorimeter in the barrel region can be seen in Figure 2.9, where laterally and longitudinally segmentation into cells (individual readouts) can be observed. The EM calorimeter is further divided in three layers in the region devoted to precision physics ($|\eta| < 2.5$). The first layer is the most finely segmented in η which provides the highest precision in position measurement. The second layer

uses a 0.025×0.025 ($\Delta\eta \times \Delta\phi$) segmentation and collects the largest fraction of the EM shower energy. The third layer is designed for the tail of the EM shower using a bigger η segmentation. For the end-cap inner wheel, the calorimeter is segmented in two sections in depth with a coarser lateral granularity. The transition region between the barrel and the end-caps, located at $1.37 \leq |\eta| \leq 1.52$, is dedicated to detector services and therefore is no fully instrumented. The LAr EM calorimeter is designed with an energy resolution of $\sigma/E \approx 10\%/\sqrt{E(\text{GeV})} \oplus 0.7\%$.

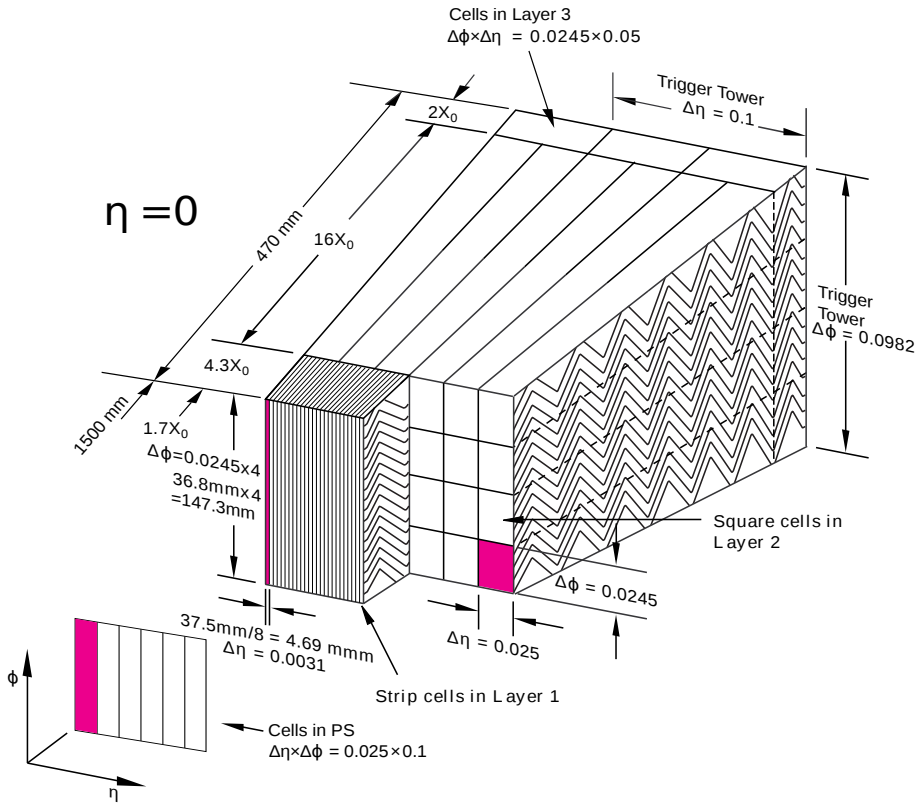

Figure 2.9: Schematic diagram of the cross section of the EM barrel calorimeter, including the presampler (labelled "PS") [58].

Tile Calorimeter

The Tile Calorimeter (TileCal) is the central section of the hadronic calorimeter of ATLAS. TileCal is designed to cover the $|\eta| \leq 1.7$ region of the detector. The inner radius of TileCal is 2.28 m while the outer radius is 4.25 m which results in a thickness of 9.7 interaction lengths (λ) at $\eta = 0$ for hadronic showers produced by LHC collisions.

TileCal is divided in one barrel region and two extended barrel regions surrounding the LAr calorimeter. The Long Barrel (LB) and Extended Barrels (EB) are divided in $|\eta| \leq 1.0$ (LB) and $0.8 \geq |\eta| \geq 1.7$ (EB). The gap crack regions between the TileCal LB and EB and the LAr EMB and hadronic end-caps sections are covered by scintillators (E-cells).

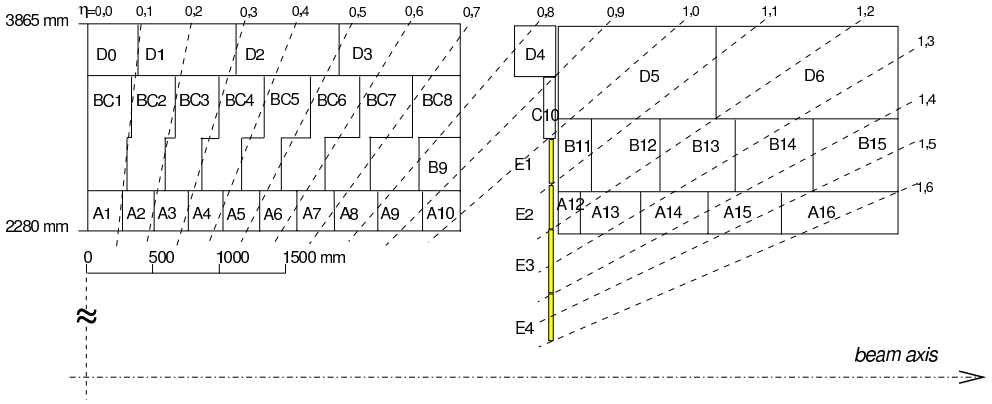

Figure 2.10: The layout of the TileCal cells, denoted by a letter (A to E) plus a number (integer). The A-layer is closest to the beam-line. The E-cells appear in yellow. The naming convention is repeated on each side of $\eta = 0$ [53].

TileCal uses iron plates as absorbers and scintillating tiles as active material. TileCal is designed to provide an energy resolution for jets of $\sigma/E \approx 50\%/\sqrt{E(\text{GeV})} \oplus 3\%$. The TileCal readout system is divided into 5000 longitudinal and transversal cells, each of them being read by two photomultipliers (PMTs). TileCal is divided in 4 partitions, LB A-side (LBA), LB C-side (LBC) and EB A-side (EBA), EB C-side (EBC). Each partition is divided in 64 modules of $\Delta\phi \approx 0.1$ with 45 channels in the long barrel modules and 32 channels in the extended barrel modules. All TileCal barrels are further divided in three layers: being the A-layer the closest to the beam axis, followed by the B(C) and D-layers. Figure 2.10 shows the radial and η structures of Tile. The Intermediate Tile Calorimeter (ITC) cells (D4, C10 and E-cells) are in between LB and EB providing a coverage in the region $0.8 \leq |\eta| \leq 1.6$. The gap-cells and crack-cells (E-cells) cover the range $1.0 \leq |\eta| \leq 1.6$ and are closer to the beam than the A-layer cells and therefore are more exposed to radiation. These scintillators are read out by only one PMT.

The Tile Calorimeter read-out is divided in three components: the optical part,

scintillators and fibers, and the PMT read-out electronics. The schematic of these components can be seen in Figure 2.11. When a particle interacts with the scintillators, it produces light that is collected and routed by wavelength shifting (WLS) fibers and converted into electronic pulses by the PMTs. The Analog to Digital Converters (ADCs) are in charge of the sampling and digitization of the pulses. The signal from the PMTs are then shaped and amplified with two gains. During normal operation only one of the two gains and only seven consecutive time samples of 25 ns are read-out in order to reduce the total data bandwidth. Trigger signals are formed by an analogue sum of input signals and sent to the calorimeter trigger system, which also considers input from the rest of the calorimeter system. For a given collision, if an event is selected by the trigger system, the digitizer signals are collected and processed by a Read-Out Driver (ROD) of the TileCal back-end electronics. In the unlikely case that all the memory buffers are full, the ROD generates a busy signal that is transmitted to the Trigger and Busy Module (TBM) and distributed to the Central Trigger Processor (CTP) to stop accepting new events until the busy signal is lifted. Also, integrators measure the integrated current from the PMTs which is used for calibration with a cesium source and to measure the rate of soft interactions during LHC collisions.

2.3.3 Muon Spectrometer

Figure 2.12 shows the outermost part of the ATLAS detector, the ATLAS Muon Spectrometer (MS). It is built from Monitored Drift Tubes (MDTs) for precision tracking in the spectrometer bending plane, Resistive Plate Chambers (RPCs) and Thin Gap Chambers (TGCs) for triggering in the barrel and end-cap, and Cathode Strip Chambers (CSCs) for precision measurements in the high-rate end-cap inner layer.

The magnetic field for muon momentum measurements is provided by the ATLAS toroid magnets, being orthogonal to the muon trajectories. In the $|\eta| \leq 1.4$ region the large barrel toroid magnetic field bends the muon trajectories while for the region $1.6 \leq |\eta| \leq 2.7$ the end-cap toroids are responsible for the bending of the muon trajectory. In the transition region $1.4 \leq |\eta| \leq 1.6$ the magnetic deflection is provided by a combination of the barrel and end-cap toroid fields. In order to achieve track reconstructions, 1850 Halls sensors mounted on spectrometer chambers map in detail

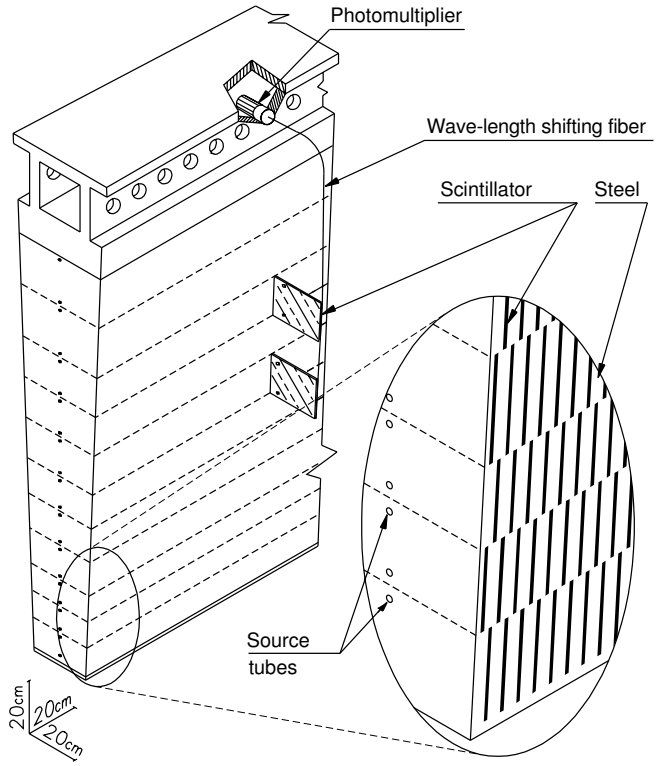

Figure 2.11: A schematic of a Tile Calorimeter wedge-shaped module showing the plastic scintillators sandwiched between steel absorbers. The front-end electronics drawer is located in the outer radius to read out the photomultiplier tubes [53]

.

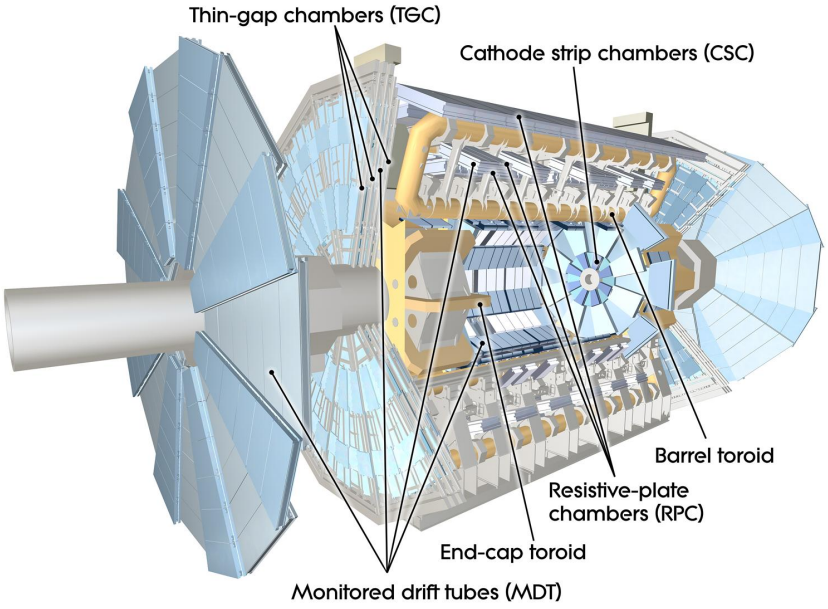

Figure 2.12: Cut-away view of the ATLAS muon system [53].

the magnetic field.

Another very critical measurement for momentum determination is the alignment of the spectrometer which is accomplished with an optical alignment system composed by 12,000 sensors. These sensors allow a three-dimensional reconstruction of the chamber positions to an accuracy up to 50 μm.

Typically muons cross three layers of MDT chambers. The track components in the bending plane of the spectrometer are measured by precision chambers with resolutions between 60-70 μm. Typically the track left by a 1 TeV muon is of 500 μm. The trigger chambers are in the opposite side of the middle MDT layer and provides a trigger based on the muon momentum.

2.3.4 Forward Detectors

The Forward Detectors are composed by three small detector systems. The first two systems are designed to measure the luminosity delivered to ATLAS. LUCID (LUminosity measurement using Cerenkov Integrating Detector) is placed at $\pm$17 m from the interaction point. LUCID is designed to detect inelastic pp scattering in the forward direction and monitors the relative luminosity for ATLAS. The second detector is ALFA

(Absolute Luminosity For ATLAS), placed at ±240 m. It is built from scintillating fibre trackers inside Roman pots and designed to be as close as 1 mm to the beam. The third system is the ZDC (Zero-Degree Calorimeter) which is designed to determine the centrality of heavy ion collisions at ±140 m from the interaction point. It is built alternating quartz rods and tungsten plates that measures neutral particles at $|\eta| = 8.3$.

2.3.5 Magnet system

ATLAS magnet system is formed by hybrid system of a central superconducting solenoid and three outer superconducting toroids. The magnetic system schematic can be seen in Figure 2.13, the magnetic system is 22 m in diameter and 26 m in length with a total stored energy of 1.6 GJ and a magnetic field covering a volume of 12,000 m^3.

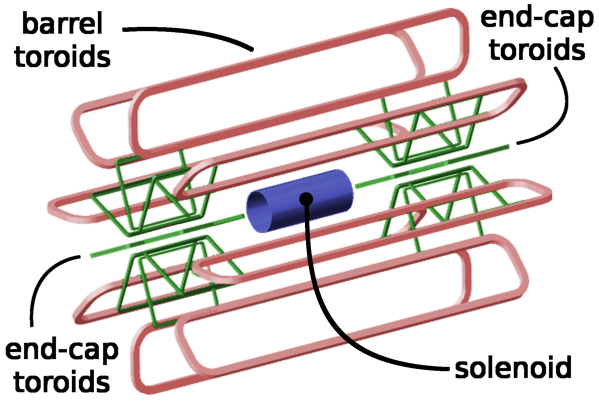

Figure 2.13: Schematic diagram of the ATLAS magnet system.

The solenoid provides the Inner Detector with a magnetic field of 2 T. This high magnetic field strength is obtained by keeping the solenoid thin in order to reduce the amount of material in front of the electromagnetic calorimeter. The solenoid is aligned with the beam, is 5.8 m long and has a diameter of 2.56 m.

The toroid system is divided between one barrel and two end-caps. The end-cap toroids are built from 8 coils each and produce a magnetic field of 1 T for the muon detector in the end-cap regions. The barrel region is built of 8 coils as well and produces a toroidal magnetic field of 0.5 T for the central muon detector.

2.3.6 Trigger, Data Acquisition and Detector Control Systems

The Trigger and Data Acquisition (TDAQ) system [59], timing and trigger control logic and the Detector Control System (DCS) are the collective pieces needed for ATLAS to retrieve information from collisions and are usually associated with sub-detectors although with the same logical components. The trigger system is divided in two levels, the second level refines the decision made by the previous level and adds additional selection criteria. The data acquisition system receives the event data from a detector specific read-out. Figure 2.14 shows the ATLAS TDAQ system schema.

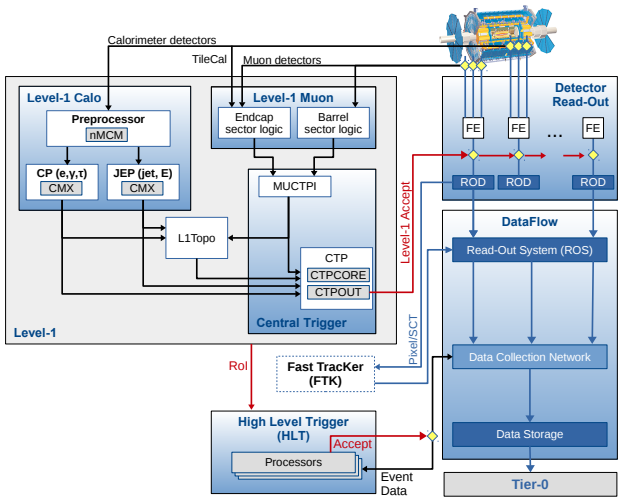

Figure 2.14: Schematic diagram of the Run 2 ATLAS Trigger and Data Acquisition system [60].

Trigger system

Collisions take place in intervals multiples of 25 ns. Given the design instantaneous luminosity of 10^{34} cm^{-2}s^{-1} and a bunch spacing of 25 ns, it results in an average number of 35 interactions per bunch-crossing or 1.4×10^{9} interactions per second. Given the current computation limits selective triggering is required. It is also needed to associate a unique bunch-crossing with each event to avoid background from other bunch-crossings.

The ATLAS Trigger system is divided in two levels. The Level 1 (L1) is the first level of trigger based on hardware logic working at a frequency of 40 MHz. It uses a sum of calorimeter signals provided by the detector and signals from muon trigger chambers. Therefore event selection can only happen if there are energy depositions in the calorimeters or muon track segments. It is located in the USA15 underground area, as close to the detector as possible to minimize the cable length and therefore reduce the transmission time.

The L1 trigger has been operating at different acceptance rate during the data taking period. During Run 1 it operated at a maximum speed of 60-65 kHz. During the long shutdown, in the years 2013 and 2014, the read-out electronics were improved and during the Run 2 it was capable of operating with a 100 kHz acceptance rate. The L1 trigger can handle an input rate of 40 MHz with a latency of 2.5 μs.

Data accepted by the L1 trigger is further analyzed by software running in the ATLAS trigger farm that provides the second level of triggering. The High Level Trigger (HLT) is designed with an average output rate of 1 kHz and a maximum processing time of 4 s. The HLT receives Region-of-Interest (RoI) [60] information from L1, which can be used for regional reconstruction in the trigger algorithms. After the events are accepted by the HLT, they are transferred to local storage at the experimental site and exported to the Tier-0 facility at CERN's computing centre for offline reconstruction.

Readout architecture and Data Acquisition

The high level of data concentration is achieved by the Read-Out Drivers (RODs) which are detector-specific elements of the back-end electronics and can retrieve data from several front-end data streams. When an event is selected by the L1 trigger the data is then transferred to the RODs. Raw data is then transferred to the DAQ system.

The DAQ is in charge of buffering, transporting and recording the events that are selected by the L1 trigger. First, the Read-Out System (ROS) stores temporarily the data in local buffers. The HLT receives part of the data, specifically the coordinates η and ϕ that have been selected, and, if the event passes the HLT criteria, the ROSes send the full event data and the rest of triggers are run in the same node. The events that have been selected by the HLT system are then permanently stored at the CERN

computer centre. In addition to the data, the configuration, control and monitoring of the hardware and software components that take part in the data-taking process are also stored.

Detector Control Systems

The Detector Control System (DCS) provides an easy and comprehensive environment for the operation of the ATLAS detector as well as a common user interface for all the sub-systems and technical infrastructure of the experiment. It is continuously monitoring the operational parameters, it automatically signals any abnormal behavior to the operator and even automatically corrects it or indicates manual actions that need to be taken. The DCS system also allows the communication with the DAQ system to synchronize the detector status with data-taking and handles the communication between the sub-systems that are controlled independently.

Computing and data management

The computing and data management plays an essential role in CERN experiments, so essential that it led to the invention of the World Wide Web (WWW) by Tim Berners-Lee in 1989 [61]. The current storage and management of the huge amount of data generated by CERN is done by the Worldwide LHC Computing Grid (WLCG), usually named GRID. The GRID is a network of computing centers around the world, which provides the necessary amount of storage as well as distributed computing resources for the analysis of the data.

The GRID is divided into Tiers, the Tier-0 is located in the CERN data centre and it is the core of the network. All the data generated in the LHC passes through this central hub although the Tier-0 is only about 20% of the total GRID computing capacity. It distributes the raw data and the reconstructed output to the Tier-1 centers, and reprocesses the data while LHC is not running. The Tier-1 is composed by 13 computing centers that stores a copy of the LHC data. It provides support to the GRID and stores a share of the raw and reconstructed data. It is also responsible for performing large scale reprocessing and storing the output. Tier-1 also distributes the data to Tier-2 and stores a part of the simulated data produced at Tier-2. Tier-2 are

computing centers located at universities and scientific institutes that can store data and provide computer power for simulation and analyses.

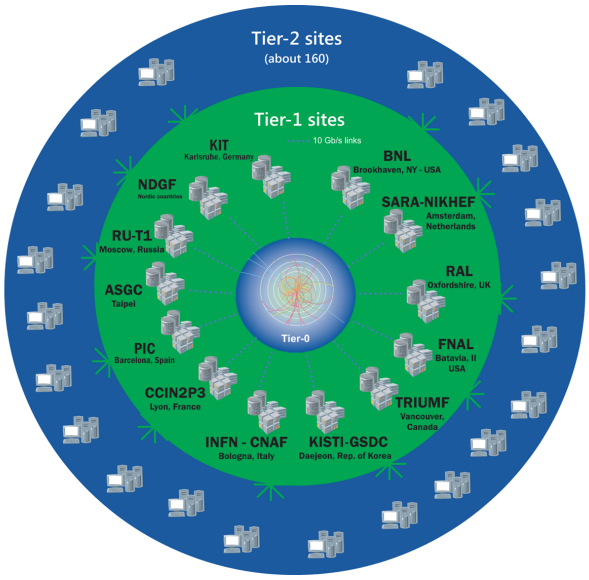

Figure 2.15: Diagram of the Tier hierarchy of the GRID, showing the Tier-0 (CERN Computing Center) in the inner layer, the 13 Tier-1 sites in the green layer and the Tier-2 sites in the blue outer layer [62].

From the raw data the Event Summary Data (ESD) format is derived. It contains all the reconstructed data and therefore is a very large data format. This data format is not usually stored.

The next format in data reconstruction is called Analysis Object Data (AOD). This is the format intended for primary use within ATLAS since it still contains all the information needed to perform physics analyses.

Users working with AODs also apply additional analysis selection to reduce the size producing the so called Derived Analysis Object Data (DAOD). During Run 1 the most common data format used a third level of selection criteria, the Derived Physics Data (D3PD). In this format instead of storing data in objects, every variable is stored in simplest types, integers, vectors of integers, etc. During Run 2 this format was replaced by a format named Mini-AODs (MAODs), created at a per-analysis or per-working group level, applying the convenient selection cuts, triggers, etc., to reduce further the size of the files. Even after all these levels of reduction, a typical analysis still employs several TBs of MAODs files.

Chapter 3

Objects and event reconstruction

ATLAS is designed to identify electrons, photons, muons, taus and jets from raw detector data using a dedicated set of algorithms, referred to as event reconstruction. Therefore the description of a collision, an event, requires the definition of different objects. The building blocks of these objects are the particle tracks reconstructed from hits (points assigned to a track) in the inner detector and the muon spectrometer in the case of muons and topological clusters constructed from energy deposits in the calorimeters. The hits are used to measure charged particles momentum and direction. Electrons and photons are reconstructed with a clustering algorithm that determines local energy deposits in the EM calorimeter.

In this chapter the reconstruction algorithms and techniques used to identify these objects are briefly described.

3.1 Tracks and primary vertices

3.1.1 Track reconstruction

Charged particles originated in pp collisions follow helicoidal trajectories in the presence of an axial magnetic field that can be parametrized by five quantities:

- ϕ_0, the azimuthal angle of the track.
- θ, the polar angle of the track.

- d_0, the transverse impact parameter, i.e. the distance from the point of closest approach to the reference point in the transverse plane.
- z_0, the longitudinal impact parameter, i.e. the z coordinate of the track at the point of closest approach mentioned in the previous bullet point. Strictly speaking, the longitudinal impact parameter is $|z_0| \sin\theta$.
- the ratio q/p, which defines the orientation and the curvature of the helix trajectory, where q denotes the electric charge and p the momentum.

The ATLAS track reconstruction software system [63] is a set of local and global recognition algorithms designed to identify charged particle trajectories in the inner detector. Its aim is to reconstruct tracks originated from the pp hard scatter (primary tracks), from decays of long-lived particles (secondary tracks) and from the interaction of particles with the detector itself (conversion tracks).

Primary tracks are required to have $p_{\mathrm{T}} > 400$ MeV and are reconstructed in the region $|\eta| < 2.5$ using the "inside-out" tracking sequence, which is a set of components:

- Data preparation and space point formation: the first step of the inner detector reconstruction algorithm consists of creating clusters and drift circles that are transformed into 3D space points in the silicon detector.
- Space point seeded track finding: seeds are defined as space points triplets and are the first step to find a track. Seeds are built from space points in the pixel detector, the strip detector or any combination setup. Seeds that pass the initial cuts are then the input of a track finding algorithm using the Kalman filter technique [64] aiming to complete the track candidates in the silicon detector.
- Ambiguity solving: this module is focused on the elimination of track candidates from random hit combinations (referred to as fakes) or track duplicates that are identified by shared properties with other track candidates. The ambiguity module is based on a scoring function applying positive scores for unique measurements and good fit quality and negative or low scores to holes (missing measurements where they would be expected) or shared measurements with other track candidates.

- TRT extension: once a track passes all the previous steps and is within the coverage of the TRT detector, measurements are completed in the outermost tracking detector.

Back-tracking is the complementary "outside-in" sequence, where the track starts from a segment reconstructed in the TRT detector and then extended inwards by adding silicon hits. Back-tracking is designed to reconstruct secondary and conversion tracks. When a track is found in the TRT detector but there is no extension into the silicon detector is then flagged as TRT-standalone track.

A consequence of the increasing detector occupancy with pile-up is the degradation of the track reconstruction since the combinatorial "fake" tracks are increased, i.e. reconstructed tracks which cannot be matched to a primary vertex nor secondary particle. In order to minimize this impact and improve the quality of the reconstructed tracks tight requirements on the hits, holes (non-existing but expected points) and outliers (hits that reduce the quality of the track fit) of the silicon detector are applied. Analyses usually cut on the d_0 and z_0 impact parameters or their errors to ensure that the track originates from the primary hard-scattering vertex.

3.1.2 Primary vertex reconstruction

Charged particle tracks that pass the previous requirements are combined to reconstruct the topology of the pp interaction. The spatial position of each particle is reconstructed using an iterative procedure divided in two stages: vertex finding and vertex fitting.

The first step is finding a vertex seed by looking for a global maximum in the distribution of z coordinates of the pre-selected tracks that are computed respect to the centre of the beamspot. Figure 3.1 shows the distribution of vertices for hadronic interaction candidates in the $x-y$ plane for data. The vertex position is then determined using the adaptive vertex fitting algorithm [65] constrained by the beamspot position. The fitting algorithm is a χ^2-based fitting algorithm that takes the input seed and the tracks around it. Each track that is used in the fitting process is weighted based on its compatibility with the fitted vertex. If a track is incompatible with the vertex by more than 7σ is then used to seed a new vertex. This procedure is repeated until no tracks

are left.

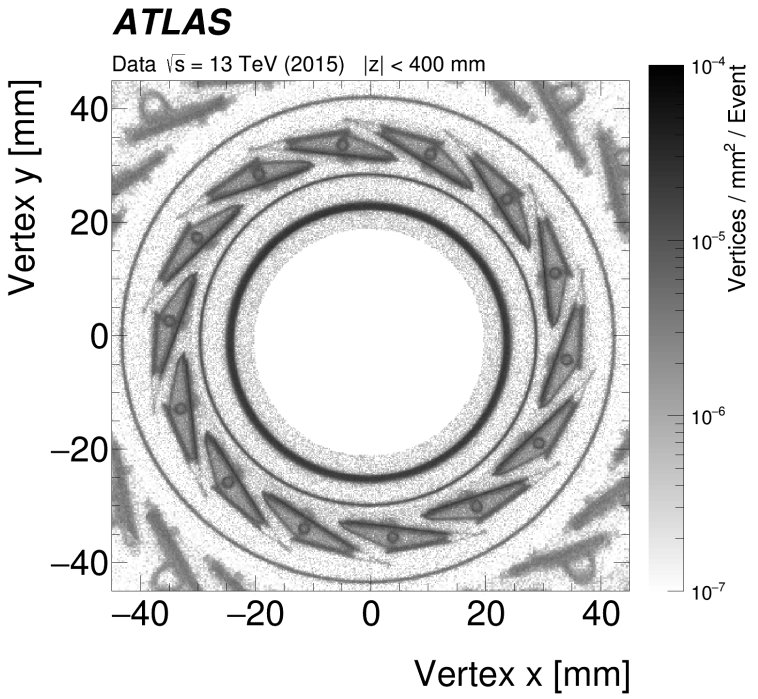

Figure 3.1: Distribution of hadronic-interaction vertex candidates in $|\eta| < 2.4$ and $|z| < 400$ mm for data. The plot shows the $x - y$ view zooming-in to the beam pipe, Inner Positioning Tube (IPT), IBL staves and Inner Support Tube (IST) [66].

The resolution of the vertex position is proportional to the number of associated tracks to it, N_{trk}, and to the quadratic sum of their transverse momentum $\sum_i^{N_{trk}} p_{\text{T},i}^2$. The primary vertex is the one with the highest sum of transverse momentum while the rest are flagged as pile-up vertices.

For the analysis presented in this thesis, the primary vertex of the event is selected among all the reconstructed vertices, using a neural network algorithm based on track and primary vertex information, as well as the directions of the two selected photons measured in the calorimeter and inner detector [67].

3.2 Photons

3.2.1 Photon reconstruction

The photon interaction with the EM calorimeter is the origin of the electromagnetic showers, which deposits a significant amount of energy in a small number of neighbouring calorimeter cells. The reconstruction of photons can be divided in several steps:

- Topoclusters: the topocluster reconstruction algorithm [68] forms protoclusters in the EM and hadronic calorimeters using a set of noise thresholds in which the cell initiating the cluster is required to have a significance 4 times higher than the expected cell noise. The expected cell noise is built from the known electronic noise and the estimated pile-up noise corresponding to the average instantaneous luminosity expected from Run 2.

- Seed cluster building: the first step to reconstruct photon candidates in the region $|\eta| < 2.5$ starts by building seed clusters from energy deposits in the EM calorimeter. Cells in the EM calorimeter from all three layers are grouped into $\Delta\eta \times \Delta\phi$ towers of 0.025×0.025 by a sliding-window algorithm [69] with windows of size 3×5 in $\eta - \phi$ space and transverse momentum above 2.5 GeV, followed by duplicate removal. Based on Monte Carlo simulations, the cluster building efficiency is estimated to be greater than 99% for photons with $E_{\mathrm{T}} > 20$ GeV.

- Track reconstruction: once the seed clusters are reconstructed, the next step is to search for inner detector tracks that can be loosely matched to the clusters in order to identify and reconstruct photon conversions. The initial clusters are used to create RoIs. Standard track pattern reconstruction [63] is performed within the defined RoIs. If the pattern recognition fails for a silicon track seed that is within a RoI, a modified pattern reconstruction algorithm is then performed based on a Kalman filter allowing a 30% energy loss at each material intersection. The track candidates are then fitted using an ATLAS global χ^2 fitter [70] that allows additional energy loss for cases that the standard track fit fails.

- Track conversion: tracks consistent with originating from a photon conversion are

used to create conversion vertex candidates.

- Track-cluster matching: conversion vertex candidates are matched to seed clusters.

- Final cluster creation: a final algorithm decides whether a seed cluster corresponds to an unconverted photon, a converted photon or a single electron based on the matching to conversion vertices or tracks and on the cluster and track(s) four-momenta.

Photon conversion

The conversion-finding algorithm is run on the loosely-matched tracks using tracks with silicon hits and tracks reconstructed only in the TRT. The converted photons are classified into single-track or double-track. Double-track conversion vertex candidates are reconstructed from pairs of oppositely charged tracks in the inner detector that could be electrons. On the other hand, single-track conversion vertex candidates are tracks that are missing hits in the innermost sensitive layers. In order to increase the converted photon purity, the tracks that are used to build conversions have a high probability to be electron tracks determined by the TRT.

The matching of tracks from the conversion vertices and clusters relies on an extrapolation of the conversion candidates to the second layer of the calorimeter and the comparison of the extrapolated η and ϕ coordinates to the ones of the cluster centre (ΔR). For better pile-up tolerance quality cuts are applied on the conversion vertices. The dead pixel map is also used in order to determine the conversion quality since dead pixels can affect the conversion building.

If there are multiple conversion vertices matched to a cluster, double-track conversion with two silicon tracks is selected over double-track conversion, followed by single-track conversion. Also, the vertex with the smallest conversion radius is preferred. The conversion vertex matching procedure is performed twice, first is used to determine the potential seed clusters and secondly to complete photon superclusters. The fraction of converted / unconverted photons can be seen in Figure 3.2.

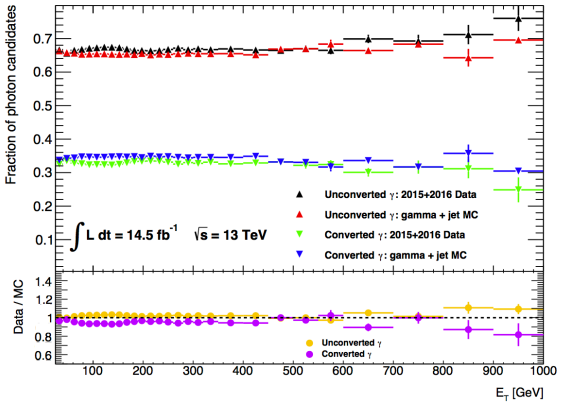

(a)

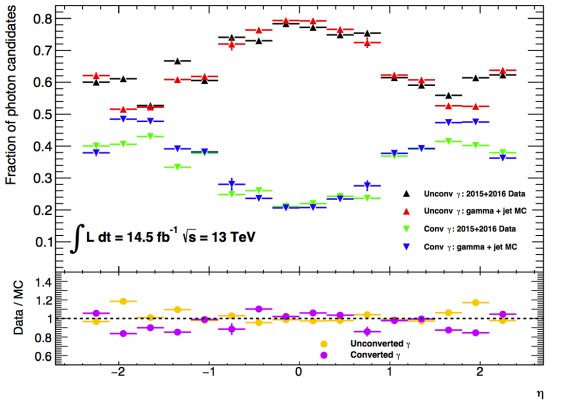

(b)

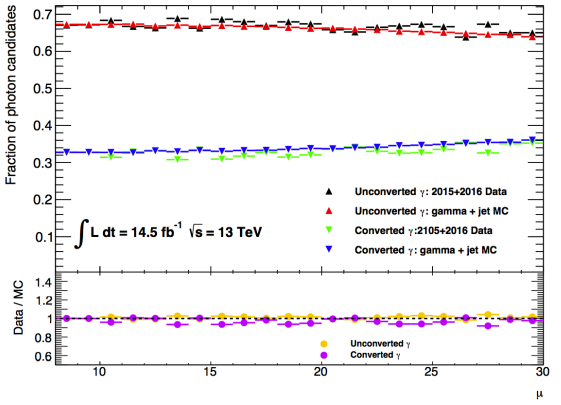

(c)

Figure 3.2: Fraction of converted and unconverted photons as a function of a) transverse energy E_{T}, b) detector pseudorapidity η and c) number of interactions per crossing μ, with early Run 2 data. Comparison with MC simulated γ+jet events is also shown.

3.2.2 Photon identification

Once a photon candidate is found it is also required to satisfy a set of identification criteria to reduce contamination from background, that is primary neutral pions in jets decaying into photon pairs. The photon identification is constructed from one-dimensional selection criteria, or a cut-based selection, based on the geometry of the electromagnetic shower in the calorimeter [71, 72], using variables such as R_{had}, R_{ϕ}, E_{ratio}, d_0 and E/p among others. Photons are required to deposit only a small fraction of their energy in the hadronic calorimeter and a lateral shower shape that has to be consistent with a single electromagnetic shower. There are two levels of selection:

- The loose identification which exploits discriminating variables, as the ratio of E_{T} in the hadronic calorimeter to the E_{T} of the EM cluster or the lateral width of the shower. It provides a highly efficient selection with fair background rejection and is typically used for the trigger and background studies.
- The tight identification on the other hand exploits the full granularity of the EM calorimeter and applies tighter requirement on the discriminating variables used by the loose identification. The efficiency of this identification level ranges from 67% (60%) to 90% (95%) for unconverted (converted) isolated photons from p_{T} of 15 GeV to 50 GeV.

Figure 3.3 shows different methods that are used to measure the efficiency of the photon identification level covering a broad energy spectrum:

- At the low energy spectrum, radiative photons from $Z \to \ell\ell\gamma$ decays are selected through kinematic requirements on the dilepton pair, the invariant mass of the three particles in the final state and on the quality of the two leptons.
- For the medium energy range, the $Z \to ee$ decay is used to exploit similarities between electron and photon showers and photon ID efficiencies are obtained using a tag-and-probe method.
- At high energy, inclusive photon final states are used applying the matrix method, which classifies the photons between prompt and background photon candidates,

passing or failing tight identification criteria.

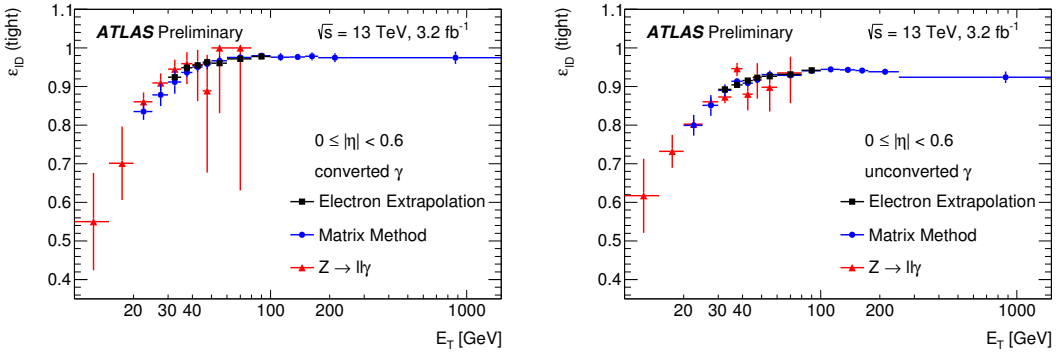

(a) (b)

Figure 3.3: Comparison of the data-driven measurements of the identification efficiency for a) converted photons and b) unconverted photons [73].

Figure 3.4 shows the differences between the simulation and the data-driven measurements that are taken into account by computing data-to-MC efficiency ratios, that are known as scale factors (SFs).

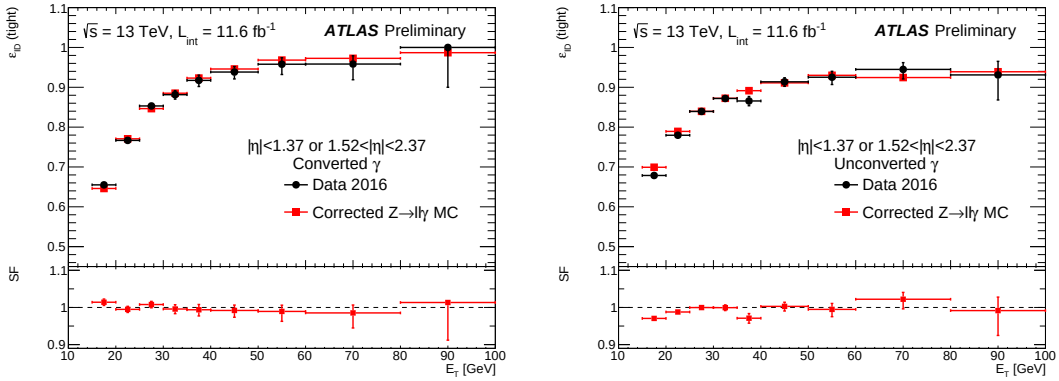

(a) (b)

Figure 3.4: Comparison of the radiative Z boson data-driven efficiency measurements of a) converted and b) unconverted photons to the $Z \to \ell\ell\gamma$ simulation as a function of the E_{T}, in the region $15 \leq E_{\mathrm{T}} \leq 100$ GeV. The lower panel shows the ratio between the data and the simulation [74].

3.2.3 Photon isolation

Photon candidates are required to be isolated from any other activity in the calorimeter and the tracking detector in order to reject the hadronic jet background. The

calorimeter isolation is defined as the sum of the transverse energies of positive-energy topological clusters [75] in a cone of $\Delta R = 0.2$ centered around the photon shower origin. The transverse energy of the photon candidate is removed and the contributions of the underlying event and pile-up are subtracted according to the method suggested in [76]. The isolated track is required to deposit less than 6.5% of the photon E_{T} in the calorimeter. The efficiency of the isolation requirement for photons satisfying the tight identification criteria ranges from 60% for $E_{\mathrm{T}} \geq 15$ GeV to more than 90% for $E_{\mathrm{T}} \geq 40$ GeV. The jet background rejection factor for isolation requirements with respect to the tight identification criteria is of approximately 1.5.

3.2.4 Photon calibration

Precise measurements of photon energy are of vital importance in analyses involving photons as the one presented in this thesis. There are different effects that impact the energy resolution and bias the measured value of the photon energy [77]:

- The energy loss due to the amount of material that sits in front of the EM calorimeter.
- The energy loss due to dead material inside the EM calorimeter.
- The energy loss laterally outside the reconstructed cluster.
- The energy loss longitudinally behind the EM calorimeter.

The sum of the energy in the cells will be less than the true energy if there is no calibration procedure [78]. The energy of the photons is calibrated using a multivariate regression algorithm in order to account for the energy losses. After the multivariate analysis, measurements using $Z \rightarrow ee$ events are performed to determine the energy scale and resolution in data and Monte Carlo. These measurements are then used to correct the energy scale in data and to smear the energy resolution in simulations.

MVA calibration

The energy calibration is derived with a multivariate technique using a single particle Monte Carlo sample. The regression MVA technique chosen is a boosted decision tree

with gradient boosting targeting the ratio between true photon energy and photon energy measured in the calorimeter.

The input variables for the MVA training are the total raw cluster transverse energy measured by the calorimeter (E_{acc}), the ratio of the pre-sampler layer transverse energy to the calorimeter transverse energy (E_0/E_{acc}), the ratio between the transverse energy measured in the first two layers of the calorimeter (E_1/E_2), the cluster barycenter η in the ATLAS coordinate system and the cluster barycenter η and ϕ in the EM calorimeter coordinate system.

The Monte Carlo sample is divided into different regions based on the pseudorapidity (η), measured transverse energy (E_{acc}) and whether the photon is converted or unconverted.

Corrections

After applying the MVA based calibration there could still be some disagreement between energy scale and resolution in data. To account for this possible disagreement a correction is evaluated using $Z \to ee$ events. The energy miscalibration is defined as the difference between data and MC simulation that can be parametrized as:

$$E_i^{\text{data}} = E_i^{\text{MC}}(1 + \alpha_i), \tag{3.1}$$

where E_i^{data} is the electron energy in data and E_i^{MC} is the photon energy in simulation. The deviation from the perfect calibration in a given η region, labeled with i, is represented by α_i. The difference in energy resolution between data and simulation can be modeled adding an additional term c_i' for a given η bin as:

$$\left(\frac{\sigma(E)}{E}\right)_i^{\text{data}} = \left(\frac{\sigma(E)}{E}\right)_i^{\text{MC}} \oplus c_i'. \tag{3.2}$$

The measured values of α_i range between -2% and +2% depending on the η bin. The measured values of c_i' range between 0.005 and 0.03 depending on η.

Even though Z bosons decay to electrons, the corrections are also valid for photons. This validity is tested using photons from radiative Z boson decays in the electron and muon channel and the results are found to be compatible.

3.3 Electrons

3.3.1 Electron reconstruction

Electron reconstruction in the central region of the ATLAS detector ($|\eta| < 2.47$) proceeds in several steps:

- Seed-cluster reconstruction: electrons are formed by matching tracks reconstructed in the Inner Detector with electromagnetic clusters found using the supercluster algorithm. The efficiency of the cluster reconstruction for a true e/γ ranges from 95% at $E_{\mathrm{T}} = 7$ GeV to more than 99% for E_{T} above 15 GeV.

- Track reconstruction: it can be divided in two steps: pattern recognition and track fit. Pattern recognition is based on the pion hypothesis for energy loss in the interactions with the detector material. It is complemented with a modified pattern recognition algorithm that accounts for the energy loss for possible bremsstrahlung. If a track seed with a $p_{\mathrm{T}} \geq 1$ GeV cannot be extended to a full track and it falls within one of the EM RoIs, a second attempt is performed using another pattern recognition based on the electron hypothesis which allows larger energy loss. Track candidates are then fitted using the ATLAS global χ^2 track fitter with either hypotheses.

- Electron specific track fit: tracks are loosely matched to EM clusters using the distance in η and ϕ between the track position extrapolated to the calorimeter middle layer and the cluster barycentre. Energy-loss due to bremsstrahlung and number of precision hits in the silicon detector are considered in the matching conditions. If a track has a significant number of precision hits (≥ 4) and is loosely associated to an electron cluster, it is refitted using an optimized Gaussian Sum Filter [79] taking into account non-linear bremsstrahlung effects.

- Electron candidate reconstruction: the reconstruction procedure is completed by the matching of the track candidate to the cluster seed. If the matching conditions are satisfied by several tracks, one track is chosen as a primary track. The choice is based on an algorithm using the cluster-track distance R calculated using different

momentum hypotheses, the number of pixel hits and the presence of a hit in the first silicon layer [80]. If an electron candidate does not have any associated precision hit track it is then removed and flagged as a photon. Then the electron cluster energy is calibrated to the original electron energy using MVA techniques based on MC samples. Also, data-driven scale corrections are derived from $Z \to ee$ events following the same procedure described for photons in Section 3.2.4.

The electrons' four-momentum is computed using both the final calibrated energy cluster and the best track matched to the original seed cluster information. The energy is given by the calibrated cluster while the η and ϕ are given by the track.

For Run 2 analyses, electron measurements require that the track that is associated to the electron must be compatible with the primary interaction vertex of the pp collision in order to reduce the background from conversion and secondary particles. To accomplish the compatibility with the primary vertex the distance Δz_0 between the track and the primary vertex is used.

3.3.2 Electron identification

Electron identification algorithms are used to determine if the reconstructed electron candidates are signal-like objects or background-like as jets or converted photons. The identification algorithm uses electron cluster and track measured quantities such as calorimeter shower shapes, information from the transition radiation tracker, track-cluster matching related quantities, track properties and measurements of the bremsstrahlung effects in order to distinguish signal from background.

An schematic view of the electron reconstruction and identification can be seen in Figure 3.5.

Different likelihood-based (LH) identification criteria are defined as loose, medium and tight operating points based on 95%, 90% and 80% electron identification efficiency for electrons with $E_{\mathrm{T}} \approx 40$ GeV, respectively. Electron identification efficiencies are found to be robust with respect to the number of primary vertices.

The $Z \to ee$ and $J/\psi \to ee$ decays are used to measure the electron identification efficiencies and isolation cuts using a tag-and-probe technique. Strict selection criteria

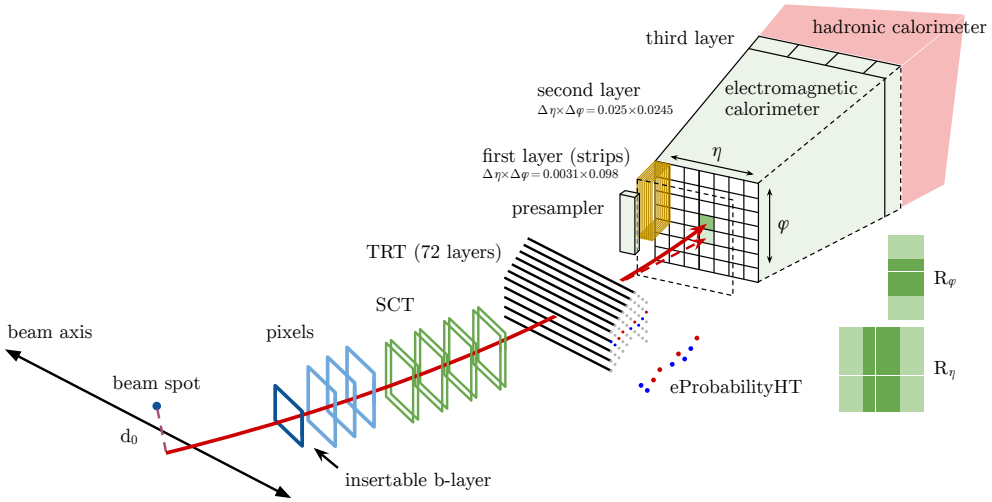

(a)

Figure 3.5: Schematic view of the electron reconstruction and identification [81].

are applied to one of the electron candidates (known as tag) together with the requirement of the di-electron invariant mass window centered in the mass of the leptonically decaying particle, this allows a loose pre-identification of the other electron candidate (known as probe).

The low E_{T} range, from 4.5 to 20 GeV, is studied by $J/\psi \to ee$ that suffers from a high background contamination while $Z \to ee$ events are used for energies above 15 GeV, as can be seen in Figure 3.6.

3.4 Muons

Muons produced in pp collisions are identified and reconstructed using information from the muon spectrometer, inner detector and EM calorimeter. Muon identification is performed according to several reconstruction criteria [83, 84], leading to different muon types:

- Stand-Alone (SA) muons: MS tracks found within the MS acceptance, but outside the ID acceptance ($2.5 < |\eta| < 2.7$) and momentum taken from the MS track.
- Combined (CB) muons: a MS track is matched to a reconstructed track in the ID, and the measurements of the momenta are combined. This is the type of

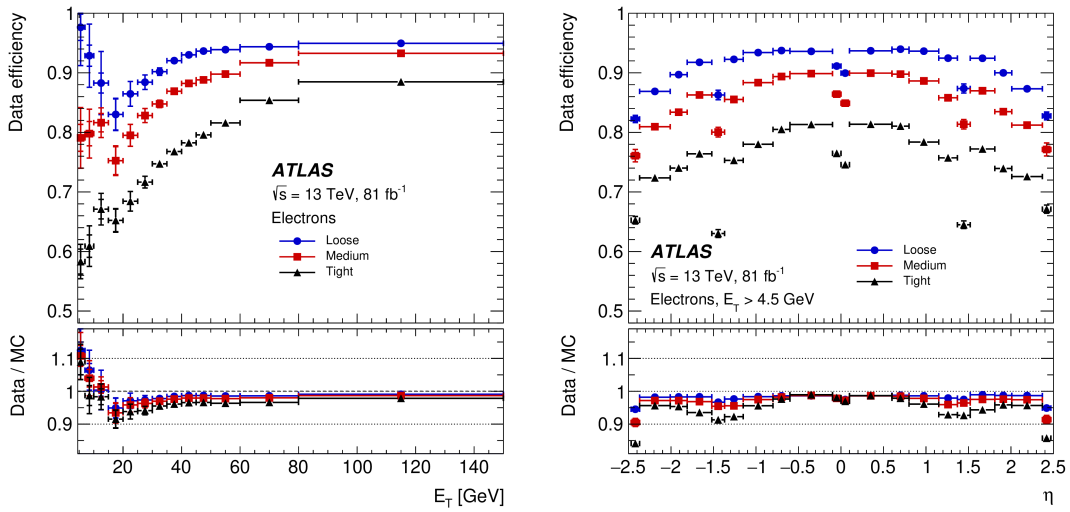

(a) (b)

Figure 3.6: Electron identification efficiency in $Z \to ee$ events in data as a function of E_{T} (left) and as a function of η (right) for the loose, medium and tight operating points. The efficiencies are obtained by applying data-to-simulation efficiency ratios measured in $J/\psi \to ee$ and $Z \to ee$ events to simulation. The inner uncertainties are statistical and the total uncertainties are the statistical and systematic uncertainties in the data-to-simulation efficiency ratio added in quadrature. For both plots, the bottom panel shows the data-to-simulation ratios [82].

reconstructed muons most commonly used by physics analyses.

- Segment-tagged (ST) muons: a partial MS track is matched to an ID track, and the muon momentum is taken from the ID measurement.

- Calorimeter-tagged (CaloTag) muons: in the non-active "crack" of the MS at $|\eta| < 0.1$, muon candidates are reconstructed from a track in the ID that has an EM calorimeter energy deposit compatible with a minimum ionizing particle.

Two reconstruction software packages are used for the reconstruction of muons used in physics analyses, each implementing different strategies named chains, which combine the information from the ID tracks and MS track segments. Staco or Chain 1 combines the ID and MS track candidates using the corresponding track parameters and covariance matrices. Chain 2 or Muid performs a global χ^2 fit of the muon tracks, using both ID and MS measurements.

Chain 3 is an improved algorithm that combines the best features of the other two chains and has been used to reconstruct Run 2 muons. Some additional improvements

are the better calculation of the energy loss in the calorimeter, the use of a Hough transformation [85] to increase track-finding efficiency and a higher background rejection.

Background, mainly from pion and kaon decays, is suppressed by applying quality requirements to muon identification while selecting muons with high efficiency and/or guaranteeing a robust momentum measurement. Simulated $t\bar{t}$ events are used to determine good discrimination variables between prompt muon and background muon candidates. Muons from W decays are categorized as signal muons while muon candidates from light hadron decays are categorized as background. Quality requirements are also imposed to reconstructed muons, including minimum requirements on the number of hits in each of the tracking subdetectors and the MS. Identification selections are divided in four (loose, medium, tight and high-p_{T}) categories addressing specific needs of different physics analyses. Loose, medium and tight are inclusive categories so that muons identified with tighter requirements are also included in the looser categories.

Using two independent detectors to reconstruct muons (the ID and the MS) enables a precise determination of the muon reconstruction efficiency in the region $|\eta| < 2.5$. This efficiency is obtained using the tag-and-probe method with $Z \to \mu\mu$ and $J/\psi \to \mu\mu$ decays covering a broad muon p_{T} spectrum. For this method, one of the muons (tag) is required to be identified as a medium muon that fires the trigger and the second muon (probe) is required to be reconstructed by a system independent of the one being studied. Scale factors take into account the differences in the measured reconstruction efficiency in data and MC that differ from unity within a few percent.

Muon reconstruction efficiency as a function of η measured from $Z \to \mu\mu$ events can be seen in Figure 3.7a. At low p_{T} the efficiency is measured using $J/\psi \to \mu\mu$ events as can be seen in Figure 3.7b as a function of p_{T} in different η regions. Loose and medium selection efficiencies are very similar throughout the detector except for $|\eta| < 0.1$, where the loose selection fills the MS acceptance gap using the calorimeter and segment-tagged muon contributions.

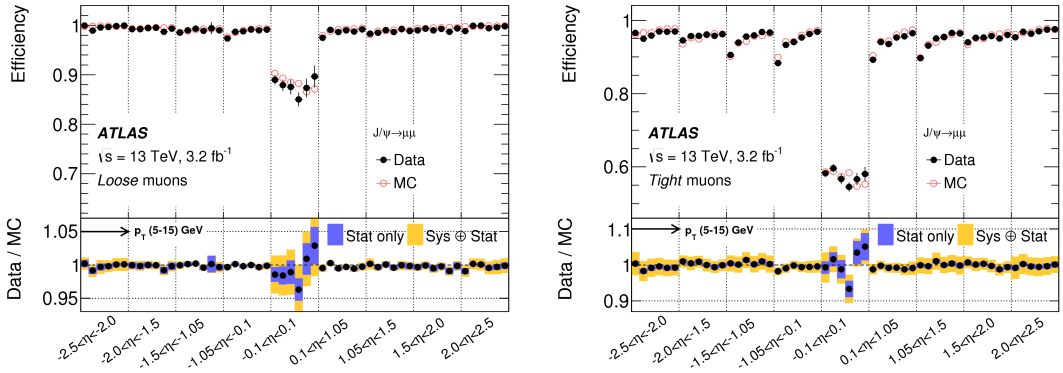

(a) (b)

Figure 3.7: Muon reconstruction efficiency in different η regions measured in $J/\psi \to \mu\mu$ events for loose (left) and tight (right) muon selections. Within each η region, the efficiency is measured in six p_{T} bins (5–6, 6–7, 7–8, 8–10, 10–12, and 12–15 GeV). The resulting values are plotted as distinct measurements in each η bin with p_{T} increasing from 5 to 15 GeV going from left to right. The error bars on the efficiencies indicate the statistical uncertainty. The panel at the bottom shows the ratio of the measured to predicted efficiencies, with statistical and systematic uncertainties [84].

3.5 Jets

A jet is a collimated spray of hadrons and is one of the most abundant phenomena in pp collisions at the LHC. The jet energy scale, along with the energy and angular resolution is achieved by a calibration procedure. Jet reconstruction and calibration is a very important procedure that facilitates the identification of known resonances decaying into hadronic jets as well as searches for new particles.

The anti-k_t algorithm [86] is the default jet reconstruction algorithm used by ATLAS with distance parameters of $R = 0.4$ and $R = 1.0$. The input objects for this algorithm are: calorimeter energy deposits, inner detector tracks [87] or a combination of both [88]. Track jets have low dependence on the pile-up activity since only tracks originating from the primary vertex are used for the jet. Track jet reconstruction is limited by the ATLAS tracker acceptance of $|\eta| < 2.5$. Therefore, ATLAS analyses requiring jets outside this region use a jet reconstruction based on calorimeter deposits that are called calorimeter jets.

For calorimeter jet reconstruction the inputs are the topologically clustered cells, called topoclusters [75]. The topological clustering algorithm groups cells where a significant energy has been deposited, aiming for effective noise suppression. The noise in

a calorimeter cell, σ_{Noise}, is calculated as the quadratic sum of the measured electronics noise and the average energy deposited by concurrent pp interactions, so called pile-up noise. The clustering algorithm starts from cells with energy deposits above $4\sigma_{\text{Noise}}$ as seeds. If a neighbour cell has an energy deposit above $2\sigma_{\text{Noise}}$ it is added to the topocluster. Finally, the cluster splitting algorithm separates produced topoclusters based on local energy maxima to avoid overlap. Only topoclusters with positive energies are used for jet reconstruction and all are considered to be massless.

Calorimeter cell energy is measured at the EM scale, which is established using electrons at test beams. The local cell weighting (LCW) calibration [89] can be applied to topoclusters classified as hadronic to account for the difference in the detector response to electromagnetic and hadronic particles. To calibrate LCW, single pion events from simulation samples are used.

The jet energy scale (JES) calibration [90] adjusts the energy scale of reconstructed jets to that of simulated truth jets. Using the EM and LCW topoclusters different sets of correction factors are developed. The JES calibration includes origin correction, pile-up correction, absolute correction for the detector response, global sequential correction and residual in-situ calibration:

- Origin correction: the four-momentum vector of the jet is forced to point to the hard-scatter primary vertex instead of the centre of the detector while the jet energy is kept.

- Pile-up contribution: the first step is to remove the effect of pile-up exploiting the average energy density and the area of the jet. Secondly, a residual correction is applied to remove the dependence of the jet on the number of reconstructed primary vertices (N_{PV}) and the expected average number of interactions per bunch crossing ($\langle\mu\rangle$). The performance of the pile-up correction is shown in Figure 3.8a.

- The jet energy scale and η calibration correct the reconstructed jet to the particle level energy scale in order to account for the difference of the calorimeter energy response using MC simulations. Any bias of the reconstructed jet η caused by transitions between different calorimeter regions are also corrected. Figure 3.8b shows the energy response as a function of η for jets at different truth energies.

- Global sequential correction (GSC) [91] is designed to remove the flavour of the initiated-jet parton dependence from the jet response. This correction uses jet global properties as the portion of the jet energy measured in the first layer of the hadronic calorimeter, the portion of the jet energy measured in the third layer of the EM calorimeter, the average p_{T}-weighted transverse distance in the $\eta-\phi$ phase space between the jet axis and all tracks related to the jet, the number of tracks associated to the jet and the number of muon track segments associated to the jet. This correction removes the jet response dependence on all listed observables.

- In-situ JES calibration is applied to jets measured in data. This correction is computed as the jet response difference between data and MC simulation using the transverse momentum balance of a jet and a reference object. There are different in-situ methods as: relative η-intercalibration, where the jet response in a particular region is corrected relative to the jet response in the central region; direct transverse momentum balance between a photon or a Z boson and a jet, allowing a correction of the jet response in the central region; balance between a high-p_{T} jet and a recoil system of high-p_{T} jets that have been calibrated by previous techniques. The relative jet response as a function of η in a single jet p_{T} bin is shown in Figure 3.9a. The combined in-situ corrections can be seen in Figure 3.9b measured using Z+jets, γ+jets and multijet events.

3.5.1 Jet energy scale uncertainty

The uncertainty on the JES is frequently the dominant systematic uncertainty in many physics analyses. The total uncertainty on the JES as a function of p_{T} and η of the jet is shown in Figure 3.10. The total uncertainty at low jet p_{T} reaches up to 5% driven by the in-situ method uncertainties. This uncertainty can be tweaked by varying the event selection criteria, calibration and modeling of the objects used as reference. Also additional JES uncertainties due to event topologies, as the selection of samples with different flavour compositions are accounted.

At high jet $p_{\mathrm{T}} > 200$ GeV the in-situ method uncertainties are of about 1% being the dominating ones. Pile-up correction uncertainties are evaluated in-situ using track

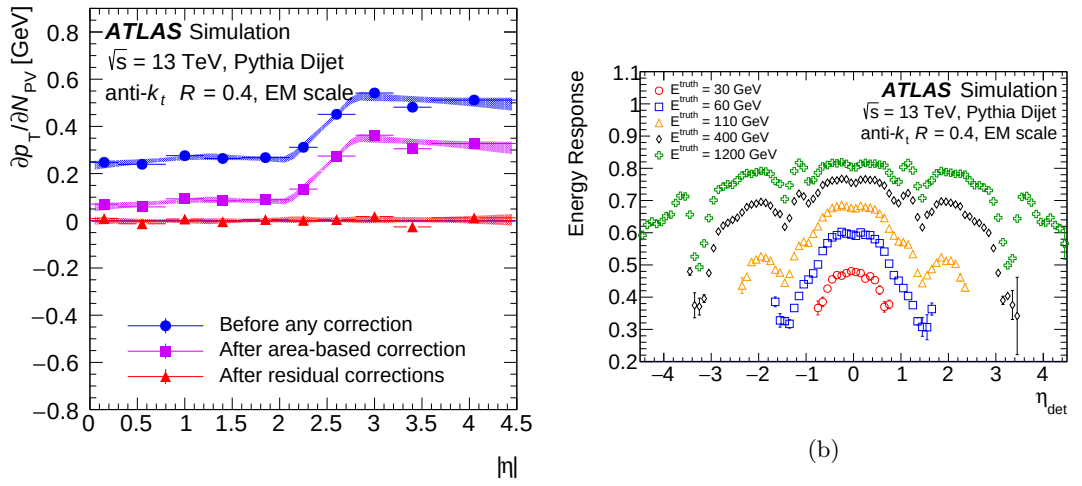

(a) (b)

Figure 3.8: a) Dependence of the jet p_{T} with the number of primary vertices, for simulated events, before pile-up corrections (blue), after the area-based correction (violet), and after the residual correction (red). b) The average jet energy response as a function of the detector pseudorapidity for different truth energies [92].

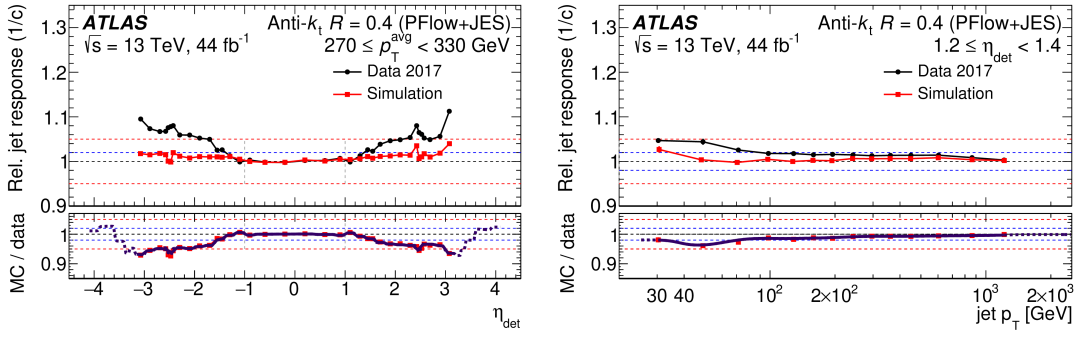

(a) (b)

Figure 3.9: Relative response of jets at the PFlow+JES scale in 2015+2016 data (black circles) and Powheg+Pythia8 MC simulation (red squares) for (a) jets of $270 < p_{\mathrm{T}}^{\mathrm{avg}} < 330$ GeV as a function ot η_{det}, (b) as a function of p_{T} for jets of $1.2 < \eta_{\mathrm{det}} < 1.4$. The lower panel shows the response ratio of MC simulation to data (red squares) as well as the smoothed in-situ calibration factor derived from the ratio (solid curve). Dotted lines show the extrapolation of the in-situ calibration to the regions without data points. The dashed red and blue horizontal lines provide reference points for the viewer [93].

jets and the p_{T} balance between the jet and a Z boson.

Jets in the $p_{\mathrm{T}} > 2$ TeV region are not covered by the Multijet Balance calibration and larger uncertainties are taken from single particle measurements. Each uncertainty is independent from the others and fully correlated across p_{T} and η.

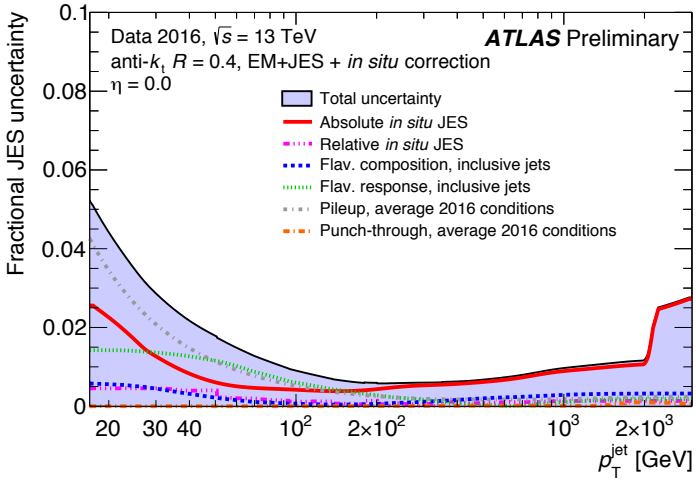

(a)

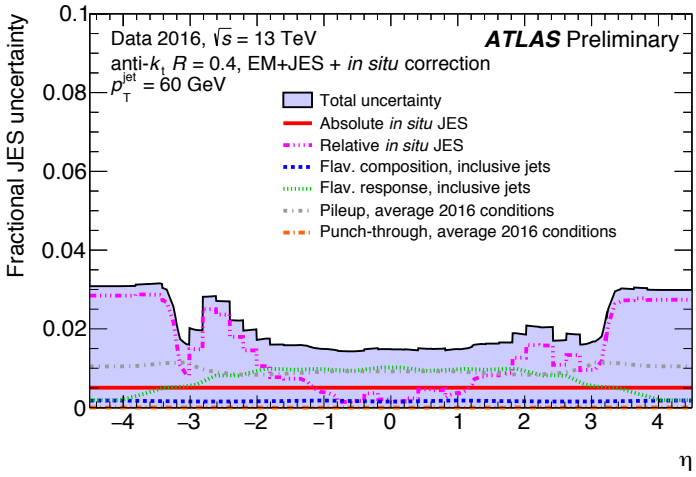

(b)

Figure 3.10: Fractional jet energy scale systematic uncertainty components, as a function of a) jet transverse momentum at $\eta = 0$ and b) η for jets with $p_{\mathrm{T}} = 60$ GeV [94].

3.6 *b*-tagging

The final state used in the search for Higgs boson pair production of this thesis is characterized by the presence of jets originating from b-quarks. The precise identification of

these b-jets is of paramount importance for selecting the HH signal and to reduce the contribution of some of the main backgrounds.

The b-tagging efficiency is defined as the rate at which true b-jets are being identified and is particular of each b-tagging algorithm. The true jet flavour is defined in simulated data using a spatial ΔR matching between stable hadrons and reconstructed jets. The matching is done hierarchically, the first step is to check if a b-hadron can be matched, followed by a charm hadron and finally a τ-jet. Therefore the jets are classified as b-jets, c-jets, τ-jets or light-jets (no match found).

Multiple algorithms are used in ATLAS [95], based on the information from reconstructed tracks and secondary vertices in the ID in order to identify b-jets, taking advantage of the b-hadron long lifetime.

Impact parameter based algorithms (IP2D, IP3D) [96], inclusive secondary vertex reconstruction algorithms (SV) [97] and decay reconstruction algorithms (JetFitter) are used. These algorithms are complementary to each other and can be combined using a multivariate function to create a single b-tagging discriminant (MV).

Impact parameter algorithms are based on the signed impact parameter significances, d_0/σ_{d_0} and z_0/σ_{z_0}, of the tracks matching to a jet. The impact parameters can be positive or negative based on the assumption that the decay point of the b-hadron lies along its paths. Therefore, tracks from b-hadron decays usually have positive impact parameters, indicating that they are originated in front of the primary vertex while tracks that are originated in the primary vertex will have equally negative or positive signs due to resolution effects.

Secondary vertex algorithms attempt to reconstruct an inclusive displaced secondary vertex which is formed by selected tracks within a jet. Vertices from long lived particles (K_s, Λ), photon conversions or hadron interactions with the detector are removed. A single inclusive vertex is reconstructed by iteratively removing outlier tracks until a good vertex candidate is identified. Also, the kinematic properties of the track can be used to offer discrimination power between b-jets and light-jets.

The multi-vertex decay chain algorithm attempts to reconstruct the weak decay chain of a b-hadron produced at the primary vertex that decays to a charm hadron, called tertiary vertex. A Kalman filter is used to identify b-hadron flight path assuming

that the tertiary vertex is in the same path. Track properties are also used to provide discrimination power.

The three types of algorithms provide input to a multivariate classifier. The second high-level b-tagging algorithm used for the search of this thesis is DL1r [98], where DL1 is based on a deep feed-forward neural network (NN) and "r" stands for recurrent where the output of the DL1 algorithm is used as input for the same algorithm in order to improve the efficiency. The DL1 NN has a multidimensional output corresponding to the probabilities for a jet to be a b-jet, c-jet or a light-jet. The input variables for DL1 are the same of those used in the previous MV2 algorithm with the addition of the JetFitter c-tagging variables [99]. The DL1 algorithm parameters include the architecture of the NN, the number of training epochs, the learning rates and training batch size. The final DL1 b-tagging discriminant is defined as:

$$D_{\mathrm{DL1}} = ln\left(\frac{p_b}{f_c p_c + (1 - f_c) p_{\mathrm{light}}}\right) \tag{3.3}$$

where p_b, p_c, p_{light} and f_c represent respectively the b-jet, c-jet and light-flavour jet probabilities, and the effective c-jet fraction in the background training sample, respectively. The output discriminants of the DL1 b-tagging algorithms for b-jets, c-jets and light-jets in the baseline $t\bar{t}$ simulated events are shown in Figure 3.11.

The evaluation of the performance of the algorithms is carried out using b-jet tagging single-cut operating points. These are based on a fixed selection requirement on the b-tagging algorithm discriminant distribution ensuring a specific b-jet tagging efficiency, ϵ_b, for the b-jets present in the baseline $t\bar{t}$ simulated sample. The efficiency of the different algorithms can be seen in Figure 3.12.

3.7 Missing transverse energy

Neutrinos or other weakly interacting particles that are produced in pp collisions at the LHC will not interact with the ATLAS detector and therefore will escape undetected. Indirect information of these particles can be obtained imposing the momentum conservation in the transverse plane to the beam direction. The initial state has zero momentum component in the transverse plane, therefore an imbalance in the total mea-

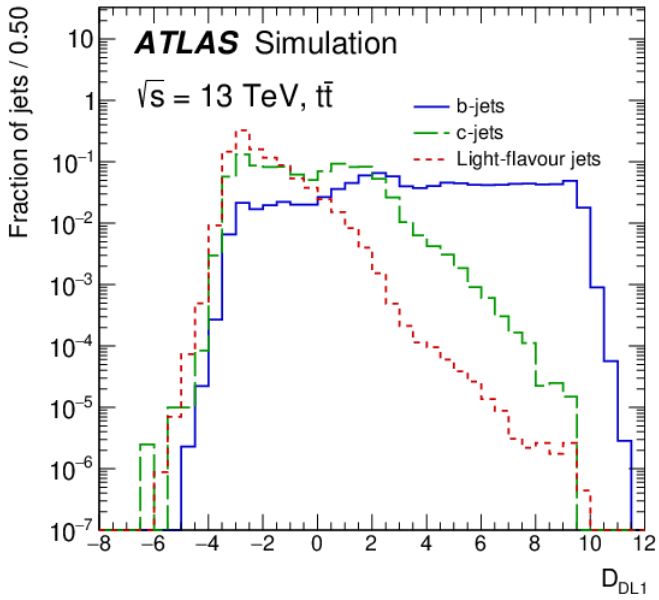

Figure 3.11: Distribution of the output discriminant of the DL1 b-tagging algorithm for b-jets, c-jets and light-jets in the baseline $t\bar{t}$ simulated events [99].

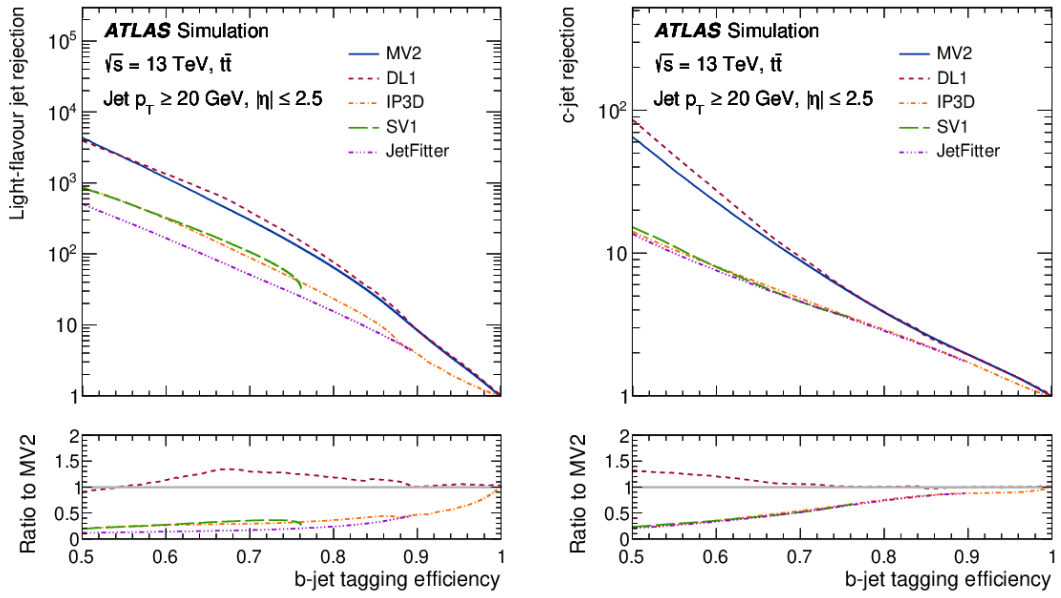

(a) (b)

Figure 3.12: The (a) light-jet and (b) c-jet rejections versus the b-jet tagging efficiency for the IP3D, SV1, JetFitter, MV2 and DL1 b-tagging algorithms evaluated on $t\bar{t}$ events.

sured transverse momentum in the final state implies the presence of an invisible particle to the detector.

The missing transverse momentum $\overrightarrow{E}_{\mathrm{T}}^{\mathrm{miss}}$ is reconstructed as the negative vector sum of the transverse momentum $\overrightarrow{p}_{\mathrm{T}}$ of reconstructed physics objects. The magnitude of the vector is defined as $E_{\mathrm{T}}^{\mathrm{miss}}$. The objects that are considered in the $E_{\mathrm{T}}^{\mathrm{miss}}$ calculation are electrons, photons, muons, τ-leptons and jets and are known as hard terms. Soft terms are reconstructed momenta of particles not associated to any hard term and are also included in the $E_{\mathrm{T}}^{\mathrm{miss}}$ calculation. The algorithm used for soft term reconstruction in ATLAS relies on tracks and it is called Track Soft Term (TST).

The $E_{\mathrm{T}}^{\mathrm{miss}}$ resolution is highly related to the removal of pile-up jets. The algorithm used to extract pile-up jets is the jet-vertex-tagger (JVT) that uses the track-to-vertex method [100]. In addition, a forward pile-up tagging technique (fJVT) exploits the correlation between central and forward jets that are originated from pile-up interactions [101]. Figure 3.13 shows the $E_{\mathrm{T}}^{\mathrm{miss}}$ resolution improvement in high pile-up conditions using fJVT.

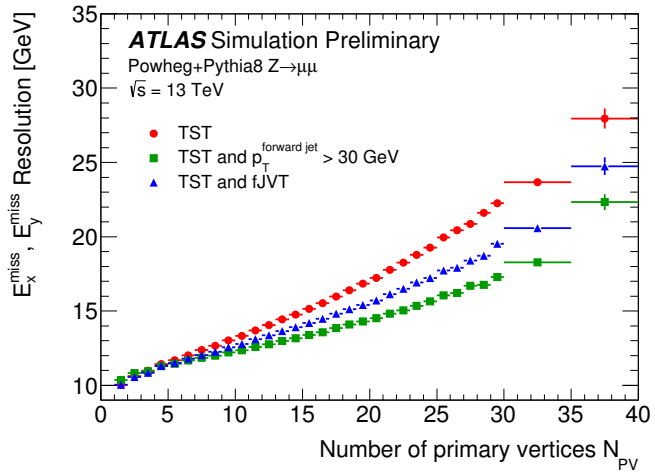

Figure 3.13: The Track Soft Term $E_{\mathrm{T}}^{\mathrm{miss}}$ resolution as a function of N_{PV} measured in MC simulated $Z \to \mu\mu$ events using different strategies for pile-up suppression [102].

The TST performance is validated using $Z \to \ell\ell$, $W \to \ell\nu$ and $t\bar{t}$ events. The agreement of TST $E_{\mathrm{T}}^{\mathrm{miss}}$ between data and MC simulation can be seen in Figure 3.14a with $Z \to ee$ events.

TST systematic uncertainties are calculated using the differences between data and

MC from the balance of a soft term object and a calibrated physics object. The systematic uncertainty of each hard term is also propagated to $E_{\mathrm{T}}^{\mathrm{miss}}$. Figure 3.14b shows the mean of the TST distribution as a function of the hard term p_{T} for 36.5 fb^{-1} of data taken by ATLAS during Run 2.

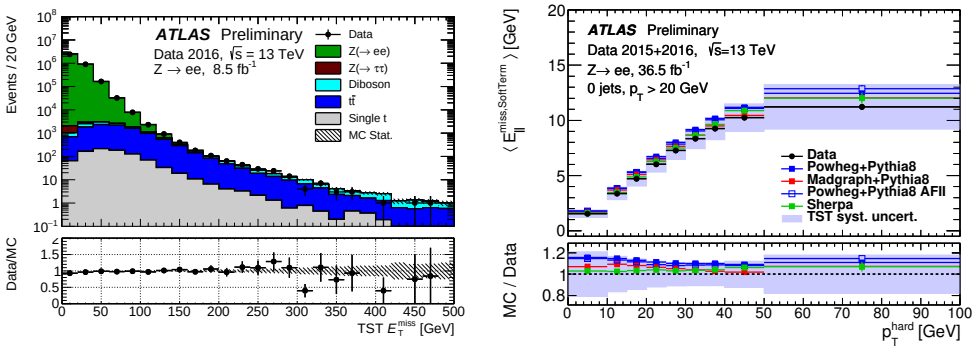

(a) (b)

Figure 3.14: a) TST $E_{\mathrm{T}}^{\mathrm{miss}}$ distribution for a selection of Z boson decays to a pair of electrons at Run 2 ATLAS data. The expectation is superimposed by POWHEG+PYTHIA8 MC simulated events for the relevant signal physics processes including some background processes while diboson backgrounds use SHERPA [103]. b) The mean of the TST distribution projected in the direction longitudinal to the hard term p_{T} for $Z \to ee$ events measured using Run 2 ATLAS data and MC simulation [102].

Chapter 4

Tile Calorimeter upgrades

As member of the ATLAS Collaboration, I have performed a series of tasks to qualify as author and to contribute to the development of the ATLAS detector and the LHC. During the Long Shutdown 2, an upgrade of the ATLAS experiment was performed. The upgrade consisted of refurbishments of the electronics, maintenance and upgrade of various detector components along with the installation of new detectors in order to keep with the increased luminosity that is expected during Run 3. These improvements increase ATLAS potential to spot new or rare physics processes and have required the installation and development of new hardware and software systems.

The High Luminosity upgrade of the LHC (HL-LHC) [104] will provide an instantaneous luminosity 7.5 times larger than the LHC design, in order to reach a dataset size of about 4000 fb^{-1}. Due to the very high luminosity, up to 200 simultaneous collisions are expected per bunch crossing. In preparation for the HL-LHC, the ATLAS experiment is undergoing a series of upgrades of the detector to cope with the increased radiation and to meet the requirements of a 1 MHz rate for the first trigger level output. In the case of the Tile Calorimeter, digitized signals from PMTs are sent to the back-end electronics and to the first level of trigger at 40 MHz, providing better trigger precision and allowing the development of more complex trigger algorithms.

One key element of the Tile Calorimeter upgrade is the TileCal Phase-II Demonstrator. The Demonstrator is an on-detector read-out electronics that consists of a superdrawer that partitions a legacy Tile Calorimeter drawer into four minidrawers,

each servicing up to 12 PMT channels. The superdrawer continuously digitizes two gains of up to 48 Tile Calorimeter PMTs and sends the digitized sampled data to the off-detector systems at 40 MHz. The Demonstrator has two different read-out paths, one through the legacy ROD-ROS read-out and another using the Phase-II Preprocessor-FELIX (PPr-FELIX) system.

During the detector operations, raw data are saved and then reconstructed with the ATLAS software framework (Athena) in order to obtain calibrated energy per cell and to perform data quality checks for monitoring.

In the legacy read-out, the ROD transmits the Demonstrator data to the TDAQ data stream with the legacy data format allowing the reconstruction of the data in Athena. The legacy data format is formed by 7 10-bit samples for each channel.

In the PPr-FELIX read-out, the data format is different and therefore a new bytestream converter is needed to reconstruct this data in Athena. In addition to this step, the signal reconstruction algorithms (Optimal Filtering) and the associated tools available in Athena have to be updated to process the new data format formed by 16 12-bit samples for each channel.

In addition, the ATLAS software framework has undergone during the LS2 a migration to the so called AthenaMT where multi-thread processes are used to exploit more efficiently modern CPUs processing power and memory footprint.

4.1 AthenaMT migration

ATLAS software framework, based on Gaudi [105] and Athena [106], was designed to process serially one event at a time. The limitations of existing computing technology, along with the requirements of the ATLAS reconstruction environment for higher luminosity and the emergence of new computing methodologies, has forced multi-threaded implementations [107] for Run 3. The key requirements are the reduction of the maintenance overhead and the effective usage of the hardware resources.

To reduce the maintenance overhead, a common multi-threaded framework, AthenaMT [108] has been proposed. This framework is designed to meet offline and trigger requirements, eliminating the need for a custom trigger-specific layer. Data and

control flow, as well as regional reconstruction are part of the scheduler. The scheduler is a service that executes algorithms and stores their states in order to determine in an event which algorithm should be executed next. It runs in a dedicated thread using two thread-safe queues to communicate with the framework. All algorithms that can be executed are added to the scheduled queue and ordered based on a priority.

The data flow is expressed via data dependencies, in the form of ReadHandles and WriteHandles. An algorithm takes one or more inputs ReadHandles (that can be from other algorithms or directly from the initial detector data) and performs a transformation in order to create one or more output objects that are published in the WriteHandler. This information is known prior to the execution of the first event and is used by the Run 3 Gaudi scheduler to generate the dependencies and control the order in which algorithm run for each event. Algorithms with no common dependencies (as can be tracking or calorimeter reconstruction) can run in parallel. An example of an electron algorithm with independent tracking and calorimeter reconstruction is shown in Figure 4.1.

The control flow is defined as a set of conditions that allow the scheduler to avoid unnecessary processing. If an event contains, for instance, only low momentum jets, subsequent algorithms related to high momentum jet substructure calculations can be skipped.

Regional reconstruction is expressed via EventViews, which confine an algorithm to a given geometric region. This is transparent to the algorithms that request data via ReadHandles and receive only data in the given region.

This new structure requires the migration of the current Athena framework to a multi-thread framework capable of processing asynchronous data in a core-safe way. Therefore the ATLAS monitoring system, among others, had to be migrated to the new AthenaMT framework.

As part of my contribution to the AthenaMT migration I have worked on the TileMonitoring package, adapting the TileTMDBRawChannel and TileTMDBDigitsMonitor algorithms to the new multi-thread framework.

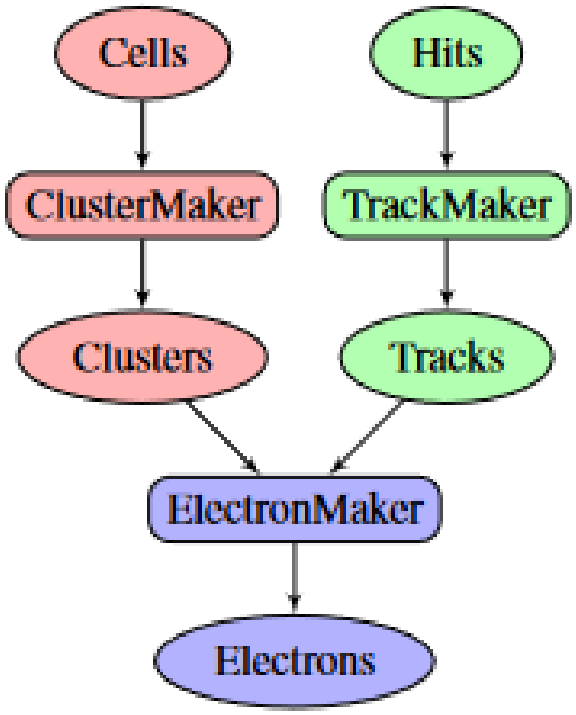

Figure 4.1: Data dependencies for electron reconstructions [109].

TileTMDBRawChannelMonTool

The TileTMDBRawChannelMonTool is a monitoring algorithm of the "Tile Muon Digitizer Board" (TMDB) inside the TileMonitoring package that takes raw data as input and monitors the digital noise. The output are histograms of energy amplitudes, timing distributions, coincidences of muon impact positions in the TGC and muon signals in the TMDB.

As part of the ATLAS monitoring system, this algorithm has been migrated to the AthenaMT framework. The algorithm determines automatically if data files are generated from "Digital Signal Processing" (DSP) inputs. If data are not from DSP inputs, the algorithm books timing histograms, as shown in Figure 4.2, and amplitude histograms is shown in Figure 4.3. If data are from DSP inputs, only amplitude histograms are booked and the range is dynamically changed to the expected range.

A flag to help the Level 1 muon trigger is used to suppress spurious trigger signals

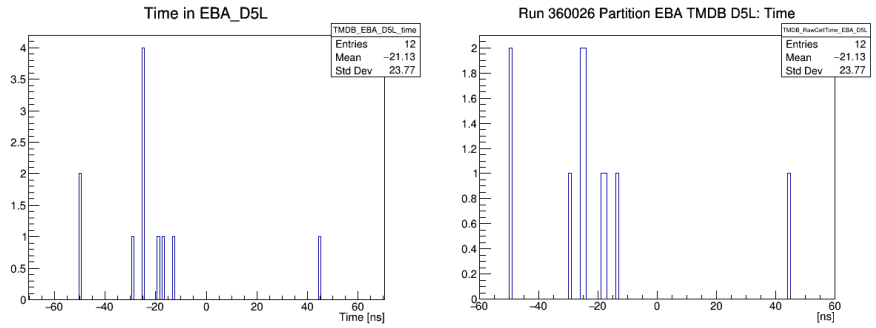

Figure 4.2: Comparison between (a) legacy time reconstruction and (b) migrated time reconstruction for non DSP inputs. Difference is coming from a different binning criteria.

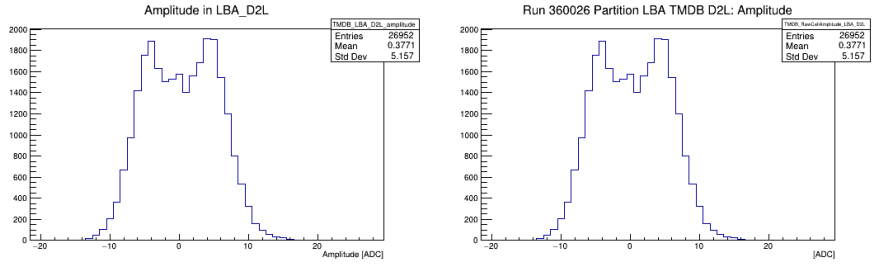

Figure 4.3: Comparison between (a) legacy amplitude reconstruction and (b) migrated amplitude reconstruction for non DSP inputs.

by looking for coincidences of energy deposition in the D-Layer of the Tile Calorimeter Extended Barrel A and C sides with the TGC inner chambers. The histograms are generated based on reconstructed muons in the TGC trigger sectors in correspondence to EBA and EBC angular coverage and based on coincidences with EBA(C) in D6(+D5) for 500(600) MeV as shown in Figure 4.4.

TileTMDBDigitsMonitorAlgorithm

The TileTMDBDigitsMonitorAlgorithm is a monitoring algorithm inside the TileMonitoring package that takes raw data as input and monitors the digital noise whose output are histograms of pedestal values, high frequency noise (mean RMS of the 7 samples of each read-out channel of each event), and energy amplitude for each partition and cell along with a 2D Profile where the y-axis is the cell and the x-axis is the drawer.

Figure 4.5 shows the reconstructed amplitude for the legacy Athena algorithm on the left and the new migrated AthenaMT algorithm on the right.

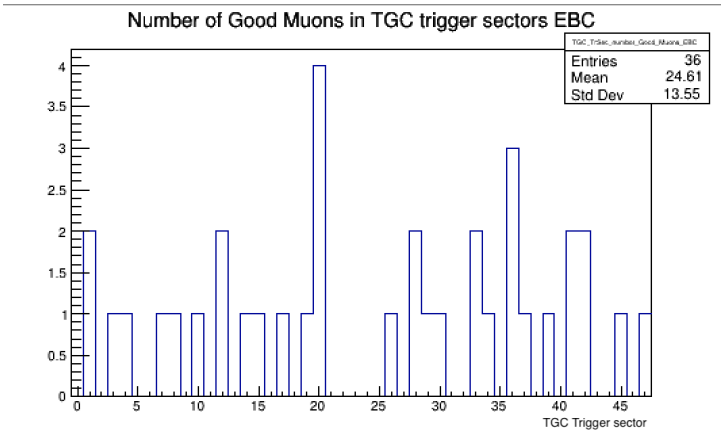

Figure 4.4: Migrated muon impact positions in coincidence with the Tile Calorimeter D5 layer. Note that only a fraction of the data is shown.

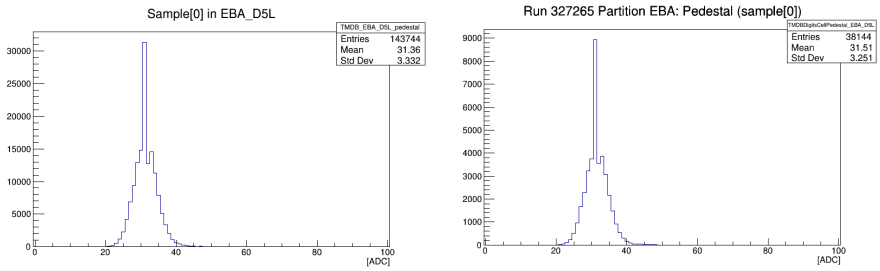

Figure 4.5: Comparison between (a) legacy amplitude reconstruction and (b) amplitude reconstruction for the migrated TileTMDBDigitsMonitorAlgorithm.

4.2 Tile Calorimeter upgrade for HL-LHC

4.2.1 Introduction

The HL-LHC will have a peak luminosity 7.5 times higher than the design luminosity of the LHC. Therefore, the ATLAS Tile Calorimeter is undergoing a series of upgrades in preparation for the HL-LHC. TileCal Phase-II upgrade [110] for the HL-LHC will allow the system to cope with the increased radiation levels and out of time pile-up. The upgraded system will digitize and send all the calorimeter signals to the off-detector systems, where the events will be reconstructed and sent to the first level trigger at 40 MHz rate.

The goals of the TileCal Phase-II upgrade are the replacement of the aging electronics, the increase of radiation tolerance, the improvement of system reliability, the increase of data precision and the improvement of the first level trigger system rates.

The overall goal of the ATLAS Trigger and Data Acquisition (TDAQ) system upgrade is to be able to operate at the High Luminosity LHC (HL-LHC) [111]. The TDAQ Phase-II Upgrade Project [110] is designing, building and installing new trigger and data acquisition hardware along with its firmware and software during the Long Shutdown 3 of the LHC in 2028.

4.2.2 TilePreProcessor

For the HL-LHC new off-detector electronics architecture has been developed, the Tile PreProcessor (TilePPr), designed to replace the current ROD system. Along with new electronics developments, modifications to the Tile Calorimeter mechanics are also considered. Each drawer is going to be splitted into four "mini-drawers" in order to improve the accessibility to the Tile Calorimeter on-detector electronics.

The TilePPr can be operated in legacy and Phase-II mode. In legacy mode, the TilePPr emulates the legacy front-end electronics. The Phase-II and legacy systems operate in parallel and are synchronized using the clock and trigger information distributed via dedicated optical links from the legacy TTC modules. The TilePPr adds trigger identification information to the data packets, which is used for synchronization at the read-out driver level.

In addition, the TilePPr prototype implements the Phase-II read-out architecture, which can be used in standalone mode or in parallel with the legacy system. The TilePPr operated within the legacy infrastructure transfers the triggered data through a high-speed optical link to the FELIX system, which saves the data on a local disk for offline reconstruction and analysis.

The TilePPr uses 16 asymmetric GigaBit Transceiver (GBT) running at 4.8 Gbps for the downlink (TilePPr to front-end) and 9.6 Gbps for the uplink (front-end to TilePPr). Detector Control System (DCS) commands and Trigger, Timing and Control (TTC) information are encoded and transmitted to the downlink at a data rate of 4.8 Gbps. In the front-end electronics the daughterboard decodes and executes the received commands, sending an acknowledgment receipt to the TilePPr.

4.2.3 FELIX system

After the LHC Long Shutdown 2 (2019-2021), the ATLAS experiment operates in an increasingly harsh collision environment. The LHC will deliver instantaneous luminosities two times the original design value and increase the number of interactions per bunch crossing. In order to maintain physics performance, ATLAS has undergone a series of upgrades during the Long Shutdown 2. To this end, the Frond-END Link eXchange (FELIX) system is being developed. FELIX is a new read-out component, developed as part of the ATLAS TDAQ upgrade effort. FELIX acts as the interface between the data acquisition, detector control and TTC systems, and an updated trigger and detector front-end electronics. Therefore, FELIX functions as a router between custom and radiation tolerant serial links from front-end ASICs and FPGAs to data collection and processing components via a commodity switched network.

The FELIX system is also in charge of distributing the input from the TTC system. The LHC clock and trigger information are distributed to both on-detector electronics with low and fixed latency via GBT links and to network endpoints.

In Run 3, FELIX will be used by the LAr Calorimeter, the Level-1 Calorimeter trigger system, BIS 7/8, and the New Small Wheel (NSW) muon detector. Starting from Run 4 FELIX will read-out the entire ATLAS detector.

4.2.4 Raw data

Currently, the TileCal Phase-II Demonstrator has two different read-out paths, one through the legacy ROD and another one using the TilePPr system. Raw data are saved and then reconstructed in the ATLAS software framework (Athena) [112] to obtain calibrated energy per cell and to perform data quality checks for monitoring.

In the legacy read-out system, the ROD introduces the Demonstrator data into the TDAQ data stream with the correct data format allowing the reconstruction of the data in Athena.

In the FELIX read-out, the data format of the TilePPr is different and a bytestream converter (decoder) is needed to reconstruct the data in Athena. The data are organized in e-groups of 16 bits each. Each e-group is composed of up to 8 e-links. The e-groups are

synchronous with the TTC clock: data are being transferred with a 40 MHz frequency. There are four possible e-link data widths: 2, 4, 8 and 16 bits, corresponding to data rates of 80, 160, 320 and 640 MB/s for each link.

Two modules have been tested with the PPr-FELIX read-out, the event format will follow the structure:

- Run parameters, starting with the word (0x1234aaaa)
- Full event fragment, with the header (0xaa1234aa)
- ROB Fragment (0xdd1234dd)
- ROD Fragment (0xee1234ee)
- LB side with minidrawers 01-d4 (8 minidrawers)
- Sub Fragment (0xff1234ff)
- EB side with minidrawers 41-4d (8 minidrawers)

Since both read-outs simultaneously provided by the Demonstrator, we have the capability to compare the reconstruction of the data using the legacy data format and the data using the new TilePPr data format, as described in Table 4.1.

	Legacy	TilePPr
Samples	7	16
Amplitude's bits	10	12
Read-out gains	1-2	2

Table 4.1: Differences between TilePPr and Legacy data formats.

In order to validate the new bytestream converter, a comparison of the reconstructed energy is done using two methods, the Optimal Filtering (Opt2) algorithm and the Fit Method (Fit) algorithm.

To make the comparison we have to keep in mind that we are comparing amplitudes encoded with a different number of bits. HL-LHC data format has 4 times finer granularity than the legacy read-out. Let's suppose that for a given channel the amplitude for the TilePPr read-out is 2134 ADC counts, the same amplitude in the legacy read-out

will be 533 ADC counts. In order to compare TilePPr and legacy read-outs a factor 4 is introduced to account for the bit difference between both, meaning that the peak in the legacy read-out of 533 ADC would be translated to a TilePPr peak of 2132 ADC counts. Thus, there is an expected average difference of 1.5 ADC counts between the TilePPr and legacy read-outs. In order to remove this granularity effect, the comparison is modified so that an increase of 4 ADC counts in the TilePPr system is translated to an increase of 1 ADC count in the Legacy system (TilePPr values like 2000, 2001, 2002, 2003 are treated as the same value, 2000).

Fit Method

Figure 4.6 shows the comparison of the reconstruction of amplitudes of the TilePPr and legacy, with respect to the legacy amplitude. Two possible comparisons are performed:

- A comparison of the 16 12-bit samples from TilePPr against the 7 10-bit samples from the legacy read-out, where legacy amplitudes are multiplied by a factor of four. This comparison is shown in Figure 4.6 (a), where the difference goes up to 6-7 ADC counts. To understand this difference a more in depth study is needed. In the occurrence of the following readout example:

  - TilePPr read-out ADC samples = [2052,2051,2052,2053,2041,2040,2050,2094,2084,2057, 2053,2051,2053,2051,2052,2052] ADC counts
  - TilePPr pedestal = 2049 ADC counts
  - TilePPr amplitude $\approx$ 46 ADC counts
  - Legacy read-out samples = [510,510,512,523,521,514,513] ADC counts
  - Legacy pedestal = 510 ADC counts
  - Legacy amplitude $\approx$ 14 ADC counts

  The read-out comparison provides the following difference, 4$\times$legacy amplitude - TilePPr amplitude = $4 \times 14 - 46 = 10$ ADC counts.

- A comparison of the 7 intermediate 12-bit samples from TilePPr against the 7-10 bit samples from the legacy read-out. The legacy amplitudes are multiplied by a

factor of four. This comparison is shown in Figure 4.6 (b), where the difference goes up to 1-2 ADC counts. This difference is coming from the different granularity between the systems and it is in the expected range.

These comparisons show that the TilePPr system is providing more precision and that there are differences arising from the increased number in samples and from the different number of bits of the amplitudes.

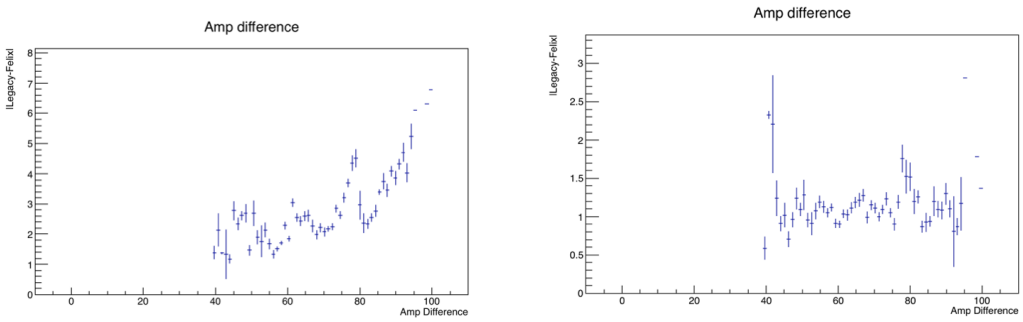

Figure 4.6: Difference (4×Legacy-TilePPr amplitude) between (a) legacy and TilePPr amplitudes using all 16 samples from TilePPr and (b) legacy and TilePPr amplitudes using the intermediate 7 samples from TilePPr respect to the legacy amplitude.

Optimal Filtering

The Optimal Filtering algorithm [113] has been updated so that is able to reconstruct the energy through the legacy and the TilePPr systems.

Figure 4.7 shows the difference (4×legacy-TilePPr amplitudes) between the legacy and TilePPr systems of the reconstructed amplitude using the Optimal Filtering algorithm. The difference is expected to be 0, except when the amplitude is small. This is due to the noise threshold that must be adjusted for TilePPr since the algorithm was designed for the legacy system and there is a factor 4 in the TilePPr ADC count values that has to be taken into account when setting the noise threshold.

Figure 4.8 shows the difference of the amplitudes reconstructed by the TilePPr and the legacy systems after removing the truncation effect and after the adjustment of the noise threshold ($|\text{Pedestal} - \text{Peak}| < 3$ ADC counts) for the TilePPr algorithm.

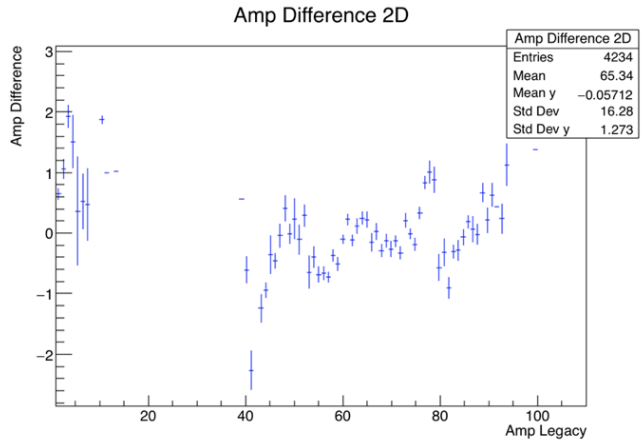

Figure 4.7: Difference (4×legacy-TilePPr amplitude) between the legacy and TilePPr reconstructed amplitudes using the Optimal Filtering algorithm.

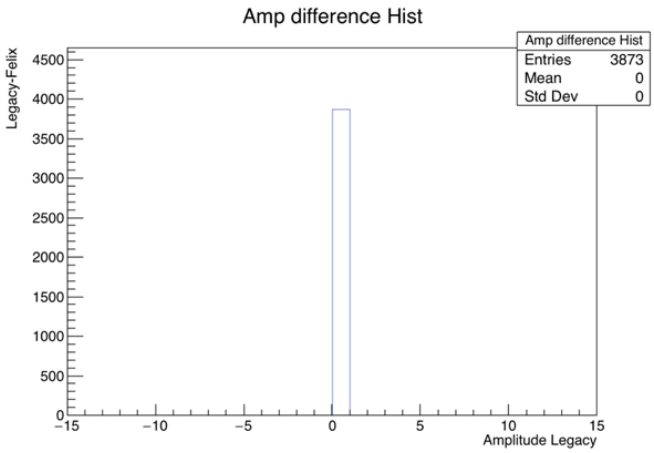

Figure 4.8: Difference between legacy and TilePPr reconstructed amplitudes using the Optimal Filtering algorithm after adapting the noise threshold for the TilePPr read-out.

4.2.5 Tile Monitoring implementation

The implementation of the Tile electronics, TilePPr, needs also the implementation of new monitoring algorithms. For that reason, the TileDigitsFlxMonitorAlgorithm has been implemented inside the TileMonitoring package using the AthenaMT framework.

The TileDigitsFlxMonitorAlgorithm creates sample distribution histograms for each channel and partition as shown in Figure 4.9.

TileDigitsFlxMonitorAlgorithm also creates histograms for high frequency noise (HFN) as shown in Figure 4.10 (a), where typical HFN for the TilePPr (legacy) system is 4.8 (1.2) ADC counts for low gain and 8 (2) ADC counts for high gain. Figure 4.10

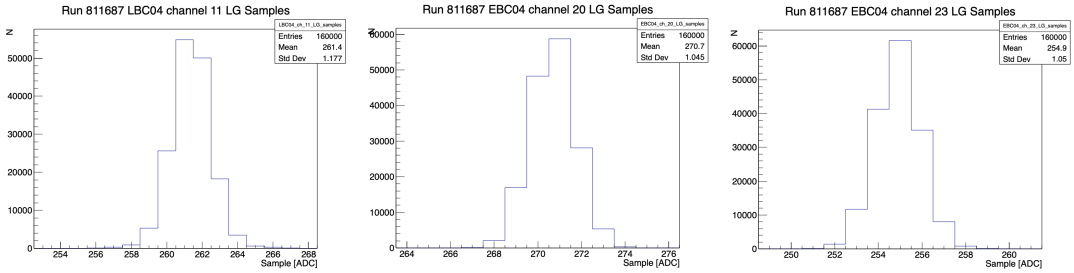

Figure 4.9: Sample distributions in ADC counts for (a) "Low Gain" (LG) LBC04 channel 11, (b) LG EBC04 channel 20 and (c) LG EBC04 channel 23.

(b) shows the distribution of the pedestal in high gain for all channels of the LBC04 module.

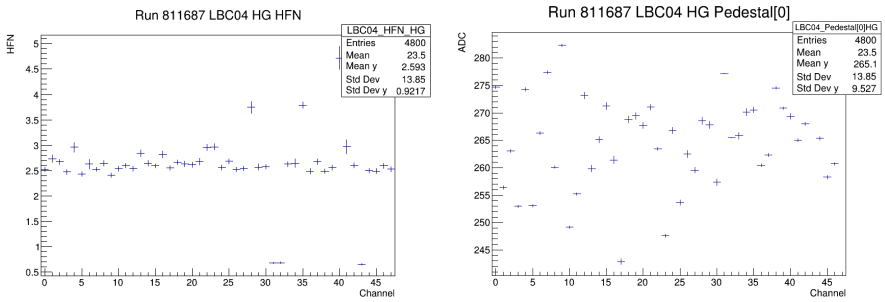

Figure 4.10: (a) HFN noise for LBC04 High Gain and (b) pedestal distribution for LBC04 High Gain.

Chapter 5

Search for Higgs boson pair production in the $HH \to b\bar{b}\gamma\gamma$ final state

5.1 Introduction

A search for the Higgs boson pairs in the $b\bar{b}\gamma\gamma$ final state is presented. The analysis is divided in two parts: the resonant search and the non-resonant search.

The resonant search is motivated by BSM theories predicting heavy particles that can decay into a pair of Higgs bosons, as shown in Figure 5.1. Such theories include models with two Higgs doublets [114], like the minimal supersymmetric extension of the SM [115], twin Higgs models [116] and composite Higgs models [117], adding a second complex doublet to the Higgs sector.

Non-resonant searches are motivated by the need to understand the Higgs boson self-coupling, predicted by the EW symmetry breaking. At leading order (LO) the production of Higgs boson pairs via ggF proceeds through the two diagrams shown in Figure 5.2. These diagrams interfere destructively, resulting in a small production cross section [118–120]. The ggF cross section calculated at next-to-next-to-leading-order (NNLO), for 13 TeV pp collisions and a Higgs boson mass of $m_H = 125.09$ GeV, in finite top mass approximation (FTapprox) is $\sigma_{HH}(\text{ggF}) = 31.02^{+2.2\%}_{-5.0\%}(\text{Scale})\pm 3.0\%(\alpha_S +$

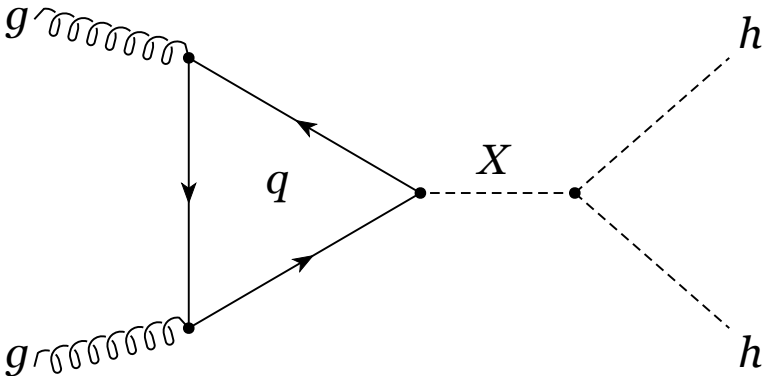

Figure 5.1: Gluon-gluon fusion production of a heavy resonance decaying into a Higgs boson pair.

PDF)$^{+4\%}_{-18\%}(m_t)$ fb [121], where "Scale" represents the uncertainty due to missing higher order quantum chromodynamics (QCD) calculations, "$\alpha_S + \text{PDF}$" the uncertainties on the strong coupling constant and parton distribution functions, and finally "m_t" is the uncertainty related to the top-quark mass [122,123], which is linearly added to the Scale uncertainty.

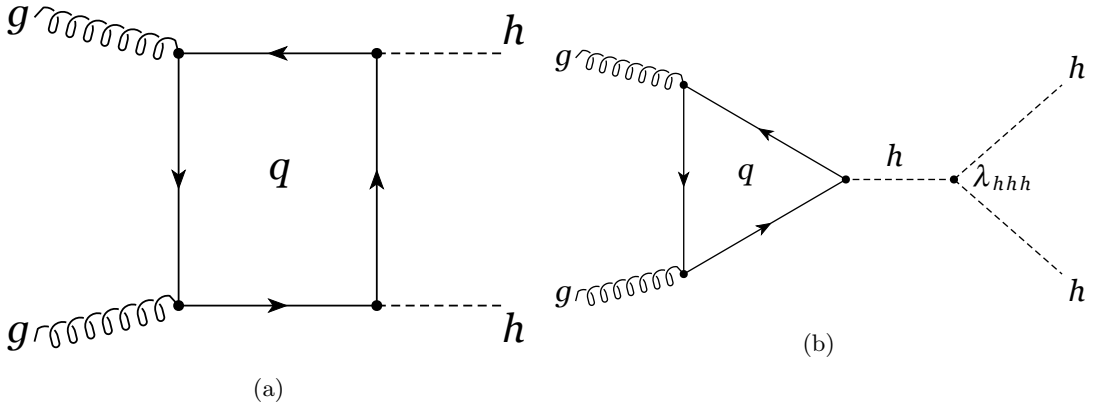

Figure 5.2: The Feynman diagrams for the dominant gluon-gluon fusion production process. In the Standard Model, (a) the trilinear coupling process, (b) the box diagram, and the destructive interference between the two processes, contribute to the total cross section. In the figure, κ_λ represents the Higgs boson trilinear coupling modifier.

The di-Higgs vector-boson fusion (VBF) production cross section, calculated at Next-to-Next-to-Next-to-Leading-Order (N3LO), is $\sigma_{HH}(\text{VBF}) = 1.72^{+0.03\%}_{-0.04\%}(\text{Scale}) \pm 2.1\%(\alpha_S + \text{PDF})$ fb [121] for $m_H = 125.09$ GeV, which is one order of magnitude lower than the cross section for the ggF process. The VBF production mode provides additional sensitivity of the Higgs trilinear coupling as can be seen in Figure 5.3. In

this thesis, the two leading production modes, ggF and VBF, of Higgs boson pairs are considered as signal. The rest of production mechanisms are neglected given their lower cross sections [124].

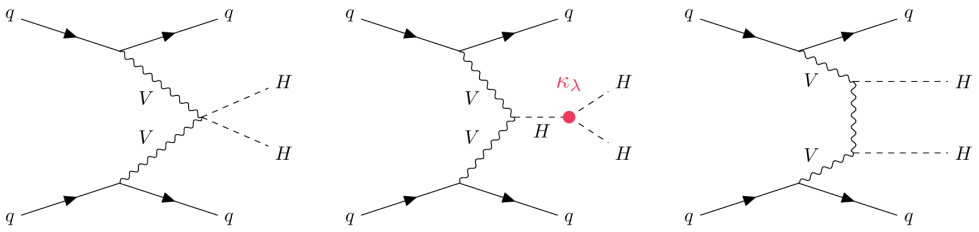

(a) $HHVV$ vertex (b) Trilinear coupling (c) VVH Production mode

Figure 5.3: The VBF production of Higgs boson pairs via (a) the $HHVV$ vertex, (b) the trilinear coupling, and (c) the VVH production mode. In the figure, κ_λ denotes the Higgs boson trilinear coupling modifier.

Non-resonant di-Higgs cross section can be enhanced by loop corrections involving new particles or by non-SM couplings between the Higgs boson and other SM particles. The non-resonant production cross section can also be modified if the trilinear self-coupling λ_{HHH} is different from what the SM predicts [125, 126]. This effect can be observed by a scale factor defined as $\kappa_\lambda \equiv \lambda_{HHH}/\lambda^{SM}_{HHH}$, where λ^{SM}_{HHH} is the SM value of the trilinear self-coupling.

In this section a search for di-Higgs production in the $b\bar{b}\gamma\gamma$ final state for the resonant and non-resonant production hypotheses is presented. The analysis considers the full Run 2 data set of 139 fb^{-1} at $\sqrt{s} = 13$ TeV. The event selection strategy for both the resonant and non-resonant analyses is based on multivariate methods designed to reject background processes, the statistical result is finally obtained fitting the diphoton invariant mass $m_{\gamma\gamma}$. The resonant search focuses on a narrow-width scalar particle X in the mass range of 251 GeV $\leq m_X \leq$ 1000 GeV. The selection depends on the mass of the considered scalar particle. For the non-resonant search, events are divided in different categories based on the reconstructed di-Higgs invariant mass targeting different κ_λ ranges. The main background processes are diphoton-plus-jets production and processes where a Higgs boson decays into a pair of photons. For the resonant search, the non-resonant HH production according to the SM prediction is considered as background. Interference effects between resonant and non-resonant HH production are neglected.

5.2 Data and simulation samples

The analysis uses pp collision data collected by the ATLAS experiment from 2015 to 2018 with proton beams colliding at a centre-of-mass energy of $\sqrt{s} = 13$ TeV. After data quality requirements [127], the full data set presents an integrated luminosity of 139.0 ± 2.4 fb^{-1} [128].

Monte Carlo simulations are used for signals and most of the background processes. Background from final states with jets wrongly identified as photons (originating from γ-jet and di-jets backgrounds are estimated using a data-driven technique.

The heavy spin-0 resonance X production via ggF and its decay into a pair of Higgs bosons ($pp \to X \to HH$) is simulated using `MADGRAPH5_aMC NLO` v2.6.1 [129] at LO accuracy with the `NNPDF2.3lo` PDF set. The parton shower, hadronization and underlying event is interfaced with the event generator `HERWIG` 7.1.3 [130, 131]. The resonance X mass ranges between 251 GeV and 1000 GeV at simulation level. A width of 10 MeV is used for all resonances. The eventual interference with non-resonant Higgs boson pair production is neglected.

Non-resonant HH production via ggF is generated at next-to-leading order accuracy in QCD with finite top-quark mass in both the real and virtual corrections (NLO FT) [119] using `POWHEG BOX` v2 [132] as event generator in the finite top-quark mass approximation with the `PDF4LHC15` parton distribution set [133]. The parton shower, hadronization and underlying event are generated by `PYTHIA` 8.244. Also, `HERWIG` 7.1.6 is used as an alternative generator to calculate the theory uncertainty from the parton shower. Samples are generated for $\kappa_\lambda = 1$ and 10.

The rest of the non-resonant ggF samples at different κ_λ are obtained using a reweighting method. The reweighting method derives the scale factors as a function of κ_λ in bins of m_{HH} by performing a linear combination of samples generated at different κ_λ values. The reweighting method [134] is validated by comparing the $m_{\gamma\gamma}$ distribution and event yields in the generated $\kappa_\lambda = 10$ sample and the $\kappa_\lambda = 1$ sample reweighted to $\kappa_\lambda = 10$. A systematic uncertainty in the range of 3-4% is associated with the reweighting process, based on the observed maximum difference. The inclusive cross section is then normalized for each κ_λ value [135].

Events from VBF non-resonant HH are generated at LO using `MADGRAPH5_aMC NLO` v2.6.0 [129]. The `NNPDF3.0nlo` set interfaced with `PYTHIA` 8.244 is used in the matrix element calculation. Samples are generated at LO for four values of the coupling modifier $\kappa_\lambda = 0, 1, 2$ and 10. The N3LO to LO cross section ratio at the SM value is obtained and applied to the VBF HH cross section. These samples are used to parametrize the signal yields in the signal region as a function of κ_λ fitting with a second order polynomial to the MC predictions.

Production of single Higgs boson via the ggF, VBF, WH, ZH ($qq \to ZH$ and $gg \to ZH$), $t\bar{t}H$, tH ($tHqj$ and tHW) and bbH processes have been modeled using the MC samples described in Ref. [127]. A Higgs boson mass of 125 GeV has been assumed for all production processes. The analysis presented in this thesis assumes a branching ratio of 0.227% for Higgs boson decaying into two photons and a branching ratio of 58.2% for the Higgs boson decay into two b-quarks [136].

Finally, the $\gamma\gamma$+jets process has been simulated with the SHERPA 2.2.4. generator QCD NLO-accurate matrix elements for up to one parton, and LO-accurate matrix elements for up to three partons, were calculated with COMIX [137] and OpenLoop [138–140] libraries. These samples are calculated in the 5-flavour scheme including b-quarks in the massless approximation and then merged with the SHERPA parton shower [141] using the MEPS NLO prescription [142, 143] with a dynamic merging cut [144] of 10 GeV. At the parton shower effect, b-quarks are treated as massive particles. Events from $t\bar{t}\gamma\gamma$ processes are produced with `MADGRAPH5_aMC NLO` in the 4-flavour scheme [129]. The summary of all simulation samples that have been considered in the analysis is listed in Table 5.1. A full simulation of the ATLAS detector based on `GEANT4` [145] is used to reproduce the detector response to single Higgs boson processes. The continuum background, a combination of $\gamma\gamma$, γ-jet and di-jets events, and the signal samples are simulated using `ATLASFAST II` [146], a fast simulation of the ATLAS detector response which have been shown to be able to accurately simulate di-photon Events.

For all samples the detector is simulated using Geant4, except for the signal samples and continuum background, where fast simulation is used.

Table 5.1: Summary of nominal Higgs boson pair signal samples and single-Higgs-boson background samples, split by production mode, and continuum background samples. The generator used in the simulation, the PDF set, and set of tuned parameters are also provided.

Process	Generator	PDF set	Showering	Tune
Nonresonant ggF HH	POWHEG BOX v2+FT	PDFLHC	PYTHIA 8.2	A14
Nonresonant VBF HH	MADGRAPH5_aMC NLO	NNPDF3.0nlo	PYTHIA 8.2	A14
Resonant ggF HH	MADGRAPH5_aMC NLO	NNPDF2.3lo	HERWIG 7.2.3	H7.1 - Default
ggF HH	NNLOPS	PDFLHC	PYTHIA 8.2	AZNLO
VBF HH	POWHEG BOX v2	PDFLHC	PYTHIA 8.2	AZNLO
WH	POWHEG BOX v2	PDFLHC	PYTHIA 8.2	AZNLO
$qq \to ZH$	POWHEG BOX v2	PDFLHC	PYTHIA 8.2	AZNLO
$gg \to ZH$	POWHEG BOX v2	PDFLHC	PYTHIA 8.2	AZNLO
$t\bar{t}H$	POWHEG BOX v2	NNPDF3.0nlo	PYTHIA 8.2	A14
$b\bar{b}H$	POWHEG BOX v2	NNPDF3.0nlo	PYTHIA 8.2	A14
tHq	MADGRAPH5_aMC NLO	NNPDF3.0nlo	PYTHIA 8.2	A14
tHW	MADGRAPH5_aMC NLO	NNPDF3.0nlo	PYTHIA 8.2	A14
$\gamma\gamma$ +jets	SHERPA v2.2.4	NNPDF3.0nnlo	SHERPA v2.2.4	–
$t\bar{t}\gamma\gamma$	MADGRAPH5_aMC NLO	NNPDF2.3lo	PYTHIA 8.2	–

5.3 Event selection

Both resonant and non-resonant searches are based on multivariate analysis techniques to separate signal from background. There is a common preselection shared between the resonant and the non-resonant searches, afterwards events must fulfill different requirements for the two searches.

Common preselection

For both resonant and non-resonant analyses, events are pre-selected using di-photon triggers [147] requiring two reconstructed photon candidates with minimum transverse energies of 35 GeV for the leading and 25 GeV for the sub-leading photon. The leading (sub-leading) photon is defined as the photon candidate with the highest (second-highest) transverse energy [147]. Different photon identification criteria are used depending on the dataset:

- A "Loose" photon identification [148] criterion is used for both photons in the 2015 and 2016 di-photon riggers.
- A "Medium" photon identification [148] is used for the 2017-2018 period to cope with the increased instantaneous luminosity.

Once the full diphoton event selection described in this Section is applied, the average trigger efficiency for $H \to \gamma\gamma$ events is found to be greater than 99% for the 2015–2016 data-taking period, and greater than 98% for the 2017–2018 data-taking period.

The combined trigger efficiency is 82.9% for the non-resonant signal and 69.5% for the $m_X = 300$ GeV resonant signal. On top of the di-photon trigger requirements there are other requisites for an event to be selected. The definition of the reconstructed objects and the identification techniques have been described in Section 3.

- Events must contain two isolated photons passing a tight identification criterion.
- The di-photon invariant mass from the two leading photons must be in the range $105 < m_{\gamma\gamma} < 160$ GeV.
- The leading (sub-leading) photon must satisfy the relationship $p_{\mathrm{T}}/m_{\gamma\gamma} > 35\%(25\%)$.
- The event must have exactly two b-tagged jets passing a 77% working-point (WP) requirement, based on the DL1r b-tagging algorithm with a $p_{\mathrm{T}} > 25$ GeV for the b-jet.
- The event must contain exactly zero leptons with a $p_{\mathrm{T}} > 10$ GeV.
- Less than six central ($|\eta| < 2.5$ and $p_{\mathrm{T}} > 25$ GeV) jets are required. This requirement reduces the $t\bar{t}H$ contribution to the background where the top quarks decay hadronically.

For subsequent combinations with searches in other final states, the analysis must be orthogonal to the $HH \to b\bar{b}b\bar{b}$ event selection [149], therefore events with more than two b-jets passing the 77% WP requirement are rejected. Finally, multivariate techniques to target the ggF production mode are used. The resulting boosted decision tree (BDT) [150] categories are required to have at least 9 expected continuum background events in the range $105 < m_{\gamma\gamma} < 160$ GeV excluding the signal region $120 < m_{\gamma\gamma} < 130$ GeV. This requirement is needed to obtain enough sideband events to be able to perform a meaningful fit of the $m_{\gamma\gamma}$ distribution.

For this analysis we define $m^*_{b\bar{b}\gamma\gamma} = m_{b\bar{b}\gamma\gamma} - m_{b\bar{b}} - m_{\gamma\gamma} + 250$ GeV (being 250 GeV about twice the Higgs boson mass value). This variable improves the $m_{b\bar{b}\gamma\gamma}$ resolution due to the cancellation of detector resolution effects, particularly for the resonant analysis where the resonance signal decays into two Higgs bosons, as can be seen in Figure 5.4.

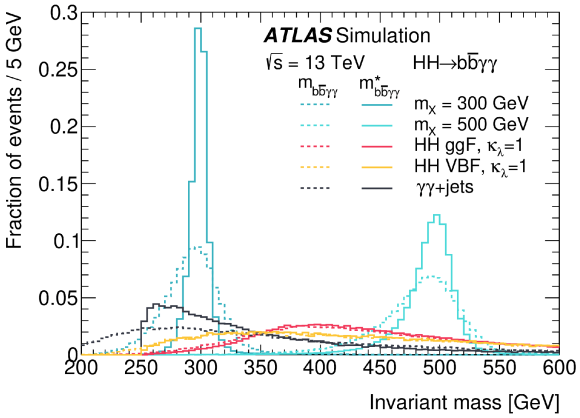

Figure 5.4: Reconstructed invariant mass for $m_X = 300$ GeV and $m_X = 500$ GeV resonant signal benchmarks, for the SM HH production processes and for the $\gamma\gamma$+jets background. Dashed lines represent the distribution of $m_{b\bar{b}\gamma\gamma}$ while solid lines represent the distribution of $m^*_{b\bar{b}\gamma\gamma}$ [151]. Distributions are normalized to unit area.

Resonant selection

The resonant analysis selection is based on a multivariate analysis using a BDT technique. For this analysis the TMVA toolkit [150] has been used. Two BDTs are trained to better separate signal from backgrounds of different nature: the $\gamma\gamma$+jets plus $t\bar{t}\gamma\gamma$ backgrounds (named $\text{BDT}_{\gamma\gamma}$) and another BDT focused on single Higgs boson background ($\text{BDT}_{\text{SingleH}}$), where the dominant backgrounds are $t\bar{t}H$ and ZH. The complete list of variables that have been used in the BDT training can be seen in Table 5.2. The $E_{\text{T}}^{\text{miss}}$ is also included for the training against single Higgs since it is particularly useful to reject the $t\bar{t}H$ background. The separation power of the MVA shown and the BDT score distribution of both MVAs are shown in Figure 5.5, where events are shown at pre-selection level.

Signal events are reweighted to match the $m^*_{b\bar{b}\gamma\gamma}$ distribution of the background events as shown in Figure 5.6. In this way the correlation between $m^*_{b\bar{b}\gamma\gamma}$ and the

Table 5.2: Variables used in the BDT for the resonant analysis. For variables depending on b-tagged jets, only jets b-tagged using the 77% working point are considered.

Variable	Definition
Photon-related kinematic variables	
$p_{\mathrm{T}}^{\gamma\gamma}$, $y^{\gamma\gamma}$	Transverse momentum and rapidity of the diphoton system.
$\Delta\phi_{\gamma\gamma}$ and $\Delta R_{\gamma\gamma}$	Azimuthal angle and ΔR between the two photons.
Jet-related kinematic variables	
$m_{b\bar{b}}$, $p_{\mathrm{T}}^{b\bar{b}}$ and $y_{b\bar{b}}$	Invariant mass, transverse momentum and rapidity of the b-tagged jets system.
$\Delta\phi_{b\bar{b}}$ and $\Delta R_{b\bar{b}}$	Azimuthal angle and ΔR between the two b-tagged jets.
N_{jets} and $N_{b\text{-jets}}$	Number of jets and number of b-tagged jets.
H_{T}	Scalar sum of the p_{T} of the jets in the event.
Diphoton+di-jets-related kinematic variables	
$m^{*}_{b\bar{b}\gamma\gamma}$	Invariant mass of the diphoton plus b-tagged jets system.
$\Delta y_{\gamma\gamma,b\bar{b}}$, $\Delta\phi_{\gamma\gamma,b\bar{b}}$ and $\Delta R_{\gamma\gamma,b\bar{b}}$	Distance in rapidity, azimuthal angle and ΔR between the diphoton and the b-tagged jets system.
Missing transverse momentum variables	
$E_{\mathrm{T}}^{\text{miss}}$	Missing transverse momentum.

other event variables is kept but the training is independent of the resonant signal mass hypothesis and can be applied to any resonant mass.

A single BDT is trained with all resonance masses. It has been checked that the performance of the BDT is similar or better than the one obtained by training a specific BDT for each signal mass point. Training all mass points together also reduces the fluctuation point by point in the signal efficiency and expected sensitivity.

Several options have been tested in order to combine the two BDT score outputs. Among all the tested functions, the combination in quadrature in a weighted manner, shown in Equation 5.1, is the most performant one and therefore, the final BDT score

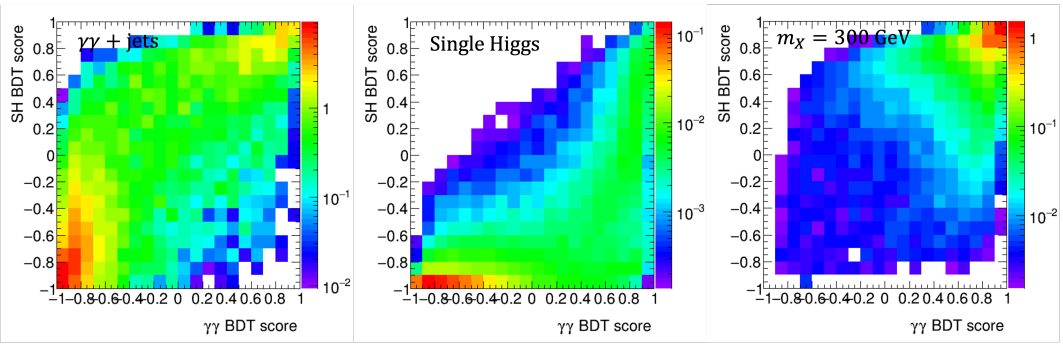

(a) (b) (c)

Figure 5.5: Separation power of both MVAs for the (a) $\gamma\gamma$+jets background, (b) single Higgs background and (c) $m_X = 300$ GeV resonance.

of an event is obtained by Equation 5.1.

$$\mathrm{BDT_{tot}} = \frac{1}{\sqrt{C_1^2 + C_2^2}} \sqrt{C_1^2 \left(\frac{\mathrm{BDT}_{\gamma\gamma} + 1}{2}\right)^2 + C_2^2 \left(\frac{\mathrm{BDT}_{\mathrm{Single}H} + 1}{2}\right)^2}. \tag{5.1}$$

The coefficients C_1 and C_2 ($C_2 = 1 - C_1$) are used to weight the contribution of each MVA and take values in the range [0,1] along with $\mathrm{BDT_{tot}}$. Events considered in this analysis are required to pass a minimum value of the $\mathrm{BDT_{tot}}$. The combination of possible values of C_1 and C_2 and a $\mathrm{BDT_{tot}}$ cut are scanned in order to maximize the binned Asimov significance [152], defined as $\sqrt{\sum_{i=0}^{N_{\mathrm{bins}}} \sigma_{\mathrm{A}}^i}$ where $\sigma_{\mathrm{A}}^i = \sqrt{2((s^i + b^i)ln(1 + s^i/b^i) - s^i)}$ is the Asimov significance in each bin, in the region $120 < m_{\gamma\gamma} < 130$ GeV in a two-stage procedure. First the optimization finds the maximum significance that can be achieved for each resonance mass point independently, this scan leads to different values of the coefficients and the BDT cut as a function of the resonance mass. The second scan is performed to select all coefficients and BDT cut combinations providing a significance within 5% from the maximum possible value. From those all possible combinations, a common C_1 coefficient ($C_1 = 0.65$) is selected across all the resonances so that the selection shares common C_1 and C_2 coefficients for all resonance mass points but different $\mathrm{BDT_{tot}}$ threshold values. Then, for each resonance mass hypothesis, an additional requirement is set on the $m^*_{b\bar{b}\gamma\gamma}$ value to select events within $\pm 2\sigma$ of the expected resonance mass mean value, where σ is the

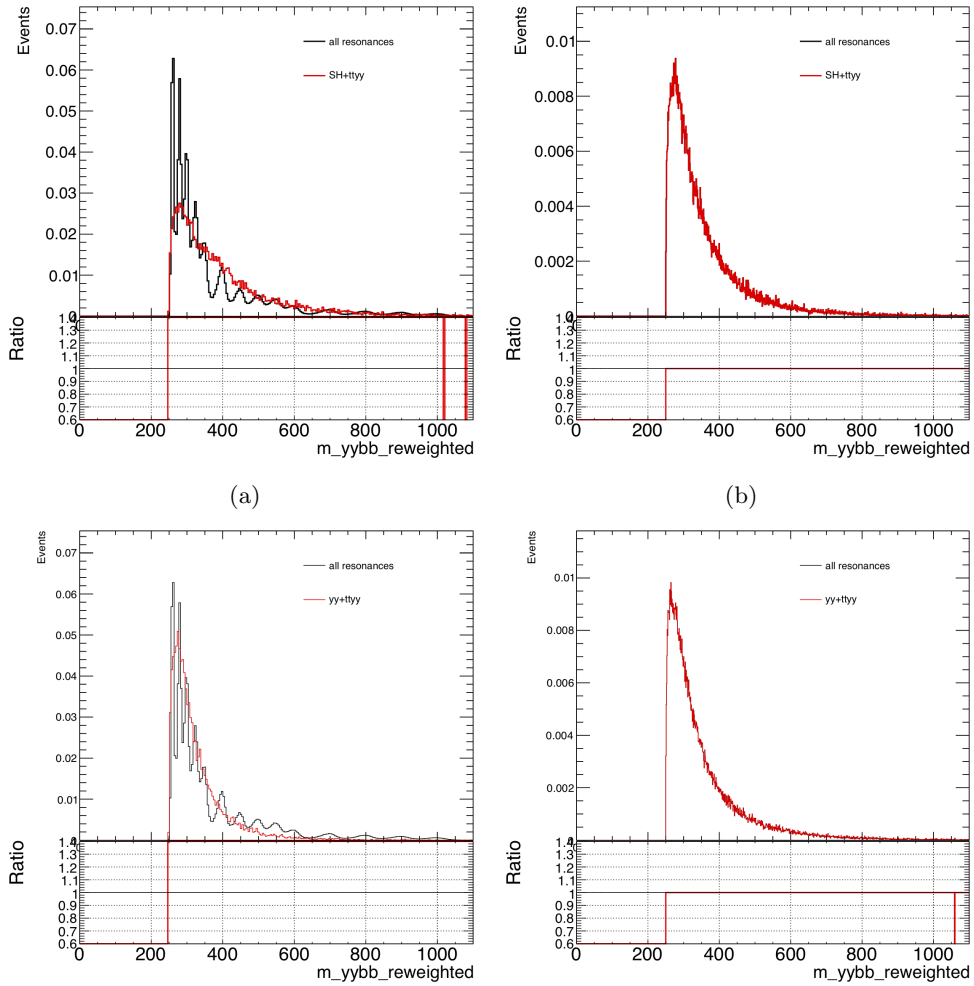

Figure 5.6: Distribution of $m^*_{b\bar{b}\gamma\gamma}$ for (a) all masses hypotheses in black and single Higgs plus $t\bar{t}\gamma\gamma$ background in red before the reweighting procedure and (b) after the reweighting procedure. Distribution of $m^*_{b\bar{b}\gamma\gamma}$ (c) all masses hypotheses in black and $\gamma\gamma$ plus $t\bar{t}\gamma\gamma$ background in red before the reweighting procedure and (d) after the reweighting procedure.

standard deviation obtained from a fit of the $m^*_{b\bar{b}\gamma\gamma}$ distribution using a Crystal Ball function. For the 900 GeV and 1000 GeV mass hypotheses the requirement is relaxed to $\pm 4\sigma$ in order to increase the number of expected background events in the $m_{\gamma\gamma}$ sideband regions, defined as the region 105 GeV $< m_{\gamma\gamma} <$ 120 GeV$\cup$130 GeV $< m_{\gamma\gamma} <$ 160 GeV. The result of these fits are shown in Appendix A. Finally, Figure 5.7 shows the $\mathrm{BDT_{tot}}$ distribution for two resonance mass hypotheses (300 GeV and 500 GeV) used as benchmark. $\mathrm{BDT_{tot}}$ distributions for all mass point hypotheses can be seen in Appendix A.

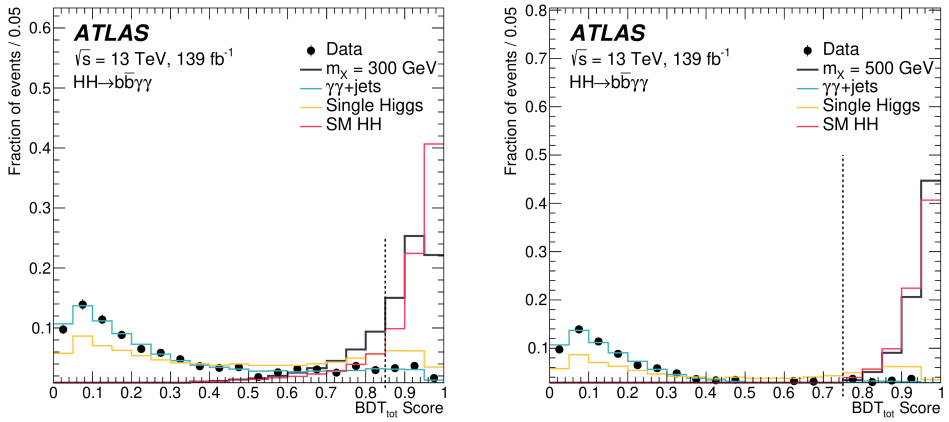

(a) $m_X = 300$ GeV. (b) $m_X = 500$ GeV.

Figure 5.7: The $\mathrm{BDT_{tot}}$ score for the benchmark signals (a) $m_X = 300$ GeV and (b) $m_X = 500$ GeV and for the main backgrounds. Distributions are normalized to unit area. The dotted lines denote the event selection thresholds. Events with a $\mathrm{BDT_{tot}}$ score below 0.85 for $m_X = 300$ GeV or below 0.75 for $m_X = 500$ GeV are discarded [151].

Non-resonant selection

For the non-resonant selection the events are divided in two regions based on the value of $m^*_{b\bar{b}\gamma\gamma}$. A high mass region is defined by requiring $m^*_{b\bar{b}\gamma\gamma} > 350$ GeV, targeting the SM signal ($\kappa_\lambda = 1$), and a low mass region is defined as $m^*_{b\bar{b}\gamma\gamma} < 350$ GeV, targeting BSM processes ($|\kappa_\lambda| \neq 1$). Figure 5.8 shows the distribution of events of these two regions for the ggF and the VBF HH production modes.

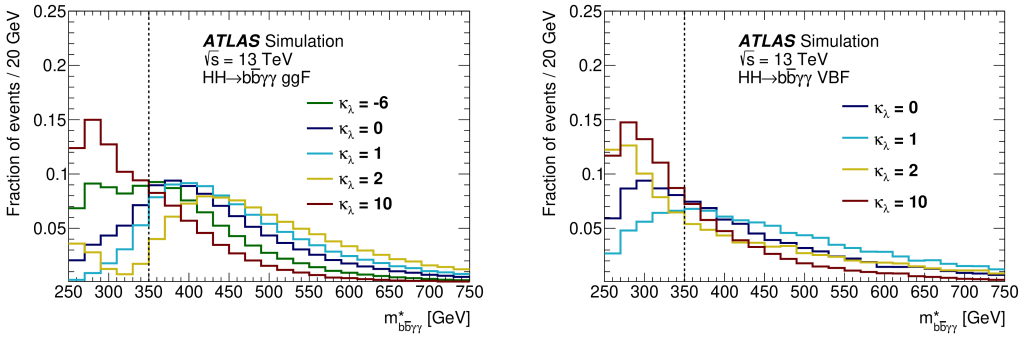

(a) ggF HH production mode. (b) VBF HH production mode.

Figure 5.8: The $m^*_{b\bar{b}\gamma\gamma}$ distributions after the common preselection for (a) non-resonant ggF HH and (b) VBF HH signals with several κ_λ values. The value of $m_{\gamma\gamma bb^*} = 350$ GeV is chosen as the boundary between categories targeting the SM and BSM signals [151].

For this analysis a BDT is trained using XGBoost [153] in each mass region in order to discriminate between a selected HH signal ($\kappa_\lambda = 1\text{and}10$) and the main backgrounds $\gamma\gamma$, $t\bar{t}H$, ggH and ZH. For the high mass region the BDT is trained with the SM HH sample ($\kappa_\lambda = 1$) as signal while the $\kappa_\lambda = 10$ sample is used for the low mass region. The input variables used for the training can be seen in Table 5.3.

Table 5.3: Variables used in the BDT for the non-resonant analysis. All vectors in the event are rotated so that the leading photon ϕ is equal to zero.

Variable	Definition
Photon-related kinematic variables	
$p_{\mathrm{T}}/m_{\gamma\gamma}$	Transverse momentum of each of the two photons divided by the diphoton invariant mass $m_{\gamma\gamma}$.
η and ϕ	Pseudorapidity and azimuthal angle of the leading and subleading photon.
Jet-related kinematic variables	
b-tag status	Highest fixed b-tag working point (60%, 70%, or 77%) that the jet passes.
p_{T}, η and ϕ	Transverse momentum, pseudorapidity and azimuthal angle of the two jets with the highest b-tagging score.
$p_{\mathrm{T}^{b\bar{b}}}$, $\eta_{b\bar{b}}$ and $\phi_{b\bar{b}}$	Transverse momentum, pseudorapidity and azimuthal angle of the b-tagged jets system.
$m_{b\bar{b}}$	Invariant mass of the two jets with the highest b-tagging score.
H_{T}	Scalar sum of the p_{T} of the jets in the event.
Single topness	For the definition, see Eq. (5.2).
Missing transverse momentum variables	
$E_{\mathrm{T}}^{\mathrm{miss}}$ and ϕ^{miss}	Missing transverse momentum and its azimuthal angle.

The BDT input variables are exploiting the different kinematic properties of signal and background events, as well as the b-tagging information. Observables based on the kinematic properties of the reconstructed photons (i.e. leading and sub-leading photon angular distributions), the transverse momentum divided by the di-photon invariant mass along with jet-based information. The "single topness" (χ_{Wt}) is used and defined

as:

$$\chi_{Wt} = \min \sqrt{\left(\frac{m_{j_1 j_2} - m_W}{m_W}\right)^2 + \left(\frac{m_{j_1 j_2 j_3} - m_t}{m_t}\right)^2}, \tag{5.2}$$

where the minimum is taken over all combination of three jets in the event (without b-tagging constraints), and $m_W = 80$ GeV and $m_t = 173$ GeV. The highest discriminant power against $\gamma\gamma$+jets continuum background is provided by $m_{b\bar{b}}$ and H_{T} variables. The distribution of the BDT score of the low mass and high mass regions can be seen in Figure 5.9 for events passing the common pre-selection.

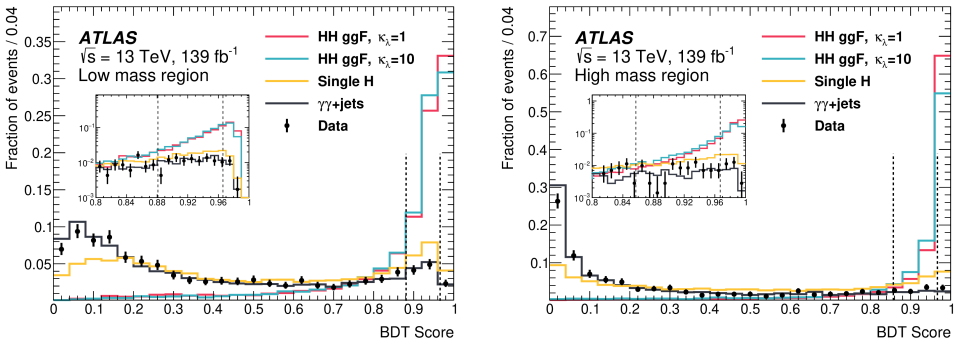

(a) Low mass region.

(b) High mass region.

Figure 5.9: The BDT distribution of the di-Higgs ggF signal for two different values of κ_λ and the main backgrounds in the (a) low mass region and (b) high mass region. Distributions are normalized to unit area. The dotted lines denote the category boundaries. Events with a BDT score below 0.881 in the low mass region or below 0.857 in the high mass region are discarded [151].

For each mass region, two categories are defined based on the BDT score. These categories are chosen by maximizing the combined significance using the signal and background yields in the $120 < m_{\gamma\gamma} < 130$ GeV mass window. The categories obtained by this definition can be seen in Table 5.4.

Data and predictions comparison

The analysis requires two tight photons and this requirement selects mainly $\gamma\gamma$+jets events and events where one or two of the jets are mis-identified as photons. The fraction of each component is estimated using data-driven techniques [154] exploiting the photon identification and isolation distributions from genuine and mis-identified

Table 5.4: Definition of the categories used in the HH non-resonant search. Before entering the BDT-based categories, events are required to satisfy the common preselection.

Category	Selection criteria
High mass BDT tight	$m^*_{b\bar{b}\gamma\gamma} \geq 350$ GeV, BDT score $\in [0.967, 1]$
High mass BDT loose	$m^*_{b\bar{b}\gamma\gamma} \geq 350$ GeV, BDT score $\in [0.857, 0.967]$
Low mass BDT tight	$m^*_{b\bar{b}\gamma\gamma} < 350$ GeV, BDT score $\in [0.966, 1]$
Low mass BDT loose	$m^*_{b\bar{b}\gamma\gamma} < 350$ GeV, BDT score $\in [0.881, 0.966]$

photons. The outcome of the study is that $(85 \pm 3)\%$ of sideband events are di-photon events and the remaining $(15 \pm 4)\%$ consists of γ-jet events and of a negligible amount of di-jet events. The uncertainties on the previous fractions consider both statistical and systematic uncertainties, where the systematic uncertainty is estimated using different photon identification criteria. This study is only used to understand the composition of the background template that is affecting the analysis and therefore is not used directly in the signal extraction. The final background estimation is obtained using data-driven techniques from the fit of data events.

The agreement between data and the background prediction for the $m_{\gamma\gamma}$ and $m^*_{b\bar{b}\gamma\gamma}$ distributions can be seen in Figure 5.10 at pre-selection level. The continuum background is scaled based on the $\gamma\gamma$, γ-jet and di-jet fractions normalized to the data sideband. The $\gamma\gamma$+jets contribution is also divided based on the flavour of the two jets. The jets decomposition is directly taken from the proportion predicted by the SHERPA event generator.

The $m_{\gamma\gamma}$ distribution with the contribution of different processes along with the data and prediction agreement after the selection can be seen in Figures 5.11 and 5.12, two benchmark points $m_X = 300$ GeV and $m_X = 500$ GeV are shown.

5.4 Signal and background parametrization

The signal and backgrounds are extracted by fitting analytic functions to the di-photon invariant mass distribution in the range $105 < m_{\gamma\gamma} < 160$ GeV in both the resonant and non-resonant HH searches.

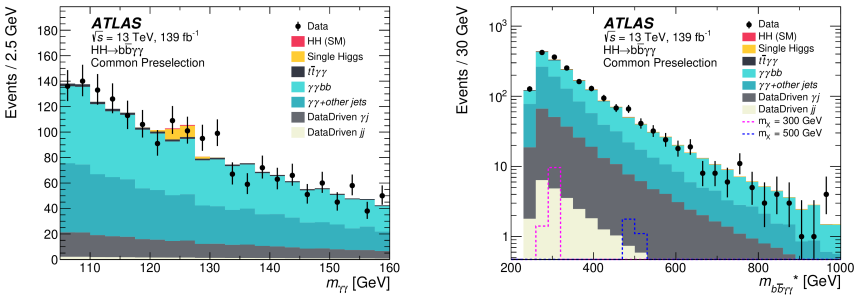

(a) (b)

Figure 5.10: Distributions of (a) $m_{\gamma\gamma}$ and (b) $m_{\gamma\gamma bb^*}$ for events satisfying the common preselection criteria. The data-derived fractions of non-resonant $\gamma\gamma$, γ–jet or jet–γ, and di-jets backgrounds are applied and the total background is normalized to the data sideband. The scalar resonance signal is scaled to a total production cross section $\sigma(pp \to X \to HH) = 370$ fb for $m_X = 300$ GeV and $\sigma(pp \to X \to HH) = 67$ fb for $m_X = 500$ GeV, these values correspond to the exclusion values determined in Section 5.6 [151].

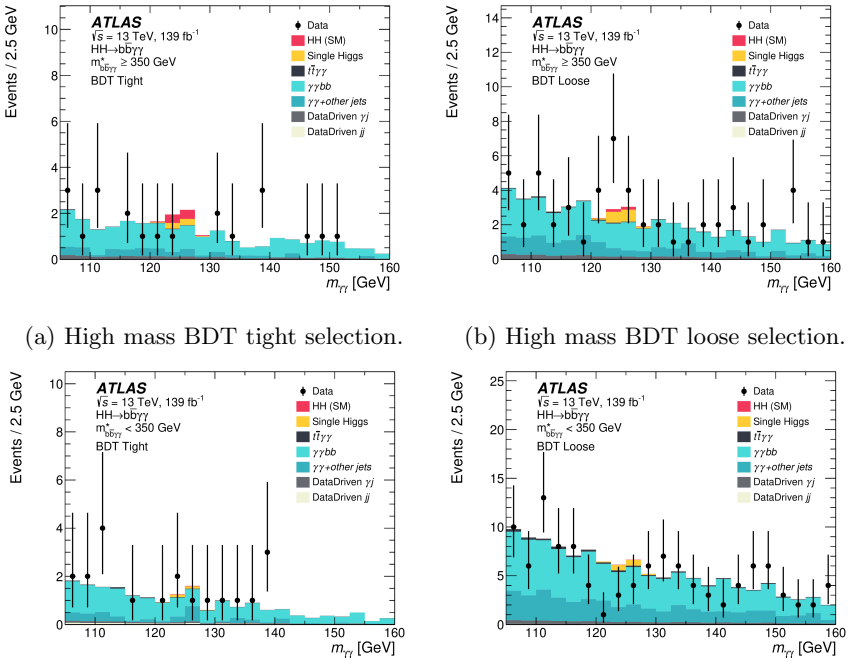

(a) High mass BDT tight selection. (b) High mass BDT loose selection.

(c) Low mass BDT tight selection. (d) Low mass BDT loose selection.

Figure 5.11: Distributions of $m_{\gamma\gamma}$ in all signal categories for the non-resonant HH search: (a) high mass BDT tight, (b) high mass BDT loose, (c) low mass BDT tight, (d) low mass BDT loose. The data-derived fractions of non-resonant $\gamma\gamma$, γ–jet or jet–γ, and di-jets backgrounds are applied and the total background is normalized to the data sideband [151].

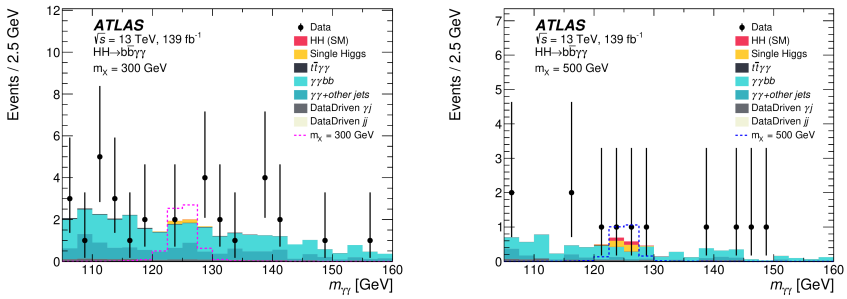

(a) (b)

Figure 5.12: Distributions of $m_{\gamma\gamma}$ for the selections used for the resonance mass points (a) $m_X = 300$ GeV and (b) $m_X = 500$ GeV for the resonant search. The data-derived fractions of non-resonant $\gamma\gamma$, γ–jet or jet–γ, and di-jets backgrounds are applied and the total background is normalized to the data sideband. The scalar resonance signal is scaled to a total production cross section $\sigma(pp \to X \to HH) = 370$ fb for $m_X = 300$ GeV or $\sigma(pp \to X \to HH) = 67$ fb for $m_X = 500$ GeV these values correspond to the exclusion values determined in Section 5.6 [151].

Signal parametrization

The di-Higgs signal and the single Higgs boson background parametrized forms are determined by fitting the $m_{\gamma\gamma}$ distribution of simulated events and normalized considering the acceptance times efficiency obtained from the simulation. The di-photon invariant mass distribution for these two processes is modeled with a double-sided Crystal Ball function [155], that is characterized by a Gaussian core and asymmetric power law tails. This shape allows the modeling of situations where the non-Gaussian tails can arise from experimental effects as photon energy mis-measurements.

The shape parameters are determined by fitting the di-photon invariant mass distribution in simulation for each category. The width of the fitted function is found to be largely insensitive to the specific signal process considered in the analysis with a maximum variance of about 10%.

For the non-resonant search, the parametrized form of $m_{\gamma\gamma}$ is obtained from the simulation samples of ggF and VBF HH processes with $\kappa_\lambda = 1$. There is no significant dependence of the functional form with κ_λ. In the case of the resonant analysis the functional form is obtained from the simulation of each resonance mass hypothesis. Table 5.5 shows the effective resolution (the smallest mass window that contains 68% of the signal events) of the functional form fit to the $m_{\gamma\gamma}$ distribution for simulated Higgs boson pair events for the non-resonant categories and for two different mass hypothesis

for a heavy resonance. For resonant and non-resonant searches, it is found that the chosen functional form models both the single Higgs and di-Higgs boson events well. Since no statistically significant bias is observed in injection tests between the input and fitted signals, the same parameterized function is used.

Table 5.5: The resolution parameter of the double-sided Crystal Ball functional form and the corresponding statistical uncertainty are obtained from the fit to the $m_{\gamma\gamma}$ distribution for simulated Higgs boson pair events for the non-resonant categories and for two different mass hypotheses for a heavy-resonance signal.

Category	σ_{DSCB} [GeV]
High mass BDT tight	1.33 ± 0.01
High mass BDT loose	1.47 ± 0.02
Low mass BDT tight	1.50 ± 0.06
Low mass BDT loose	1.64 ± 0.03
Resonant $m_X = 300$ GeV	1.78 ± 0.02
Resonant $m_X = 500$ GeV	1.46 ± 0.01

Background parametrization

The continuum di-photon background is modeled using a functional form that is selected fitting the MC background template. The background template is built from the $\gamma\gamma$+jets distribution normalized to the data sidebands that are defined in the mass windows 105-120 GeV and 130-160 GeV in the $m_{\gamma\gamma}$ distribution. There is no significant effect on the background template by the difference in shape between simulated events and the data sideband events.

A study for each category is performed in order to estimate the potential bias associated with the choice of a specific analytic function to model the continuum background [156] since the signal event yield is extracted from a signal-plus-background fit to the background-only di-photon invariant mass distribution in the range $105 < m_{\gamma\gamma} < 160$ GeV. This bias is commonly named "spurious signal". The number of spurious signal events is obtained by fitting signal events for Higgs boson masses varying in intervals of 1 GeV from 121 GeV to 129 GeV. The spurious signal yield is taken as the largest number of fitted signal events in this 8 GeV mass window. From all analytical functions that are tested, the one with the smallest number of parameter is chosen among all the

functions with a spurious signal smaller than 20% of the data statistical uncertainty plus two times of the MC statistical uncertainty following Equation 5.3.

$$\zeta_{sp} = \begin{cases} N_{sp} + 2\Delta_{MC}, & N_{sp} + 2\Delta_{MC} < 0 \\ N_{sp} - 2\Delta_{MC}, & N_{sp} - 2\Delta_{MC} > 0 \\ 0, & \text{otherwise} \end{cases} \tag{5.3}$$

An example of the "spurious signal" test is shown in Table 5.6 for a selection of analytical functions. This test is performed for all categories of both searches.

func. form $m_{\gamma\gamma}$	n_{par}	n_{sp}	Δn_{sp}	n_{HH}^{SM}	Pass 10 % exp. signal	χ^2/ndf (MC-like stat.)	p	χ^2/ndf (data-like stat.)	p	σ_{bkg}^{exp}	Z_{spur}	Pass 20 % exp. bkg err	Pass OR condition
Bernstein2	2	0.472	0.358	0.050	Pass	1.82 (78.36/43)	0.00	0.05 (2.16/43)	1.00	1.708	0.276	Pass	Pass
Novosibirsk	3	0.475	0.465	0.050	Pass	1.92 (80.63/42)	0.00	0.05 (2.17/42)	1.00	1.800	0.264	Pass	Pass
ExpPol2	2	0.486	0.369	0.050	Pass	1.89 (81.35/43)	0.00	0.05 (2.16/43)	1.00	1.848	0.263	Pass	Pass
Bernstein3	3	0.486	0.394	0.050	Pass	1.97 (82.57/42)	0.00	0.05 (2.16/42)	1.00	1.896	0.256	Pass	Pass
ExpPol3	3	0.501	0.383	0.050	Pass	1.92 (80.58/42)	0.00	0.05 (2.20/42)	1.00	1.858	0.270	Pass	Pass
Bernstein4	4	0.535	0.250	0.050	Fail	2.01 (82.34/41)	0.00	0.05 (2.18/41)	1.00	1.829	0.293	Pass	Pass
Exp	1	0.606	0.352	0.050	Pass	1.70 (74.87/44)	0.00	0.05 (2.05/44)	1.00	1.593	0.380	Pass	Pass
Pow	1	0.680	0.353	0.050	Pass	1.71 (75.18/44)	0.00	0.05 (2.05/44)	1.00	1.567	0.434	Pass	Pass

Table 5.6: Wald tests results for simulated signal events $\kappa_\lambda = 1$ in the non-resonant low mass tight category.

From all the tested functions listed in Table 5.6, it is found that an exponential function $\exp(am_{\gamma\gamma})$ performs the best among all categories, for the resonant and non-resonant searches since it has the minimal amount of degrees of freedom and yields a constantly small bias. Wald tests [157] on data show that there is no a preference for higher degree functional form with respect to the exponential function.

5.5 Systematic uncertainties

The biggest limitation of this analysis is the statistical precision. The uncertainty in the integrated luminosity of the full Run 2 data set is 1.7% [128] that is obtained using the LUCID-2 detector for the primary luminosity measurements.

The main background process, $\gamma\gamma$+jets, is determined from data-driven techniques and therefore is subject to potential biases from the background model. The background functional form bias is assessed as an additional uncertainty in the total number of signal events in each category. The uncertainties on the rest of the background and signal processes, single Higgs and di-Higgs boson production processes, are estimated using

simulation, and experimental and theoretical systematic uncertainties are considered through the full analysis procedure.

The efficiency of the di-photon trigger used to select events is evaluated in simulation using a trigger matching technique and in data using a bootstrap method [147]. The trigger efficiency uncertainty affects the acceptance by 1% in each category in the di-photon invariant mass region $105 < m_{\gamma\gamma} < 160$ GeV. $Z \to e^+e^-$ events comparison between data and simulation is used to assess the uncertainty in the vertex selection efficiency by comparing the efficiency of finding photon-pointing vertices [158]. The result from this study is found to have a negligible effect on the signal selection efficiency.

The systematic uncertainties due to the photon identification and isolation efficiencies are evaluated by varying the correction factors of photon selection efficiencies in simulation by the corresponding uncertainties and affect the di-photon selection efficiency [99]. The experimental uncertainties in photon scale and resolution are obtained from Ref. [99].

The observable $m_{b\bar{b}}$ is affected by the jet energy scale and resolution uncertainties, while flavour-tagging uncertainties affect the acceptance of the analysis categories. The experimental uncertainties in energy scale and resolution are propagated to the $E_{\mathrm{T}}^{\mathrm{miss}}$ calculation. The flavour tagging uncertainty for b- and c-jets is estimated using $t\bar{t}$ events, while the mis-identification uncertainty of light-flavour jets is determined using di-jets events [159]. Additional uncertainties related to the b-jet momentum correction related to the presence of muons and neutrinos are negligible.

For the single Higgs and SM HH production, the effects of theoretical scale uncertainties due to missing higher-order corrections on the production rates are estimated by varying the factorization and renormalization scales up and down from their nominal values by a factor two, then recalculating the cross section for each variation, and taking the largest deviation from the nominal cross section as the uncertainty. The uncertainties in the cross section and PDF+α_s, and the uncertainties on the $H \to \gamma\gamma$ and $H \to b\bar{b}$ branching ratios are taken from [121]. A 100% uncertainty is considered for the single Higgs boson ggF and VBF production modes and for the WH associated production. There is no additional heavy-flavour uncertainty assigned to single Higgs boson $t\bar{t}H$ and ZH production modes, which are modes where the dominant heavy-flavour pro-

duction is already accounted for at LO. For the non-resonant HH production process a systematic uncertainty is assigned to the κ_λ reweighting.

For the resonant search, uncertainties coming from theoretical scale uncertainties are neglected for the signal. The SM HH production process is added as part of the background. For all possible resonances, uncertainties related to the PDF choice and differences between alternative models of parton showering and hadronization are considered.

The summary of the dominant systematic uncertainties can be seen in Table 5.7 for both resonant and non-resonant searches.

Table 5.7: Breakdown of the dominant systematic uncertainties. The impact of the uncertainties is defined according to the statistical analysis. It corresponds to the relative variation of the expected upper limit on the cross section when re-evaluating the profile likelihood ratio after fixing the nuisance parameter in question to its best-fit value, while all remaining nuisance parameters remain free to float. The impact is shown in %. Only systematic uncertainties with an impact of at least 0.2% are shown. Uncertainties of the "Norm. + Shape" type affect both the normalization and the parameters of the functional form. The rest of the uncertainties affect only the yields.

		Relative impact of the systematic uncertainties [%]	
Source	Type	Nonresonant analysis HH	Resonant analysis $m_X = 300$ GeV
Experimental			
Photon energy resolution	Norm. + Shape	0.4	0.6
Jet energy scale and resolution	Normalization	< 0.2	0.3
flavour tagging	Normalization	< 0.2	0.2
Theoretical			
Factorization and renormalization scale	Normalization	0.3	< 0.2
Parton showering model	Norm. + Shape	0.6	2.6
Heavy-flavour content	Normalization	0.3	< 0.2
$\mathcal{B}(H \to \gamma\gamma, b\bar{b})$	Normalization	0.2	< 0.2
Spurious signal	Normalization	3.0	3.3

5.6 Results

5.6.1 Statistical framework

For the resonant and non-resonant searches the results are extracted from a maximum likelihood fit to the $m_{\gamma\gamma}$ distribution in the $105 < m_{\gamma\gamma} < 160$ GeV window performed

simultaneously over all the categories. The likelihood function is defined in Eq. (5.4):

$$\mathcal{L} = \prod_{c} \left(\text{Pois}(n_c | N_c(\boldsymbol{\theta})) \cdot \prod_{i=1}^{n_c} f_c(m^i_{\gamma\gamma}, \boldsymbol{\theta}) \cdot G(\boldsymbol{\theta}) \right), \tag{5.4}$$

where for each event i in a category c, n_c is the observed number of events, N_c is the expected number of events, f_c is the value of the probability density function (pdf), $\boldsymbol{\theta}$ are nuisance parameters, and $G(\boldsymbol{\theta})$ are constraint pdfs for the nuisance parameters.

The sum of expected yields from di-Higgs boson production processes, single Higgs boson, the non-resonant background and the spurious signal uncertainty is denoted by N_c and defined in Eq. (5.5):

$$N_c(\boldsymbol{\theta}) = \mu \cdot N_{HH,\text{c}}(\boldsymbol{\theta}^{\text{yield}}_{HH}) + N^{\text{res}}_{\text{bkg,c}}(\boldsymbol{\theta}^{\text{yield}}_{\text{res}}) + N_{\text{SS,c}} \cdot \boldsymbol{\theta}^{\text{SS,c}} + N^{\text{nonres}}_{\text{bkg,c}}, \tag{5.5}$$

where μ is the signal strength, defined as the measured signal event yields divided by the signal prediction, $\boldsymbol{\theta}^{\text{SS,c}}$ represent the nuisance parameters associated with the background function bias and $\boldsymbol{\theta}^{\text{yield}}$ represent the nuisance parameters affecting the event yield. The correlation of the nuisance parameters between different signal and background processes, as well as between categories, is also considered. For the resonant searches it is denoted by $N^{\text{res}}_{\text{bkg,c}} = N_{H,\text{c}} + N_{\text{SM}HH,\text{c}}$ and for the non-resonant search $N^{\text{non-res}}_{\text{bkg,c}} = N_{H,\text{c}}$.

The probability density function f_c represents the shape information. For this analysis, the sum of the double-sided Crystal Ball function is used for the modeling of the HH production processes, single Higgs boson, and the spurious signal, and for the analytical function modeling the non-resonant background. The sum of all functional forms is shown in Eq. (5.6):

$$\begin{aligned} f_c(m_{\gamma\gamma}, \boldsymbol{\theta}) = [&\mu \cdot N_{HH,\text{c}}(\boldsymbol{\theta}^{\text{yield}}_{HH}) \cdot f_{HH,\text{c}}(m_{\gamma\gamma}, \boldsymbol{\theta}^{\text{shape}}_{HH}) + N^{\text{res}}_{\text{bkg,c}}(\boldsymbol{\theta}^{\text{yield}}_{\text{res}}) \cdot f^{\text{res}}_{\text{bkg,c}}(m_{\gamma\gamma}, \boldsymbol{\theta}^{\text{shape}}_{\text{res}}) \\ &+ N_{\text{SS,c}} \cdot \boldsymbol{\theta}^{\text{SS,c}}_{HH} \cdot f_{HH,\text{c}}(m_{\gamma\gamma}, \boldsymbol{\theta}^{\text{shape}}_{HH}) + N^{\text{nonres}}_{\text{bkg,c}} \cdot f^{\text{nonres}}_{\text{bkg,c}}(m_{\gamma\gamma}, \boldsymbol{\theta}^{\text{shape}}_{\text{nonres}})]/N_c(\boldsymbol{\theta}^{\text{yield}}_{\text{nonres}}), \end{aligned} \tag{5.6}$$

where $\boldsymbol{\theta}^{\text{shape}}$ represent nuisance parameters related to the shape variations of the functional forms. When a nuisance parameter is related to shape and yield variations

at the same time, the two effects are correlated.

The nominal yields of the resonant background processes are extracted from the simulations, while the signal strength, non-resonant background shape parameters and the nuisance parameters are free parameters of the fit. The measurement of the parameters of interest (POIs) are done using a statistical test based on the profile likelihood ratio [160].

In the case that no excess is found, exclusion limits are set on the Higgs boson pair production cross section in the $b\bar{b}\gamma\gamma$ final state. The limits are calculated using the CL_S method [161] with the profile-likelihood-ratio-based test statistics $\tilde{q}_\mu$, defined in Equation 5.7.

$$\tilde{q}_\mu = \begin{cases} -2\ln\frac{\Lambda(\mu,\hat{\hat{\boldsymbol{\theta}}}(\mu))}{\Lambda(0,\hat{\hat{\boldsymbol{\theta}}}(0))} & \hat{\mu} < 0, \\ -2\ln\frac{\Lambda(\mu,\hat{\hat{\boldsymbol{\theta}}}(\mu))}{\Lambda(\hat{\mu},\hat{\hat{\boldsymbol{\theta}}}(\mu))} & 0 \leq \hat{\mu} \leq \mu, \\ 0 & \hat{\mu} > \mu. \end{cases} \tag{5.7}$$

5.6.2 Resonant search results

The fit to the data of the resonant search for two benchmark values of the mass m_X can be seen in Figure 5.13. As it is shown in Table 5.8 for $m_X = 300$ GeV and $m_X = 500$ GeV no significant excess over the SM background expectation is found. Figure 5.14 shows the observed and expected upper limits at 95% CL on the production cross section of a narrow-width scalar resonance. The observed (expected) upper limits vary between 640-44 fb (391-46 fb) in the range $251 \leq m_X \leq 1000$ GeV.

5.6.3 Non-resonant search results

The background fit to the data for each category can be seen in Figure 5.15. No significant excess over the SM background expectation is found, as can be seen in Table 5.9. Since no excess is observed, limits at 95% CL are set based on the profile likelihood ratio approach. The statistical analysis sets a 95% CL upper limit on the non-resonant HH production cross section at 130 fb, while 180 fb is expected. An observed (expected) upper limit at 95% CL on the signal strength of 4.1 (5.5) times the

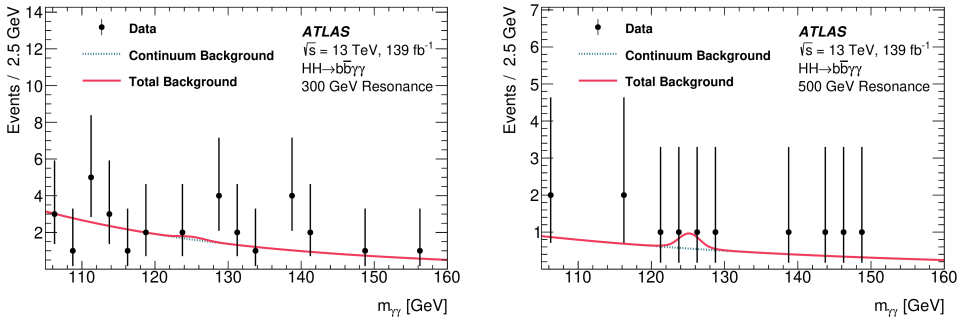

(a) (b)

Figure 5.13: Data are compared with the background-only fit for the resonant search for the (a) $m_X = 300$ GeV and (b) $m_X = 500$ GeV mass hypotheses. The continuum background, as well as the background from single Higgs boson production and from SM HH production, is considered [151].

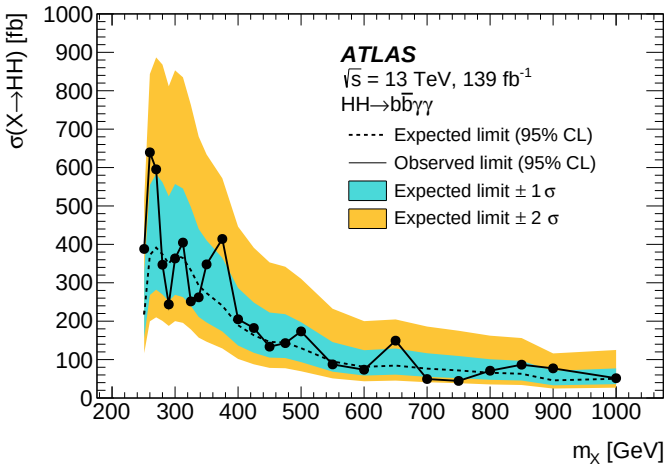

Figure 5.14: Observed and expected limits at 95% CL on the production cross section of a narrow-width scalar resonance X as a function of the mass m_X of the hypothetical scalar particle. The black solid line represents the observed upper limits. The dashed line represents the expected upper limits. The $\pm 1\sigma$ and $\pm 2\sigma$ variations about the expected limit due to statistical and systematic uncertainties are also shown [151].

Table 5.8: The number of events observed in the 120 GeV $< m_{\gamma\gamma} <$ 130 GeV window in data, the number of events expected for scalar resonance signals of masses $m_X = 300$ GeV and $m_X = 500$ GeV assuming a total production cross section $\sigma(pp \to X \to HH)$ equal to the observed exclusion limits of Figure 5.14, and events expected for SM HH and single Higgs boson production (estimated using MC simulation), as well as for continuum background. The values are obtained from a fit of the Asimov data set [160] generated under the signal-plus-background hypothesis. The continuum background component of the Asimov data set is obtained from the fit of the data sideband. The uncertainties in the resonant signals and the SM HH and single-Higgs-boson backgrounds include the systematic uncertainties discussed in Section 5.5. The uncertainty in the continuum background is given by the sum in quadrature of the statistical uncertainty from the fit to the data and the spurious-signal uncertainty.

	$m_X = 300$ GeV	$m_X = 500$ GeV
Continuum background	$5.5^{+1.3}_{-1.5}$	$1.6^{+0.6}_{-0.9}$
Single Higgs boson background	$0.34^{+0.14}_{-0.07}$	$0.40^{+0.18}_{-0.08}$
SM HH background	$0.021^{+0.005}_{-0.009}$	$0.20^{+0.09}_{-0.09}$
$X \to HH$ signal	$6.1^{+0.9}_{-0.8}$	$6.1^{+0.8}_{-0.6}$
Data	6	4

SM prediction is obtained. All theoretical uncertainties are included except the related to the signal cross section, on the other hand, constraints on the signal strength are computed including uncertainties in the predicted signal cross section. The observed (expected) limits on κ_λ are [-1.5,6.7] ([-2.4,7.7]) at 95% as shown in Figure 5.16. The single Higgs boson production cross sections and Higgs boson decay branching ratios are assumed to have SM values for this analysis. The coupling strength between Higgs boson and other particles are set to their SM values. The constraints on κ_λ are extracted over an expected hypothesis excluding $pp \to HH$ production. The VBF HH production mode is considered. It improves the constraints by about a 5% with respect to the alternative fit where only the ggF production mode is considered.

An alternative statistical analysis consists in determining the best-fit value of the k_λ coupling modifier. The best-fit value of k_λ and its uncertainty are obtained by means of a negative log-likelihood scan. The coupling strengths of the Higgs boson to fermions and gauge bosons are set to their SM values. The values of the negative log-likelihood

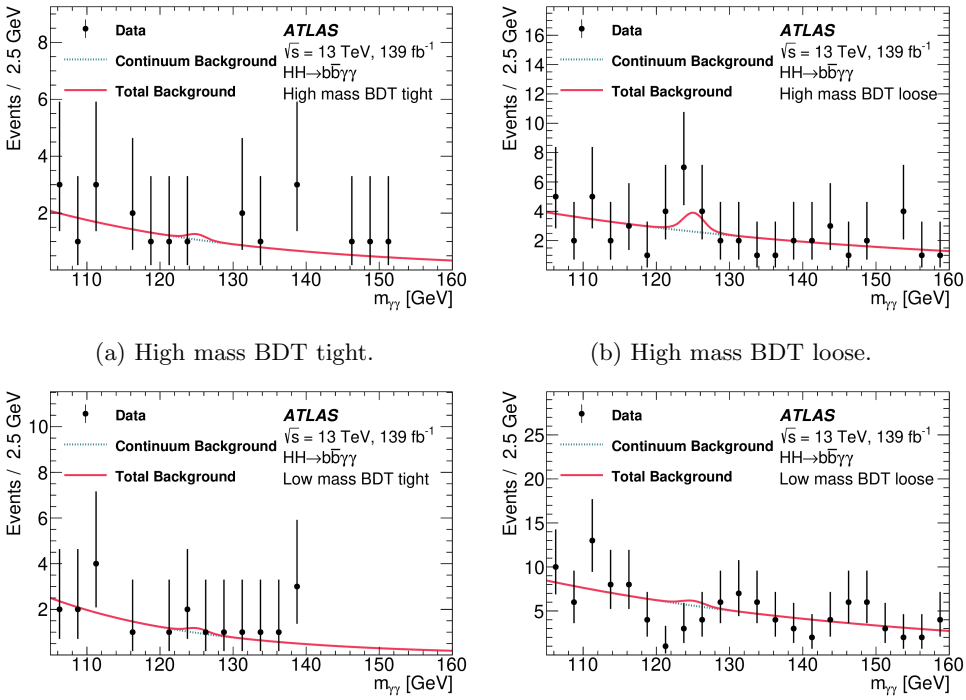

(a) High mass BDT tight.

(b) High mass BDT loose.

(c) Low mass BDT tight.

(d) Low mass BDT loose.

Figure 5.15: Data are compared with the background-only fit for the four categories of the non-resonant search: (a) high mass BDT tight, (b) high mass BDT loose, (c) low mass BDT tight, and (d) low mass BDT loose. Both the continuum background and the background from single Higgs boson production are considered [151].

Table 5.9: The number of data events observed in the $120 < m_{\gamma\gamma} < 130$ GeV window, the number of HH signal events expected for $\kappa_\lambda = 1$ and for $\kappa_\lambda = 10$, and events expected for single Higgs boson production (estimated using MC simulation), as well as for continuum background. For the single Higgs boson, "Rest" includes the following production modes: VBF, WH, $tHqb$, and tHW. The values are obtained from a fit of the Asimov data set [160] generated under the SM signal-plus-background hypothesis, $\kappa_\lambda = 1$. The continuum background component of the Asimov data set is obtained from the fit of the data sideband. The uncertainties in HH signals and single Higgs boson background include the systematic uncertainties discussed in Section 5.5. The uncertainty in the continuum background is given by the sum in quadrature of the statistical uncertainty from the fit to the data and the spurious-signal uncertainty.

	High mass BDT tight	High mass BDT loose	Low mass BDT tight	Low mass BDT loose
Continuum background	$4.9^{+1.1}_{-1.3}$	$9.5^{+1.5}_{-1.7}$	$3.7^{+0.9}_{-1.1}$	$24.9^{+2.3}_{-2.5}$
Single Higgs boson background	$0.67^{+0.29}_{-0.13}$	$1.6^{+0.6}_{-0.2}$	$0.23^{+0.09}_{-0.03}$	$1.40^{+0.33}_{-0.16}$
ggF	$0.26^{+0.28}_{-0.16}$	$0.4^{+0.5}_{-0.2}$	$0.07^{+0.08}_{-0.04}$	$0.27^{+0.27}_{-0.16}$
$t\bar{t}H$	$0.19^{+0.03}_{-0.03}$	$0.49^{+0.09}_{-0.07}$	$0.107^{+0.022}_{-0.017}$	$0.75^{+0.13}_{-0.11}$
ZH	$0.142^{+0.035}_{-0.025}$	$0.48^{+0.09}_{-0.07}$	$0.040^{+0.020}_{-0.014}$	$0.27^{+0.06}_{-0.04}$
Rest	$0.074^{+0.032}_{-0.014}$	$0.16^{+0.07}_{-0.03}$	$0.012^{+0.008}_{-0.004}$	$0.111^{+0.030}_{-0.012}$
SM $HH(\kappa_\lambda = 1)$ signal	$0.87^{+0.10}_{-0.18}$	$0.37^{+0.04}_{-0.07}$	$0.049^{+0.006}_{-0.010}$	$0.078^{+0.008}_{-0.015}$
ggF	$0.86^{+0.10}_{-0.18}$	$0.35^{+0.04}_{-0.07}$	$0.046^{+0.006}_{-0.010}$	$0.072^{+0.008}_{-0.015}$
VBF	$(12.6^{+1.3}_{-1.2}) \cdot 10^{-3}$	$(16.1^{+1.4}_{-1.2}) \cdot 10^{-3}$	$(3.2^{+0.4}_{-0.4}) \cdot 10^{-3}$	$(6.9^{+0.5}_{-0.6}) \cdot 10^{-3}$
Alternative $HH(\kappa_\lambda = 10)$ signal	$6.5^{+1.0}_{-0.8}$	$3.6^{+0.6}_{-0.4}$	$4.5^{+0.7}_{-0.6}$	$8.5^{+1.3}_{-1.0}$
Data	2	17	5	14

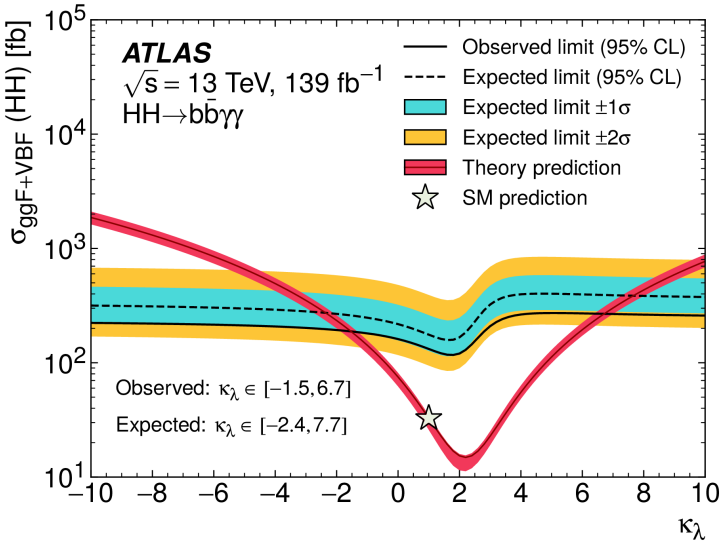

Figure 5.16: Observed and expected limits at 95% CL on the cross section of non-resonant Higgs boson pair production as a function of the Higgs boson self-coupling modifier $\kappa_\lambda = \lambda_{HHH}/\lambda_{HHH}^{\mathrm{SM}}$. The expected constraints on κ_λ are obtained with a background hypothesis excluding $pp \to HH$ production. The $\pm 1\sigma$ and $\pm 2\sigma$ variations about the expected limit due to statistical and systematic uncertainties are also shown. The theory prediction curve represents the scenario where all parameters and couplings are set to their SM values except for κ_λ. The uncertainty band of the theory prediction curve shows the cross-section uncertainty [151].

ratio, $-2\ln\Lambda(\mu)$, as a function of k_λ are shown in Figure 5.17.

The Asimov data set is generated under the SM signal-plus-background hypothesis, $k_\lambda = 1$. All systematic uncertainties, including those of the theoretical prediction of the HH production cross section, are included. The best-fit value corresponds to $k_\lambda = 2.8^{+2.0}_{-2.2}$ $(^{+3.8}_{-4.3})$ for the 1σ (2σ) confidence interval. The expected value corresponds to $k_\lambda = 1.0^{+5.5}_{-2.4}$ $(^{+7.3}_{-4.2})$ for the 1σ (2σ) confidence interval. The second minimum in the expected likelihood scan curve corresponds to a similar fitted signal yield with respect to the k_λ point at the first minimum, which is a consequence of a higher cross section, but lower acceptance and worse signal-to-background separation.

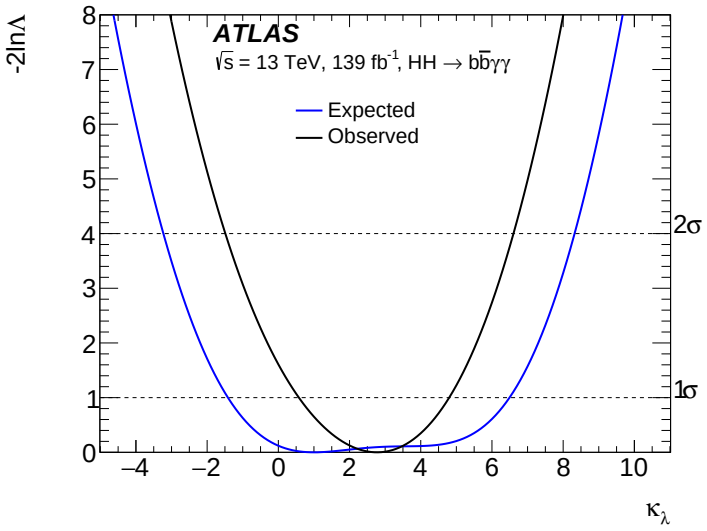

Figure 5.17: Values of the negative log-profile-likelihood ratio ($-2\ln\Lambda$) as a function of k_λ evaluated for the combination of all the categories of the non-resonant search. The coupling of the Higgs boson to fermions and gauge bosons is set to SM values in the profile likelihood calculation. The expected result corresponds to a Asimov data set generated under the SM signal-plus-background hypothesis, $k_\lambda = 1$. All systematic uncertainties, including the theoretical uncertainties in the di-Higgs boson production cross section, are included. The intersections of the solid curves and the horizontal dashed lines indicate the 1σ and 2σ confidence-level intervals.

5.7 Conclusions

Searches for resonant and non-resonant Higgs boson pair production have been performed in the $b\bar{b}\gamma\gamma$ final state using 139 fb^{-1} of 13 TeV pp collision data collected with the ATLAS detector at the LHC. No significant excess above the Standard Model background expectation is observed. For the non-resonant analysis a 95% CL upper limit of 130 fb is set to the $pp \to HH$ non-resonant production cross section, where the expected limit is 180 fb. The observed (expected) limit corresponds to 4.2 (5.7) times the cross section predicted by the Standard Model. Constraints on the Higgs boson self-coupling are also derived and limits of $-1.5 < \kappa_\lambda < 6.7$ are obtained, $-2.4 < \kappa_\lambda < 7.7$ is expected, where a background hypothesis excluding $pp \to HH$ production is considered.

For the production of a scalar particle decaying into a Higgs-boson pair, $X \to HH \to b\bar{b}\gamma\gamma$, the resonant analysis sets upper limits on the production cross section, obtained for the narrow-width hypothesis as a function of m_X. The observed (expected) upper limits are in the range 640-44 fb (391-46 fb) for $251 \leq m_X \leq 1000$ GeV.

Compared to the previous ATLAS result based on 36 fb^{-1} of 13 TeV pp collisions, the present analysis uses a data set more than four times larger, incorporates a categorization based on $m^*_{b\bar{b}\gamma\gamma}$ and multivariate event selections, and expands the analyzed mass range of the resonance search to lower values. The results improve upon the previous ATLAS limits on the $b\bar{b}\gamma\gamma$ production cross section by up to a factor of five, and the allowed κ_λ range shrinks by about a factor of two.

For the resonant search, the expected limit on the cross section improves by a factor of two to three depending on the m_X value. Of those improvements, a factor of two arises from the increase in integrated luminosity, while the additional improvement can be attributed to the use of multivariate techniques, more precise object reconstruction and calibration and, for the non-resonant search, the categorization based on $m^*_{b\bar{b}\gamma\gamma}$. The present analysis also sets constraints that are tighter than those from a combination of ATLAS searches for HH production in up to 36 fb^{-1} of 13 TeV data.

This result is combined with other searches for Higgs boson pair production using 126-139 fb^{-1} of pp collisions data recorder with the ATLAS detector at a $\sqrt{s} = 13$ TeV at the LHC. The $HH \to b\bar{b}\gamma\gamma$ search is combined with searches in the $HH \to b\bar{b}\tau^+\tau^-$ and $HH \to b\bar{b}b\bar{b}$ final states. The non-resonant combination uses the results from the $HH \to b\bar{b}\gamma\gamma$ and $HH \to b\bar{b}\tau^+\tau^-$ searches. No statistically significant excess above the Standard Model expectation has been found, therefore upper limits are set on the production rate of non-resonant Higgs boson pair at the 95% CL. The observed (expected) combined upper limit is found to be 3.1 (3.1) times the SM prediction, as shown in Figure 5.18.

The value of the Higgs boson trilinear self-coupling modifier κ_λ is also excluded outside the observed (expected) range $-1.0 \leq \kappa_\lambda \leq 6.6$ ($-1.2 \leq \kappa_\lambda \leq 7.2$) at 95% CL as shown in Figure 5.19.

For the resonant search combination all three final states are combined, since no statistically significant excess has been found upper limits on the production cross-section of a heavy scalar resonance decaying to two Higgs bosons are set at 95%. The limits are set between 1.1 fb and 595 fb (1.2 fb and 392 fb) in observation (expectation), depending on the resonance mass, m_X, within the studied mass range $251 \leq m_X \leq 3$ TeV as shown in Figure 5.20.

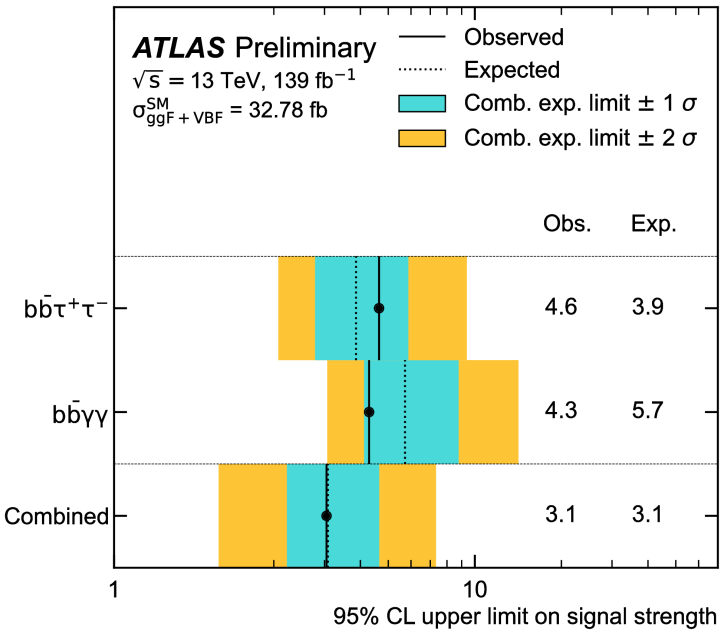

Figure 5.18: Observed and expected 95% confidence level upper limits on the signal strength for SM HH production in the $b\bar{b}\gamma\gamma$ and $b\bar{b}\tau^+\tau^-$ searches, and their statistical combination. The expected limits assume no HH production [162].

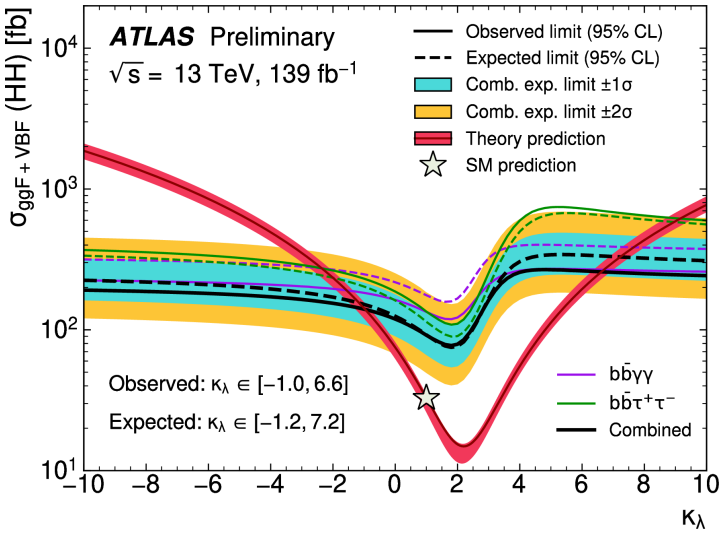

Figure 5.19: Observed and expected 95% confidence level upper limits on the non-resonant HH production cross-section as a function of κ_λ in the $b\bar{b}\gamma\gamma$ and $b\bar{b}\tau^+\tau^-$ searches, and their statistical combination. The expected limits assume no HH production. The theory prediction curve represents the scenario where all parameters and couplings are set to their SM values except for κ_λ [162].

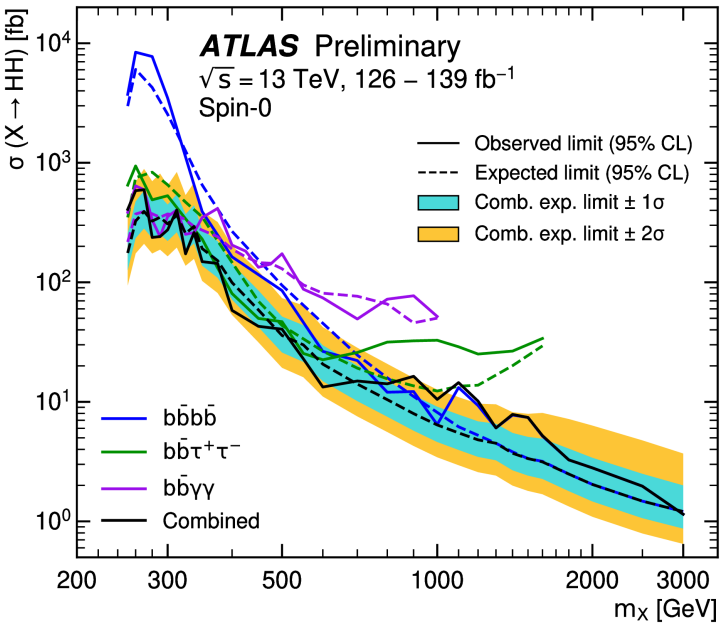

Figure 5.20: Expected and observed 95% confidence level upper limits on $\sigma(X \to HH)$ for a spin-0 resonance as a function of its mass m_X in the $b\bar{b}\gamma\gamma$, $b\bar{b}\tau^+\tau^-$ and $b\bar{b}b\bar{b}$ searches, and their statistical combination. The discontinuities in the limit visible in the range $m_X \leq 400$ GeV are caused by the partial availability of the different analysis limits on a point-by-point basis, which are provided only for the $b\bar{b}\gamma\gamma$ search at the weakest limit points [162].

The non-resonant search result is also compared with the CMS non-resonant search result in the $b\bar{b}\gamma\gamma$ final state [163]. The CMS search uses data from pp collisions at $\sqrt{s} =$ 13 TeV recorded with the CMS detector at the LHC, corresponding to an integrated luminosity of 137 fb^{-1}. No significant deviation from the background-only hypothesis is observed. Therefore, an upper limit at 95% CL is set on the Higgs boson pair production cross section times the Branching Ratio. The observed (expected) upper limit is found to be 0.67 (0.45) fb, which corresponds to 7.7 (5.2) times the Standard Model prediction.

Assuming all other Higgs boson couplings are equal to their values in the Standard Model, the observed coupling modifiers of the trilinear Higgs boson self-coupling κ_λ is constrained to the range $-3.3 \leq \kappa_\lambda \leq 8.5$ at 95% CL level as seen in Figure 5.21.

Studies of projection of non-resonant Higgs boson pair production in the $b\bar{b}\gamma\gamma$ final state with the ATLAS detector are also done [164], assuming 3000 fb^{-1} of pp collisions and a centre of mass energy of $\sqrt{s} = 14$ TeV at the HL-LHC. The projected results are based on extrapolations of the Run 2 analysis with revised assumptions on the systematic. The $b\bar{b}\gamma\gamma$ channel is highly limited by the spurious signal systematic uncertainty

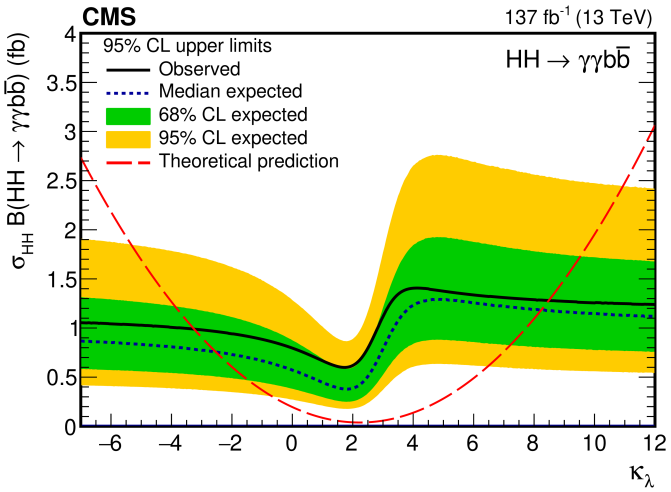

Figure 5.21: Expected and observed 95% CL upper limits on the product of the HH production cross section times $\mathcal{B}(HH \to b\bar{b}\gamma\gamma)$ obtained for different values of κ_λ assuming $\kappa_t = 1$. The green and yellow bands represent, respectively, the one and two standard deviation extensions beyond the expected limit. The long-dashed red line shows the theoretical prediction [162].

associated with the choice of the functional form used for modelling the continuum background. Assuming a spurious signal systematic uncertainty of 0 at the HL-LHC thanks to improved background modelling strategies the projected significance of the SM HH production would be 2.2. The projected 95% CL upper limit on the expected signal strength for SM HH production would be 0.93 while the k_λ allowed interval would be $0.5 \leq \kappa_\lambda \leq 1.6$.

Chapter 6

Conclusions

The discovery of the Higgs boson on July 4^{th} 2012 by the ATLAS and CMS collaborations represented a milestone in the explanation of the electroweak symmetry breaking by which fundamental particles acquire mass. This discovery was just the start of the Higgs boson studies. Precise measurements of its properties investigate the Higgs boson nature, and any deviations from the Standard Model prediction would be a clear sign of new physics.

These measurements need a perfect understanding of the performance of the ATLAS detector. One of the software detector milestone has been achieved for Run 3: moving from a multi-process framework, AthenaMP, to a multi-threading framework, AthenaMT. This new framework will ease the maintenance and make the most effective usage of the emerging computing architectures, allowing a scalable structure capable of processing asynchronous data in a core safe way.

The ATLAS experiment is undergoing upgrades for the HL-LHC phase, during which the LHC will deliver instantaneous luminosities more than 7.5 times the original design value, meaning a more harsh collision environment and higher data transmission rates. In order to maintain the physics performance, the electronics readout of the detector is being upgraded. One of these upgrades is the development of the backend read-out of the Tile Calorimeter interfaced with the TDAQ FELIX system. This is a new readout system integrating the data acquisition and TTC systems with upgraded trigger and detector front-end. The new readout system requires new bytestream converters since

data is now organized in 16 samples of 12 bits for both gains of the Tile Calorimeter. FELIX will be already used during Run 3 by the LAr Calorimeter, the Level-1 Calorimeter trigger system, the new installed NSW and for the rest of detectors, for the HL-LHC.

The Higgs boson pair production is the simplest production process that is sensitive to the self-coupling λ of the Higgs boson. It probes higher-dimension interactions and the possible existence of heavier particles coupling to the Higgs boson. This thesis has presented a search for resonant and non-resonant Higgs boson pair production in the $b\bar{b}\gamma\gamma$ final state with the full Run 2 dataset collected by the ATLAS experiment. No significant deviations from the Standard Model are observed. The observed (expected) upper limit to the $pp \to HH$ non-resonant production cross section is 130 fb (180 fb) which corresponds to 4.2 (5.7) times the cross section predicted by the Standard Model which implies an improvement respect to the ATLAS result based on 36 fb^{-1} of 13 TeV pp collisions of five times. The Higgs boson self-coupling is constrained at 95% CL to $-1.5 < \kappa_\lambda < 6.7$ observed, while $-2.4 < \kappa_\lambda < 7.7$ is expected. For the production of a scalar particle decaying into a Higgs boson pair, $X \to HH \to b\bar{b}\gamma\gamma$, upper limits at 95% CL on the production cross section are set. The observed (expected) upper limits are in the range of 641-49 fb (392-46 fb) for $251 \leq m_X \leq 1000$ GeV. This represents an improvement with respect to the previous result of two to three times depending of the m_X value.

The $HH \to b\bar{b}\gamma\gamma$ is combined with the $HH \to b\bar{b}\tau^+\tau^-$ and $HH \to b\bar{b}b\bar{b}$ searches using 126-139 fb^{-1}. The non-resonant interpretation uses results from the $b\bar{b}\gamma\gamma$ and $b\bar{b}\tau^+\tau^-$ searches, while the resonant interpretation uses results from all three searches. No significant deviation from the Standard Model expectation has been found. Upper limits are set on the non-resonant Higgs boson pair production at 95% CL. The observed (expected) upper limit is found to be 3.1 (3.1) times the Standard Model prediction. The Higgs boson self coupling modifier κ_λ is excluded outside the observed (expected) range $-1.0 < \kappa_\lambda < 6.6$ ($-1.2 < \kappa_\lambda < 7.7$) at 95% CL. Upper limits are also set on the production cross-section of a heavy scalar resonance decaying to two Standard Model Higgs bosons at 95% CL between 1.1 and 595 fb (1.2 and 392 fb) in observation (expectation) varying on the resonance mass, m_X, in the mass range 251 GeV $\leq m_X \leq$

3 TeV.

Chapter 7

Resum en valencià

7.1 Fonaments teòrics

7.1.1 El Model Estàndard

El Model Estàndard de física de partícules és una teoria quàntica de camps que descriu les partícules elementals i les seues interaccions fonamentals, unifica tres de les quatre forces de la natura, les forces electromagnètica, nuclear feble i nuclear forta, en només una.

La matèria es divideix en matèria fermiònica i bariònica. La matèria fermiònica es compon de quarks i leptons d'espí $\frac{1}{2}$ que s'agrupen en tres generacions, cadascuna de les quals està composta per dos elements, un carregat neutre i l'altre eléctricament, formen un doblet. Aquestes famílies són: l'electró (e) anb el neutrí electrònic (ν_e), el muó (μ) i el neutrí muònic (ν_μ), i finalment el tauó (τ) i el neutrí tauònic (ν_τ). Els doblets de quarks reben el nom de *up* i *down* (u, d), *charm* i *strange* (c, s), i *top* i *bottom* (t, b). Els quarks tenen càrrega elèctrica fraccionària, per als quarks de tipus u, c, t és $\frac{2}{3}$ i $-\frac{1}{3}$ per als quarks d, s, b. Els quarks tenen un nombre quàntic addicional, anomenat color, que pot tenir tres valors: roig, verd i blau.

Els colors atorguen la propietat física del confinament, la qual confina als quarks en estats neutres de color, formant hadrons.

Les interaccions entre partícules es produeixen a través de partícules transmissores, anomenades generalment bosons de gauge, les quals tenen la propietat de tenir espí

1. Les interaccions explicades mitjançant el Model Estàndard tenen lloc al grup de simetria $SU(3) \otimes SU(2) \otimes U(1)$. La interacció electromagnètica es transmesa pel fotó (γ), la interacció forta es transmet a través dels gluons (g) i la interacció feble a través dels bosons febles ($W^{\pm}$ i Z^0).

7.1.2 El bosó de Higgs

El descobriment del bosó de Higgs va ser anunciat pels experiments ATLAS i CMS el 4 de juliol de 2012 com una nova partícula amb aproximadament 125 GeV de massa [25, 26]. L'existència del bosó de Higgs va ser una peça fonamental en la compresió del trencament espontani de simetria del Model Estàndard, el qual introdueix un nou camp, anomenat camp de Higgs, el qual al interaccionar amb els bosons $W^{\pm}$ i el Z^0 genera la massa d'aquestes partícules. El bosó de Higgs no té ni càrrega elèctrica ni càrrega de color, de manera que no interactua ni electromagnèticament ni fortament encara que si és capaç d'interaccionar amb si mateix.

Els leptons carregats i els quarks deuen també la seua massa a la interacció amb el camp de Higgs, existint una correlació entre la intensitat de la interacció i la massa de la partícula.

La Figura 7.1 mostra els principals modes de producció del bosó de Higgs en un col·lisionador d'hadrons i es detallen a continuació:

- El principal mode de producció és mitjançant la fusió de gluons (ggH) a l'LHC, representant el 87% de la producció total a una energia en centre de masses de $\sqrt{s} = 13$ TeV.

- La segona contribució més gran es deu a la fusió del bosó de Higgs amb un bosó vectorial (VBF) i és un 6.8% de la producció total. Aquest mode de producció es caracteritza per tenir dos jets a la mateixa direcció transversal.

- El tercer mecanisme de producció és degut a l'associació amb un bosó vectorial (WH, ZH), és un el 4% de la secció eficaç total. Aquest procés se sol denominar com a Higgs-strahlung ja que té característiques similars a la radiació de Bremsstrahlung.

- La producció de bosons de Higgs associats a quarks top ($t\bar{t}H$ i tH) és un dels modes de producció amb la secció eficaç més baixa a l'LHC.

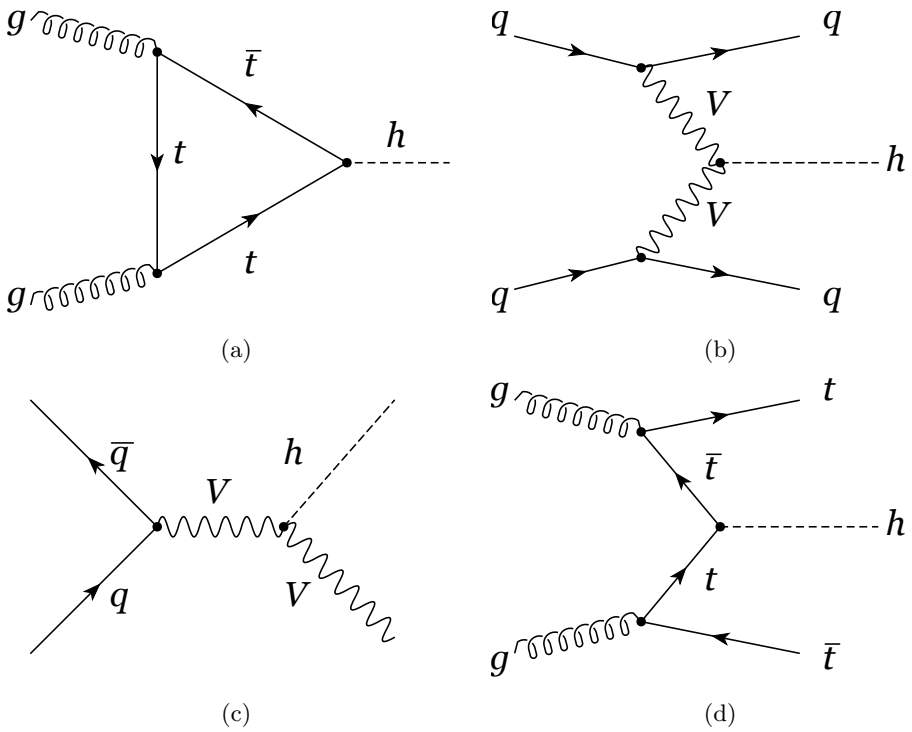

Figure 7.1: Diagrames de Feynman dels modes de producció del bosó de Higgs, mitjançant a) la fusió gluó-gluó a través de llaços de quarks pesats, b) la fusió d'un bosó vectorial (W o Z) amb dos jets, c) la radiació d'un bosó de Higgs (Higgs-Strahlung) a partir d'un bosó V (W o Z) i d) la producció de bosons de Higgs en associació amb quarks top.

El bosó de Higgs és una partícula inestable i per tant es desintegra en parells de partícules i antipartícules. Hi ha diversos canals de desintegració, sent $\gamma\gamma$ i ZZ els dos millors canals per mesurar la massa del bosó de Higgs amb precisió.

La desintegració al canal $\gamma\gamma$ permet mesurar la massa mitjançant l'energia i la direcció dels fotons. El canal ZZ determina la massa a partir de la desintegració dels dos bosons Z en parells d'electrons o muons. Existeixen també altres canals de desintegració com el WW^* el qual es caracteritza per la desintegració en un electró i un neutrí o un muó i un neutrí. Els neutrins escapen sense ser detectats, per la qual cosa, el Higgs es manifesta com un excés en la distribució de massa dels bosons WW^*. El canal de desintegració més probable del bosó de Higgs és a través d'un parell $b\bar{b}$, el qual es caracteritza per ser el canal amb més fons de processos del Model Estàndard.

7.1.3 Producció de parells de bosons de Higgs

La producció de parells de bosons de Higgs (HH) [28] és clau per comprendre el potencial que resulta del mecanisme de ruptura espontània de simetria. La producció de parells de bosons de Higgs és el mecanisme més senzill que és sensible a l'autoacoblament λ. També permet investigar interaccions d'ordre més alt, com l'existència d'estats més pesats que s'acoblen al bosó de Higgs. Hi ha dos mètodes de producció de parells de bosons de Higgs:

- No ressonant: és un mode de producció predit pel Model Estàndard amb una secció eficaç molt petita. Una variació a la secció eficaç, o una desviació al valor esperat de λ_{HHH}, podrien constituir una prova de física més trobada del Model Estàndard.
- Ressonant: moltes de les teories més enllà del Model Estàndard prediuen l'existència de partícules pesades que es desintegren en parells de bosons de Higgs. Aquestes partícules podrien manifestar-se com a ressonàncies a l'espectre de massa del bosó de Higgs.

7.2 L'LHC i l'Experiment ATLAS

7.2.1 L'LHC

El "Large Hadron Collider" (L'LHC) [48] és l'accelerador de partícules mes gran del món amb punts de col·lisió de protons en cadascun dels experiments. L'LHC es troba en un túnel de 27 km de circumferència situat entre la frontera de França i Suïssa, a la ciutat de Ginebra.

L'LHC està dissenyat per a tindre una energia del centre de massa de $\sqrt{s} = 14$ TeV i una lluminositat de $10^{34}\text{cm}^{-2}\text{s}^{-1}$ amb una col·lisió cada 25 ns. Els quatre experiments principals que ho constitueixen són ATLAS [165], CMS [166], LHCb [167] i ALICE [168].

7.2.2 L'Experiment ATLAS

L'experiment ATLAS (A Toroidal LHC Apparatus) és un dels detectors de caràcter general del LHC. Té una longitud de 44 m de llarg i 25 m d'ample, pesant més de 7000

tones. El detector està dividit en diversos sub-detectors que es mostren en la Figura 7.2.

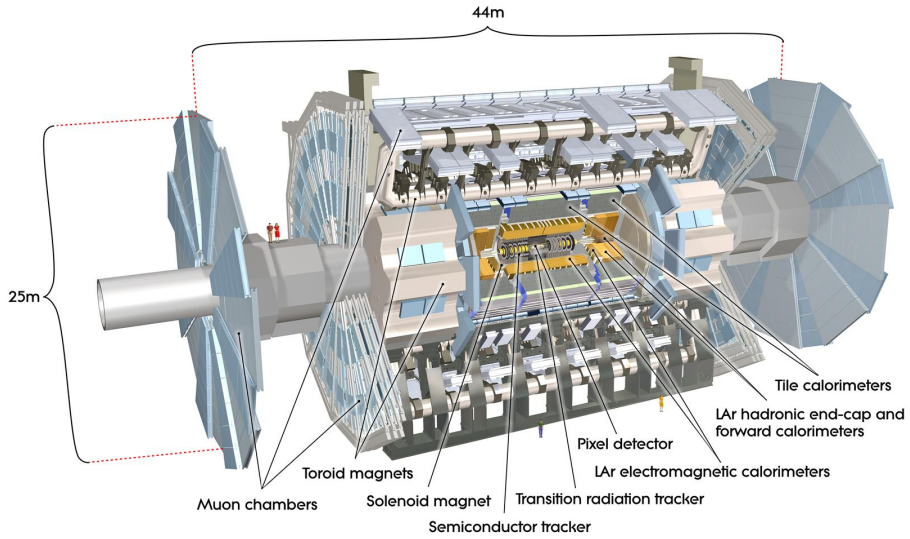

Figure 7.2: Vista en cort del detector ATLAS [53]

.

El sistema de coordenades utilizat per ATLAS es defineix amb l'origen en el punt d'interacció. La direcció z està definida pel feix de protons. La direcció de l'eix x positiva és aquella que apunta cap al centre de l'anell del LHC i l'eix y es defineix com l'ortogonal als eixos anteriors. D'aquesta manera el pla conformat pels eixos $x-y$ és ortogonal a la direcció del feix, i es sol denominar com a pla transversal. Algunes de les quantitats més importants es defineixen com la projecció de magnituds físiques sobre aquest pla, com poden ser el moment transversal p_T o l'energia transversal E_T. L'angle azimutal ϕ es defineix com aquell que envolta a la direcció del feix mentre que l'eix polar θ és aquell que es defineix sobre el feix. En el límit d'una partícula que viatja a la velocitat de la llum, o bé en el límit d'una partícula sense massa, la rapidesa y i la pseudo-rapidesa η estan definides com:

$$y = \frac{1}{2}\ln\left(\frac{E+p_z}{E-p_z}\right) \text{ i } \eta = -\ln\tan\left(\frac{\theta}{2}\right), \tag{7.1}$$

on E és l'energia i p_z és la component del moment al llarg de la direcció del feix. En el límit d'una partícula sense massa $y=\eta$, i totes dues magnituds són invariants sota transformacions de Lorentz en la direcció del feix.

El detector ATLAS va adquirir un conjunt de dades de 5.4 fb^{-1} en el període 2010-2012 a una energia $\sqrt{s} = 7$ TeV i 20.3 fb^{-1} amb $\sqrt{s} = 8$ TeV, que correspon al primer període de presa de dades, conegut com Run 1. El segon període, Run 2, va començar en 2015 amb $\sqrt{s} = 13$ TeV i va acabar en 2018, recollint un total de 139 fb^{-1}.

Els sub-detectors d'ATLAS

El detector ATLAS està constituït pels següents sistemes:

- El sistema d'imants, optimizat per desviar les trajectòries de les partícules carregades elèctricament i minimitzar els efectes de dispersió múltiple. El sistema d'imants està format per un solenoide central per al detector intern, amb un camp axial de 2 T, un toroide de barril i dos toroides externs que generen un camp magnètic tangencial de 0.5 T i 1 T, respectivament.
- Sistema de muons, el qual cobreix el rang de $|\eta| \leq 3$, està format per quatre sub-detectors en funció de la resolució espacial i temporal: MDT, CSC, RPC i TGC.
- El detector intern, el qual està dissenyat per a reconstruir traces i vèrtexs de desintegració. Està format pels sub-detectors: Píxel, SCT i TRT.
- El sistema de calorímetres, el qual mesura la posició i l'energia depositada pels hadrons en el rang $|\eta| \leq 4.9$. La part més interna correspon al calorímetre d'argó líquid (LAr), el qual està format per un cilindre (EM) i dos tapes en els extrems (HEC). Rodejant a LAr es troba TileCal, format per material centellejador.

7.3 Reconstrucció d'esdeveniments

ATLAS identifica electrons, fotons, muons, jets i tauons mitjançant algorismes que converteixen les dades provinents del detector en objectes de física fonamentals.

7.3.1 Fotons i electrons

La interacció d'un fotó o un electró amb el calorímetre electromagètic es troba a l'origen del procés de cascada electromagnètica, en el qual una quantitat d'energia es diposita

en una de les cel·les properes en el calorímetre. La reconsctrucció de fotons i electrons es desenvolupa de la següent manera:

- Reconstrucció de clústers: es reconstrueix en clústers d'energia a partir de les deposicions en les cel·les del calorímetre electromagnètic.
- Reconstrucció de traces: una vegada els clústers han sigut reconstruïts, es realitza un seguiment de les traces en el detector intern que són compatibles amb els clústers, de manera que es poden indentificar i reconstruir els electrons i els fotons convertits en electrons.
- Conversió de traces: les traces compatibles amb partícules provinents d'un procés de conversió de fotons s'utilitzen per a crear candidats als vèrtexs de conversió.
- Concordança entre traces i clústers.
- Cluster final: s'utilitzen algorismes per a decidir si un cluster es correspon a un fotó, a un fotó de conversió o a un electró, basant-se en la informació obtinguda en la resta del procés.

7.3.2 Muons

Els muons es poden identificar i reconstruir utilizant informació del sistema de muons, del detector intern i del calorímetre electromagnètic. Els muons han de satisfer una sèrie de requisits de qualitat, han de tindre un nombre mínim d'impactes en cadascun dels sub-detectors. Es proporcionen quatre seleccions d'identificació de muons, loose, medium, tight i high p_T. Loose, medium i tight són categories inhclusives amb requisits més restrictius.

7.3.3 Jets

Els jets hadronics són els objectes de física que es prodeuixen més abundament a l'LHC. Els jets es reconstrueixen a partir de les cel·les en els calorímetres utilizant l'algorisme anti-k_T amb un paràmetre de distància R = 0.4. Posteriorment se'ls aplica correcions d'energia.

7.3.4 b-jets

El sabor d'un jet es definix per mitjà d'una sèrie de concordances. Primer, es comprova si la reconstrucció coinincideix amb un hadró de tipus bottom, després amb un hadró de tipus charm i finalment amb un tauó. La frequència d'identificació d'hadrones de tipus bottom defineix l'eficiència de l'algorisme d'identificació.

L'experiment ATLAS utilitza diferents algorismes basats en la informació sobre les traces reconstruïdes i els vèrtexs secundaris junt amb la vida mitjana, relativament llarga, dels hadrons tipus bottom. L'algorisme utilitzat en aquesta tesi es denomina DL1r i està optimitzat per a la identificació de b-jets.

7.3.5 $E_{\mathrm{T}}^{\mathrm{miss}}$

Els neutrins produïts en l'LHC no interactuaran amb el detector ATLAS i per tant no es detectaran. Es pot inferir informació indirecta sobre la presència d'aquestes partícles imposant la conservació del moment en el pla transversal a la direcció del feix. Com que l'estat inicial té component de moment nul en el pla transversal, un desequilibri en el moment transversal total mesurat en l'estat final indicaria la presència d'una partícula invisible. Així, l'energia transversal perduda ($E_{\mathrm{T}}^{\mathrm{miss}}$) es defineix com la suma vectorial negativa del moment transversal de tots els objectes seleccionats.

7.4 Millores del Tile Calorimeter

Com a membre de la col·laboració ATLAS, s'han de realitzar una sèrie de contribucions que et qualifiquen com a autor d'ATLAS.

Un element clau de les millores que es realitzen durant el "Long Shutdown 2" és la instal·lació de TileCal Phase-II Demonstrator, el qual té dos canals de comunicació, l'existent ROD i el futur Phase-II FELIX. Per a poder realitzar la reconstrucció de dades en Athena utilitzant aquest nou sistema és necessari el desenvolupament d'una nova funció que descodifique les dades enviades pel sistema nou, així com la modificació d'algorismes de reconstrucció per a funcionar amb el nou format de dades.

A més, el programari de reconstrucció Athena s'està actualitzant per a poder permetre processos multi nuclis.

7.4.1 Migració a AthenaMT

Gaudi [105] i Athena [106] havien estat dissenyats originalment per a la reconstrucció en sèrie d'esdeveniments. Les noves necessitats amb l'augment de lluminositat durant el Run 3, així com les noves tecnologies, han forçat la migració del sistema per funcionar de manera paral·lela en múltiples nuclis de computació [107], AthenaMT.

Ara, els algorismes seran executats basats en una llista de prioritat. Es transmetran les dependències en forma de "ReadHandles" i "WriteHandles". Els algorismes que no tinguen dependències comunes podran ser executats en paral·lel. Un exemple d'un sistema de reconstrucció d'electrons que pot fer-se en paral·lel es mostra en la Figura 7.3.

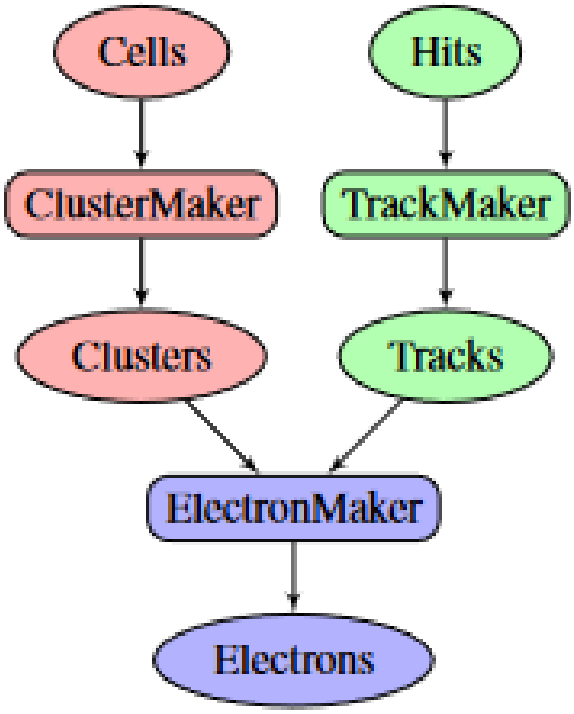

Figure 7.3: Dependència de sistemes per a la reconstrucció d'un electró [109].

Com a part de la meua contribució a la migració de AthenaMT he treballat en el paquet de "Tile Monitoring" adaptant els algorismes "TileTMDBRawChannel i TileTMDBDigitsMonitor" al nou sistema multi-nucli.

TileTMDBRawChannelMonTool

L'algorisme TileTMDBRawChannelMonTool forma part del paquet TileMonitoring. S'encarrega de la reconstrucció de dades RAW provinents del "Tile Muon Digitizer Board", obtenint amplituds de puls de senyal en ADC, així com distribucions de temps, impacte de muons en el TGC i coincidències de muons en el TMDB. La comparació de l'amplitud d puls del pols reconstruïda per tots dos sistemes es mostra en la Figura 7.4.

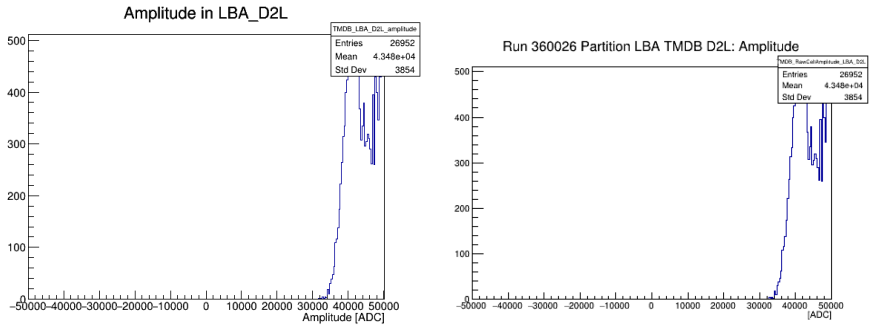

Figure 7.4: Comparació entre (a) l'amplitud reconstruïda pel sistema legacy i (b) pel l'algorisme migrat al nou sistema.

TileTMDBDigitsMonitorAlgorithm

L'algorisme TileTMDBDigitsMonitorAlgorithm s'encarrega del monitoratge del soroll digital, obtenint histogrames del valor del pedestal, el soroll d'alta freqüència i la energia de cada partició i cel·la del detector.

7.4.2 Millora per al HL-LHC

Per al període de "High Luminosity LHC" (a partir de 2028) s'està duent a terme la instal·lació de nous sistemes de triggers així com d'adquisició de dades.

Sistema FELIX

El sistema FELIX és un nou component que actua d'interfície entre el sistema d'adquisició de dades, el control del detector i el sistema TTC així com entre el nou trigger i la nova electrònica de lectura de dades.

La migració a aquest nou sistema implica també la instal·lació de nova electrònica

en el detector, el Tile PreProcessor, el qual està dissenyat per a substituir a l'actual ROD.

Actualment, el TileCal Phase-II Demonstrator té dos sistemes, la nova electrònica TilePPr i l'antic ROD, la qual cosa permet poder reconstruir les dades amb tots dos sistemes i comparar-los.

Per a poder comparar tots dos sistemes, un nou descodificador ha sigut desenvolupat per a la nova estructura de dades, així com el nou format degut al TilePPr. La Taula 7.1 mostra les diferències en el format de les dades entre la nova electrònica i el sistema antic.

	Legacy	FELIX
Mostres	7	16
Amplitud en bits	10	12
Guany	1-2	2

Table 7.1: Diferències del format de dades entre TilePPr i Legacy.

La comparació es realitza mitjançant dos algorismes de reconstrucció "Optimal Filtering" i "Fit Method".

Fit Method

Aquest mètode serveix per a comparar les amplituds d'energia en ADC de tots dos sistemes, permetent la reconstrucció de dues diferents formes:

- Els 16 12-bits de les mostres de FELIX amb l'antic sistema.
- Els 7 12-bits de les mostres intermèdies de FELIX amb l'antic sistema.

Les diferències que es troben estan dins dels valors esperats existint nous efectes a causa de l'augment del nombre de mostres.

Optimizal Filtering

Aquest és un altre mètode de reconstrucció d'amplitud d'energia en ADC, en aquest cas ajusta el valor màxim de l'ADC en una mostra respecte al pedestal.

Com es pot observar en la Figura 7.5, una vegada ajustats els límits del soroll electrònic la diferència entre tots dos sistemes és zero.

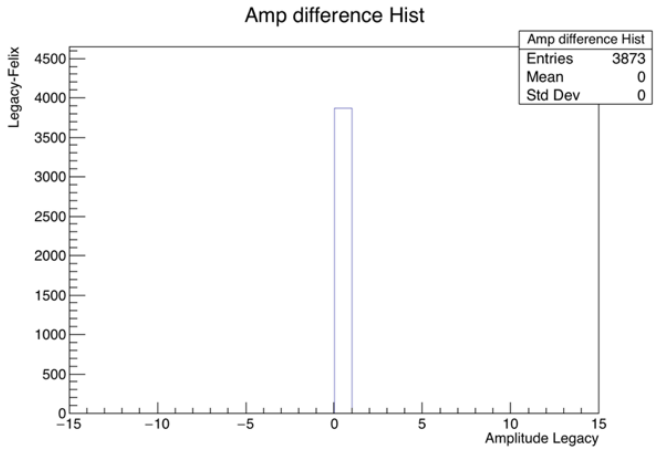

Figure 7.5: Diferències de l'amplitud reconstruïda usant Optimal Filtering entre Legacy i FELIX.

Implementació del paquet Tile Monitoring

La implementació de nova electrònica implica també nous algorismes de monitoratge. Per això s'ha desenvolupat el TileDigitsFlxMonitorAlgorithm, el qual genera histogrames per a cada canal i partició funcionant ja en el nou marc de AthenaMT.

L'algorisme genera histogrames de soroll d'alta freqüència, pedestal i distribució de mostres.

7.5 Cerca de producció de parells de bosons de Higgs en l'estat final $HH \to b\bar{b}\gamma\gamma$

En aquest capítol es presenta l'anàlisi de la cerca de producció de parells de bosons de Higgs en l'estat final $b\bar{b}\gamma\gamma$. L'anàlisi està dividida en dues parts: la cerca ressonant i la no ressonant.

La cerca ressonant està motivada per teories Beyond Standard Model (BSM) que prediuen partícules pesants que poden desintegrar-se en un parell de bosons de Higgs. El mecanisme principal que es considera en aquesta anàlisi és mitjançant ggF. D'altra banda, la cerca no ressonant està motivada per l'enteniment de l'auto-acoblament del Higgs així com la seua ràtio de producció. Per a aquesta anàlisi es consideren els dos mètodes de producció de parells de bosons de Higgs, ggF i VBF, encara que està optimitzada per a ggF ja que la seua secció eficaç és vora un ordre de magnitud major.

L'anàlisi es realitza amb totes les dades recollides durant el Run 2 per ATLAS, es a dir de luminositat integrada 139 fb^{-1} a una energia $\sqrt{s} = 13$ TeV. La selecció d'esdeveniments per a totes dues anàlisis es basa en mètodes multivariants dissenyats per a rebutjar els processos de fons.

La cerca ressonant es centra en partícules escalars d'ampladada estreta X en el rang 251 GeV $\leq m_X \leq$ 1000 GeV. Per a la cerca no ressonant els esdeveniments es divideixen en categories centrades en diferents valors de κ_λ. Els principals fons de l'anàlisi són parells de fotons i jets, i processos on un bosó de Higgs es desintegra a dos fotons.

7.5.1 Selecció d'esdeveniments

Per a la selecció d'esdeveniments de totes dues anàlisis s'utilitza una preselecció comuna que han de satisfer requisits de trigger, on es requereixen dos fotons amb un mínim de p_T de 35 GeV per al primer fotó i 25 GeV per al segon fotó. A més, es demanen els següents requisits:

- Que els fotons complisquen un criteri d'identificació "Loose" per a les dades de 2015 i 2016.
- Que els fotons complisquen un criteri d'identificació "Medium" per al període 2017-2018.
- Contindre dos fotons aillats (amb poca activitat d'altres partícles al seu voltant).
- La massa invariant del sistema de dos fotons ha d'estar en el rang 105 GeV $\leq m_{\gamma\gamma} \leq$ 160 GeV.
- El fotó amb més alt p_{T} (el segon amb més alt p_{T}) ha de satisfer la relació $p_T/m_{\gamma\gamma} \geq$ 35%(25%).
- L'esdeveniment ha de contindre exactament dos jets de tipus bottom al 77% WP.
- L'esdeveniment no pot contindre leptons (electrons, muons i tauons).
- L'esdeveniment ha de tindre menys de 6 jets centrals.

L'anàlisi és a més ortogonal a altres cerques en altres estats finals, com pot ser $HH \to b\bar{b}b\bar{b}$.

Selecció ressonant

La selecció ressonant està basada en l'ús de dos BDTs. S'han entrenat els BDTs mitjançant el kit TMVA i cadascú d'ells està dissenyat per a separar el senyal de dos fons amb diferent naturalesa: $\gamma\gamma$+jets i $t\bar{t}\gamma\gamma$ i l'altre BDT està dissenyat per a distingir el senyal de la producció d'un sol bosó de Higgs. El BDT final s'obté amb la combinació en quadratura de tots dos BDTs mitjançant l'equació 7.2:

$$\mathrm{BDT_{tot}} = \frac{1}{\sqrt{C_1^2 + C_2^2}} \sqrt{C_1^2 \left(\frac{\mathrm{BDT}_{\gamma\gamma} + 1}{2}\right)^2 + C_2^2 \left(\frac{\mathrm{BDT}_{\mathrm{Single}H} + 1}{2}\right)^2}. \tag{7.2}$$

On els coeficients C_1 i C_2 ($C_2 = 1 - C_1$) s'usen per a pesar la contribució de cada BDT. Per a cada hipòtesi de massa, m_X, es realitza un ajust en la distribució de $m_{b\bar{b}\gamma\gamma}$ seleccionant els esdeveniments entre $Mean \pm 2(4)\sigma$ (900 GeV i 1000 GeV) del ajust. Després es realitza un escaneig dels coeficients que combinen els BDTs per a trobar un coeficient comú entre totes les hipòtesis i un tall òptim en el "BDT_{score}". La Figura 7.6 mostra la distribució del BDT_{score} per a dues ressonàncies considerades.

Selecció no ressonant

Per a la selecció d'esdeveniments no ressonants els esdeveniments es divideixen en dues regions basades en $m_{b\bar{b}\gamma\gamma}$. La regió $m_{b\bar{b}\gamma\gamma} \geq 350$ GeV té com a objectiu optimitzar el senyal esperat al SM ($\kappa_\lambda = 1$), mentre que la regió de baixa massa $m_{b\bar{b}\gamma\gamma} \leq 350$ GeV cerca valors grans de $|\kappa_\lambda|$.

Es defineixen dues categories basades en la puntuació del BDT per a cada regió de massa. Les categories es defineixen maximitzant la significança en la finestra de massa 120 GeV $\leq m_{\gamma\gamma} \leq$ 130 GeV.

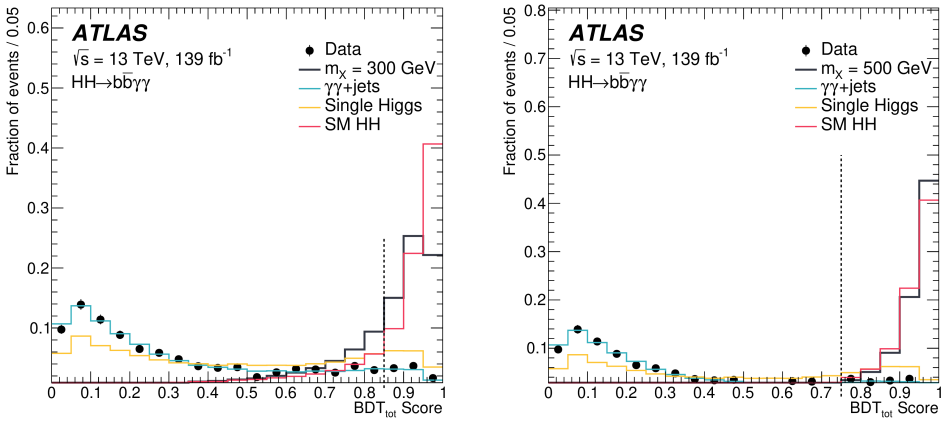

(a) (b)

Figure 7.6: $\mathrm{BDT_{tot}}$ per a les ressonàncies (a) $m_X = 300$ GeV i (b) $m_X = 500$ GeV i els seus principals fons. Les distribucions estan normalitzades a la unitat. La línia vertical de punts determina la selecció d'esdeveniments, per davall de la qual els esdeveniments són descartats. [151].

7.5.2 Parametrització de senyal i fons

El senyal i el fons s'obtenen mitjançant l'ajust de funcions analítiques a la distribució de la massa invariant dels dos fotons.

Parametrització de senyal

El senyal de parells de bosons de Higgs, així com el fons de bosons de Higgs es determina mitjançant l'ajust a mostres de dades simulades i normalitzades per la secció eficaç i per l'eficiència de selecció. La massa invariant del sistema de dos fotons es modelitza mitjançant una "Double-Sided Crystal Ball function".

Per a la cerca no ressonant la parametrització s'obté per als processos de ggF i VBF HH amb $\kappa_\lambda = 1$. En el cas de la cerca ressonant aquesta parametrització s'obté per a cada hipòtesi de massa ressonant.

Parametrització del fons

El fons es construeix a partir d'ajustar la massa invariant de dos fotons d'esdeveniments a la regió de control produïts pels processos $\gamma\gamma$+jets. Per a cada categoria de l'anàlisi es realitza un estudi per a estimar el possible "biaix" a causa de l'elecció de la funció

analítica triada, aquest "biaix" es denomina senyal espuri. De totes les funcions que es proven finalment es tria una funció exponencial.

7.5.3 Resultats

Els resultats s'obtenen mitjançant l'ajust a la distribució de la massa invariant del sistema de dos fotons. El nombre d'esdeveniments s'obté mitjançant les simulacions mentre que la força del senyal, els paràmetres del fons no ressonant i els "nuisance parameters" s'obtenen com a valors flotants en el ajust.

En cas que no es trobe excés respecte als valors esperats pel SM, es posaran límits en la secció eficaç de producció de parells de bosons de Higgs en l'estat final $b\bar{b}\gamma\gamma$. Per a totes dues anàlisis s'usara el mètode de CLs.

Resultats de la cerca ressonant

La Figura 7.7 mostra els valors esperats i observats en el límit superior en la secció eficaç de producció de partícules escalars ressonants al 95% nivell de confiança. El límit observat (esperat) varia entre 640-44 fb (391-46 fb) en el rang 251 GeV $\leq m_X \leq$ 1000 GeV.

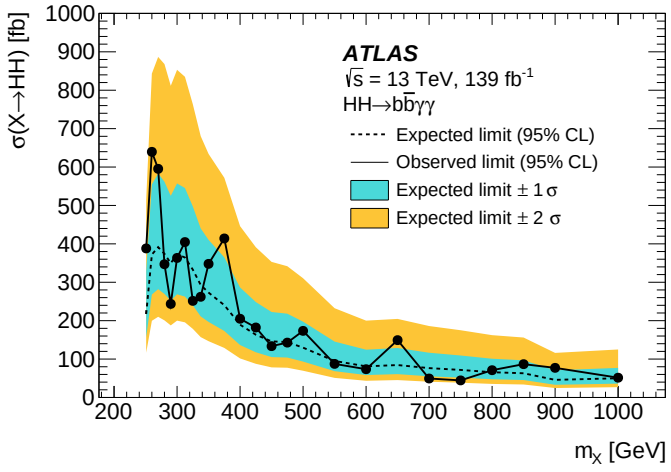

Figure 7.7: Límits observats i esperats al 95% CL en la secció eficaç de producció d'una partícula escalar "narrow-width" X en funció de la massa m_X de la partícula. La línia negra sòlida representa el límit observat. La línia de punts representa el límit esperat. [151].

Resultats de la cerca no ressonant

No s'observen excessos significatius sobre l'expextació de fons del SM, per tant, s'estableixen límits al 95% nivell de confiança en la producció de parells de bosons de Higgs. El límit al 95% observat (esperat) en el màxim del senyal és 4.1 (5.5) vegades la predicció del SM. El límits observats (esperats) en el rang de valors permesos de κ_λ és [-1.5,6.7] ([-2.4,7.7]) al 95% nivell de confiança com es mostra en la Figura 7.8.

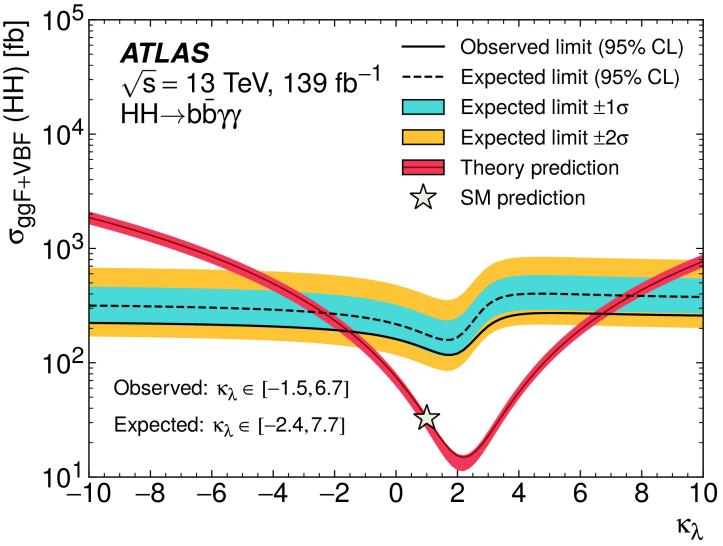

Figure 7.8: Límits observats i esperats al 95% CL en la secció eficaç de producció no ressonant de parells de bosons de Higgs en en funció del modificador d'autoacoblament del bosó de Higgs κ_λ. [151].

Conclusions

S'han realitzat cerques ressonants i no ressonants de producció de parells de bosons de Higgs en l'estat final $b\bar{b}\gamma\gamma$ amb 139 fb^{-1} de dades de col·lisions pp a $\sqrt{s} = 13$ TeV que han sigut recollits pel detector ATLAS en el LHC. Com no s'observa cap excés sobre l'expectació de fons predita pel SM es posen límits superiors.

Aquest resultat es compara amb el resultat anterior d'ATLAS en el mateix estat final amb 36 fb^{-1} respecte al qual es troben millores en la secció eficaç de produccions de parells de bosons de Higgs de fins a 5 vegades, mentre que el rang de κ_λ millora fins un factor 2. Per a la cerca ressonant el nou resultat millora entre un factor 2 i 3 depenent de la hipòtesi de massa. Aquestes millores es deuen a l'augment de la

lluminositat integrada i a la incorporació de tècniques multivariants per a la selecció d'esdeveniments, així com la millora en la reconstrucció d'objectes.

El resultat d'aquesta anàlisi es combina amb altres cerques de parells de bosons de Higgs, concretament les de $HH \to b\bar{b}\tau^{+}\tau^{-1}$ i $HH \to b\bar{b}b\bar{b}$.

La combinació no ressonant utilitza els resultats de $HH \to b\bar{b}\gamma\gamma$ i $HH \to b\bar{b}\tau^{+}\tau^{-1}$ per a establir límits en la producció de parells de bosons de Higgs al 95% nivell confiança sent l'observat (esperat) 3.1 (3.1) vegades la predicció del SM. Així mateix, s'estableixen límits en el rang de valors de l'autoacoblament del Higgs sent l'observat (esperat) $-1.0 \leq \kappa_\lambda \leq 6.6$ $(-1.2 \leq \kappa_\lambda \leq 7.2)$.

Per a la cerca ressonant es combinen les tres anàlisis obtenint els límits observats (esperats) al 95% CL entre 1.1 i 595 fb (1.2 i 392 fb) en funció de la massa ressonant m_X en el rang 251 GeV $\leq m_X \leq$ 3 TeV.

Appendix A

Resonant Selection

A.0.1 Mean and RMS calculation

A requirement for each mass hypothesis of the resonance is set on the $m^*_{b\bar{b}\gamma\gamma}$ value to select events within $\pm 2\sigma$ of the expected mean value for signal events, where σ is the standard deviation of a fit in $m^*_{b\bar{b}\gamma\gamma}$ distribution using a Crystal Ball function. In the case of the 900-1000 GeV resonance it has to be opened to Mean ± 4RMS due to the lack of background statistics. The results of the fit can be found in Table A.1.

m_X [GeV]	251	260	270	280	290	300	312.5	325	337.5	350	375	400	425
Mean	249.075	260.012	269.762	279.201	288.958	298.577	310.85	323.806	336.07	348.32	372.906	397.394	422.18
RMS	3.47843	3.13066	4.14833	5.04804	6.20036	6.70871	7.77032	7.449	8.02539	8.66209	9.75946	10.719	11.6489
m_X [GeV]	450	475	500	550	600	650	700	750	800	850	900	1000	
Mean	446.732	471.277	495.738	544.868	594.493	643.966	693.149	741.923	790.638	839.759	888.031	983.98	
RMS	12.4305	13.3335	14.1286	15.6412	16.6684	17.6277	18.8885	19.9502	21.3055	22.0929	23.4402	26.4073	

Table A.1: Mean and RMS values after the preselection using a Crystal Ball function fit.

A.0.2 BDT selection

The final BDT score of an event is obtained by the combination of the two BDT scores in quadrature in a weighted manner as can be seen in Equation A.1:

$$\mathrm{BDT_{tot}} = \frac{1}{\sqrt{C_1^2 + C_2^2}} \sqrt{C_1^2 \left(\frac{\mathrm{BDT}_{\gamma\gamma} + 1}{2}\right)^2 + C_2^2 \left(\frac{\mathrm{BDT}_{\mathrm{Single}H} + 1}{2}\right)^2}. \tag{A.1}$$

The phase space of the coefficients C_1 and C_2 ($C_2 = 1 - C_1$) and the cut on the

$\mathrm{BDT_{tot}}$ combined score is scanned to obtain the maximum binned discovery significance. The non resonant HH signal is added as part of the resonant HH signal background.

In order to be able to later perform a fit with this selection a condition of at least 0.8 events in 123-127 GeV $m_{\gamma\gamma}$window is imposed. The scan is done in a two step way. First we scan the combination of coefficients and $\mathrm{BDT_{tot}}$ that provides the maximum binned significance calculate as Equation A.2. This scan leads to a different combination of coefficients and $\mathrm{BDT_{tot}}$ cut for each resonance. Therefore a second scan is done where a common C_1 is searched for all the resonances and the loss in significance is of a maximum of 5%. The result can be seen in Table A.2.

The binned significance where σ_A^i is the Asimov significance in each bin between 120-130 GeV $m_{\gamma\gamma}$ window in bins of 1 GeV is calculated as:

$$\sum_{i=0}^{N_{\mathrm{bins}}} \sigma_{\mathrm{A}}^{i} \tag{A.2}$$

Since the fitted variable is $m_{\gamma\gamma}$ in Figure A.3 the $m_{\gamma\gamma}$ distribution for 300 GeV resonance and 500 GeV resonance is shown at preselection level and after the selection and it can be seen that the selection is not shaping the background.

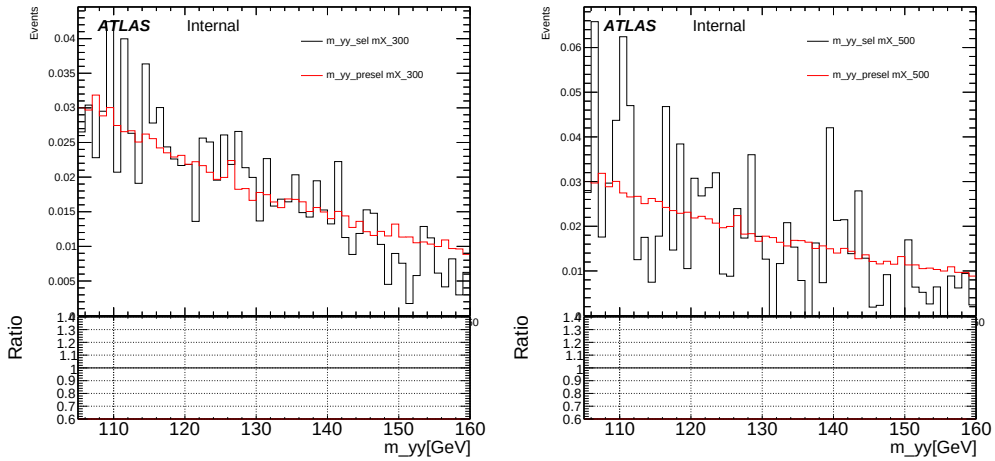

Figure A.1: $m_{\gamma\gamma}$ shape comparison for $\gamma\gamma$ continuum background in the 300 GeV and 500 GeV categories at preselection level and after the selection.

m_X [GeV]	C1	BDT cut	Signal Events	Background Events	Binned significance
251	0.65	0.70	8.73	18.56	4.26
260	0.65	0.75	7.66	40.77	2.91
270	0.65	0.80	7.11	41.97	2.57
280	0.65	0.85	6.48	32.24	2.70
290	0.65	0.85	6.59	31.91	2.69
300	0.65	0.85	6.57	28.95	2.72
312.5	0.65	0.85	6.04	28.73	2.59
325	0.65	0.85	5.22	24.43	2.65
337.5	0.65	0.85	4.85	22.19	2.50
350	0.65	0.85	4.48	19.80	2.36
375	0.65	0.90	3.71	9.17	2.48
400	0.65	0.80	4.33	14.76	2.32
425	0.65	0.85	3.38	8.52	2.14
450	0.65	0.85	2.57	6.53	1.90
475	0.65	0.80	2.58	7.35	1.83
500	0.65	0.75	2.51	7.32	1.78
550	0.65	0.60	2.52	7.34	1.81
600	0.65	0.45	1.87	9.50	1.35
650	0.65	0.30	2.03	9.97	1.49
700	0.65	0.20	1.41	10.71	1.11
750	0.65	0.20	1.48	8.64	1.28
800	0.65	0.10	1.17	10.36	0.93
850	0.65	0.03	1.19	11.93	0.95
900	0.65	0.20	1.11	8.86	0.91
1000	0.65	0.05	0.92	9.63	0.76

Table A.2: Scan on the $\mathrm{BDT_{tot}}$ for $C_1 = 0.65$. Note that only C_1 is specified since $C_2 = 1 - C_1$. For the 900-1000 GeV resonance the window has to be opened Mean ± 4RMS. Values in table are shown in the 105-160 GeV $m_{\gamma\gamma}$ window.

A.0.3 $\mathrm{BDT_{tot}}$ Score distribution

The $\mathrm{BDT_{tot}}$ distribution for all resonances are shown in Figure A.3.

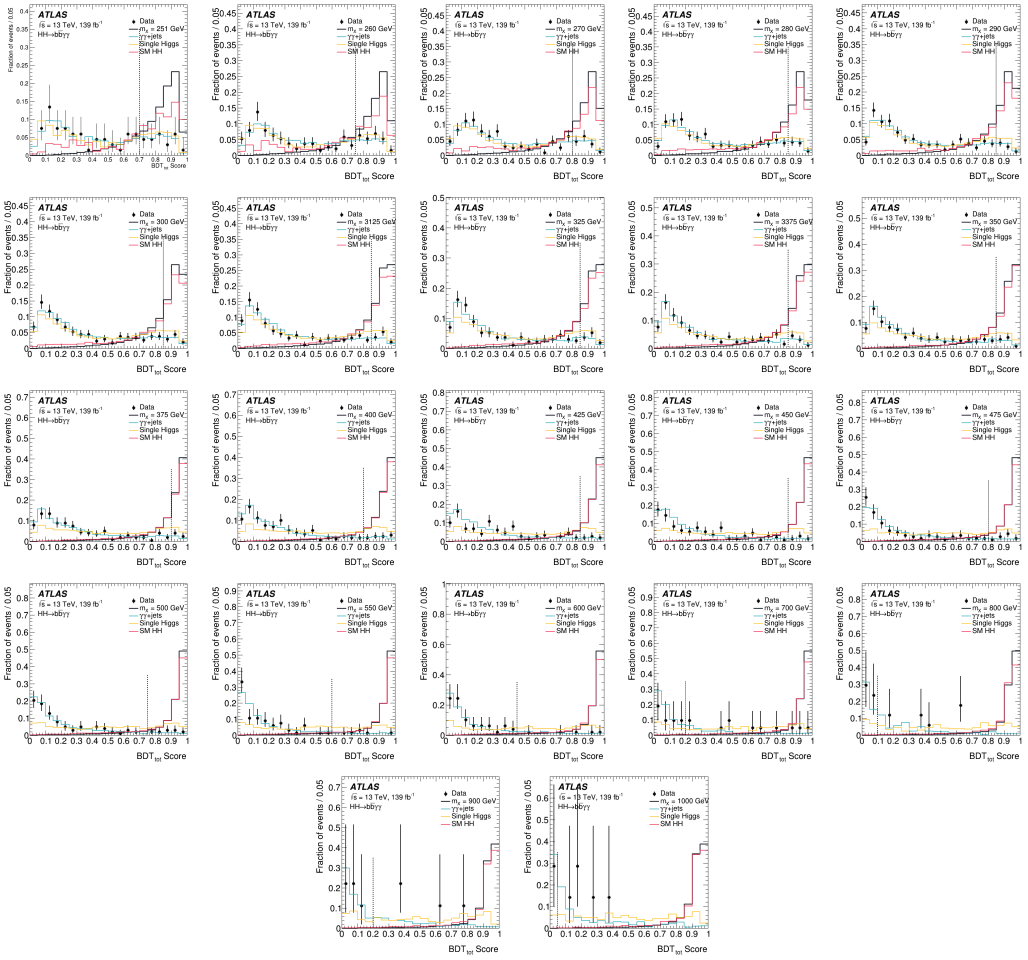

Figure A.2: $\mathrm{BDT_{tot}}$ score distribution for all resonances, m_X, at pre-selection level around the $m^*_{b\bar{b}\gamma\gamma}$ and their main backgrounds. Distributions are normalized to unit area. The dotted lines denote the event selection thresholds.

A.0.4 $m_{\gamma\gamma}$ fit

Data compared with the background-only fit for all resonant mass hypothesis are shown in Figure A.3.

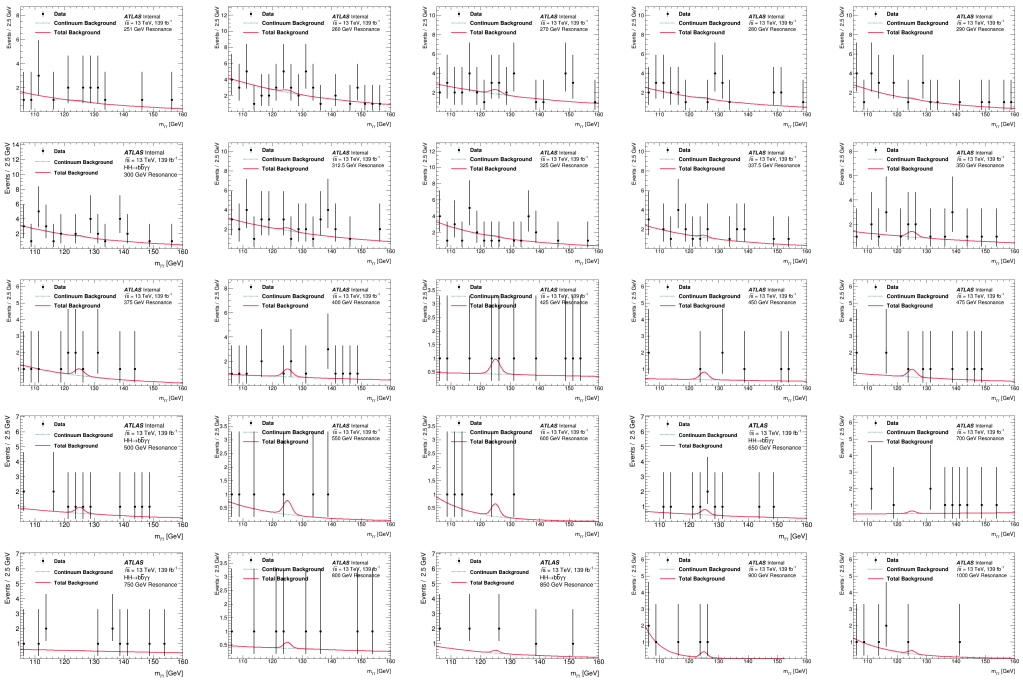

Figure A.3: Data compared with the background-only fit for all resonant, m_X, mass hypothesis. The continuum background, as well as the background from single Higgs boson production and from SM HH production, is considered.

A.0.5 Resonant limits

Observed and expected limits at 95% CL on the production cross section of a narrow-width scalar resonance X with their $\pm 1\sigma$ and $\pm 2\sigma$ variations about the expected limit due to statistical and systematic uncertainties are shown in Table A.3.

A.1 Resonance masses hypothesis above 1 TeV

The analysis is extended to resonances mass hypothesis up to 1.3 TeV justified by the small 3.0 $\sigma(2.0^{+0.4}_{-0.2}\,\sigma)$ local (global) excess observed by the $HH \to b\bar{b}\tau^+\tau^-$ [169] channel that can be seen in Figure A.4.

Therefore, the selection procedure is repeated for the mass hypothesis of 1.1, 1.2 and 1.3 TeV. For these resonance mass hypothesis the $m^*_{b\bar{b}\gamma\gamma}$ needs to be opened up to $\pm 8\sigma$. The final selection can be seen in Table A.4

The $\mathrm{BDT_{tot}}$ score distribution is shown in Figure A.5

Data compared with the background-only fit for the 1.1, 1.2 and 1.3 TeV resonant

m_X [GeV]	Exp. [fb]	Obs. [fb]	-2σ	-1σ	$+1\sigma$	$+2\sigma$
251	217.434	388.084	60.761	100.731	111.514	296.858
260	372.058	639.573	103.97	172.365	182.539	471.299
270	391.443	595.337	109.387	181.346	191.695	495.241
280	374.044	346.985	104.524	173.285	187.605	494.055
290	349.705	243.617	97.723	162.009	175.258	461.827
300	372.867	363.312	104.196	172.74	184.303	480.251
312.5	364.506	404.646	101.859	168.866	180.855	470.472
325	332.894	251.503	93.026	154.221	164.434	430.605
337.5	292.959	262.119	81.866	135.72	147.176	387.555
350	273.095	347.905	76.315	126.518	137.241	361.075
375	240.393	414.069	67.176	111.368	124.404	331.623
400	189.53	204.934	52.963	87.804	96.896	256.577
425	163.39	182.217	45.659	75.6944	85.066	227.804
450	146.039	133.674	8 40.81	67.6561	76.518	207.011
475	144.371	142.856	40.344	66.8834	73.782	197.36
500	129.719	173.434	36.2491	60.0953	67.682	180.721
550	95.108	87.4755	26.5774	44.0611	50.414	137.31
600	81.075	73.635	22.656	37.56	43.307	118.995
650	84.4136	149.297	23.589	39.1067	44.4324	120.15
700	76.4645	49.3917	40.0335	35.424	49.3917	109.555
750	71.7234	44.4765	20.0427	33.2276	37.5656	103.35
800	65.7856	71.0234	35.0524	30.4768	71.0234	96.4594
850	63.015	76.7464	17.6092	29.1932	33.7937	93.052
900	45.8839	77.1504	24.8869	21.2568	77.1504	70.1741
1000	50.0672	51.4985	26.9732	23.1948	51.4985	74.9148

Table A.3: Observed and expected limits are 95% on the production cross section of a narrow-width scalar resonance X for all m_X theoretical scalar particle. The $\pm1\sigma$ and $\pm2\sigma$ variations about the expected limit due to statistical and systematic uncertainties are also shown.

m_X [GeV]	1100	1200	1300
Mean	1076.97	1173.12	1268.54
RMS	31.7439	33.7056	36.3869
C_1	0.65	0.65	0.65
BDT cut	0.3	0.08	0.01

Table A.4: Event selection for the 1.1, 1.2 and 1.3 TeV resonance masses hypotheses.

mass hypothesis are shown in Figure A.6.

Finally, the observed and expected limits at 95% CL on the production cross section of a narrow-width scalar resonance X as a function of the mass m_X of the hypothetical scalar particle is Figure A.7 where the 1.1, 1.2 and 1.3 TeV mass hypotheses are also included.

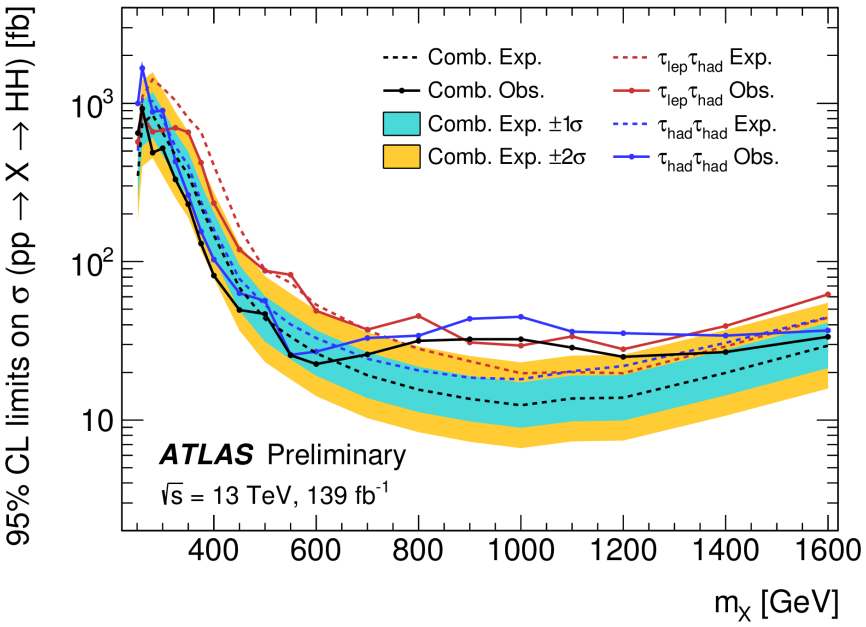

Figure A.4: Observed and expected limits at 95% CL on the cross-section of the resonant HH production as a function of the scalar resonance mass m_X. The dashed lines show the expected limits while the solid lines show the observed limits. The blue and red lines are the limits for the $\tau_{had}\tau_{had}$ channel and $\tau_{lep}\tau_{lep}$ channel, respectively. The black lines are the combined limits of the two channels. The ± 1 σ and ± 2 σ variations around the expected combined limit are indicated by the turquoise and yellow bands, respectively.

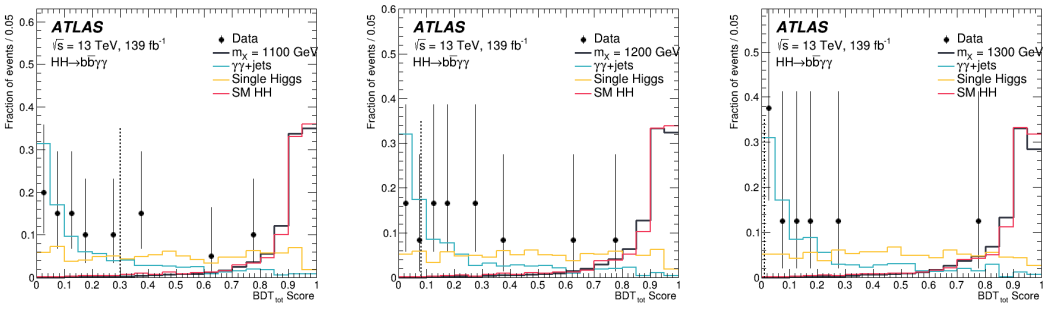

Figure A.5: $\mathrm{BDT_{tot}}$ score distribution for all resonances, m_X, at pre-selection level around the $m^*_{b\bar{b}\gamma\gamma}$ and their main backgrounds. Distributions are normalized to unit area. The dotted lines denote the event selection thresholds.

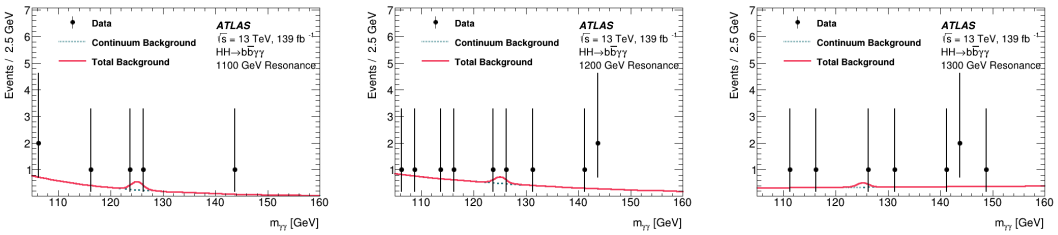

Figure A.6: Data compared with the background-only fit for $m_X = 1.1, 1.2, 1.3$ TeV, mass hypotheses. The continuum background, as well as the background from single Higgs boson production and from SM HH production, is considered.

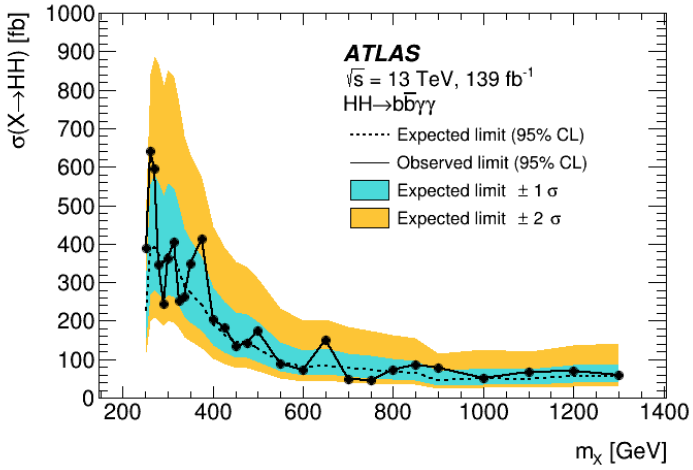

Figure A.7: Observed and expected limits at 95% CL on the production cross section of a narrow-width scalar resonance X as a function of the mass m_X of the hypothetical scalar particle. The black solid line represents the observed upper limits. The dashed line represents the expected upper limits. The $\pm 1\sigma$ and $\pm 2\sigma$ variations about the expected limit due to statistical and systematic uncertainties are also shown.

Bibliography

[1] D. Griffiths. *Introduction to Elementary Particles.* John Wiley & Sons, 1987.

[2] J. Ellis. Higgs Physics, 2013. arXiv:1312.5672 [hep-ph].

[3] A. Pich. The Standard Model of Electroweak Interactions, 2012. arXiv:1201.0537 [hep-ph].

[4] A. Djouadi. The anatomy of electro-weak symmetry breaking, 2005. arXiv:0503172 [hep-ph].

[5] C.N. Yang and R.L. Mills. Conservation of Isotopic Spin and Isotopic Gauge Invariance. *Phys. Rev.*, 96(1):191–195, October 1954.

[6] S. Bilenky. Neutrino oscillations: From a historical perspective to the present status. *Nuclear Physics B*, 908:2–13, 2016. Neutrino Oscillations: Celebrating the Nobel Prize in Physics 2015.

[7] P.A. Zyla et al. Review of Particle Physics. *PTEP*, 2020(8):083C01, 2020.

[8] S.L. Glashow. Partial-symmetries of weak interactions. *Nuclear Physics*, 22(4):579–588, 1961.

[9] A. Salam. Weak and Electromagnetic Interactions. *Conf. Proc.*, C680519:367–377, 1968.

[10] S. Weinberg. A Model of Leptons. *Phys. Rev. Lett.*, 19(21):1264–1266, November 1967.

[11] F. Englert and R. Brout. Broken symmetry and the mass of gauge vector mesons. *Phys. Rev. Lett.*, 13:321–323, Aug 1964.

[12] Peter W. Higgs. Broken symmetries and the masses of gauge bosons. *Phys. Rev. Lett.*, 13:508–509, Oct 1964.

[13] Peter W. Higgs. Broken symmetries, massless particles and gauge fields. *Physics Letters*, 12(2):132–133, 1964.

[14] ATLAS Collaboration. Measurement of the Higgs boson mass in the $H \to ZZ^* \to 4\ell$ and $H \to \gamma\gamma$ channels with $\sqrt{s} = 13$ TeV pp collisions using the ATLAS detector. *Phys. Lett.*, B784:345–366, 2018.

[15] M.E. Peskin and D. V. Schroeder. *An introduction to quantum field theory.* Addison-Wesley Advanced Book Program, USA, 1995.

[16] G. Altarelli and G. Parisi. Asymptotic freedom in parton language. *Nuclear Physics B*, 126(2):298–318, 1977.

[17] S. Alekhin et al. Fixed target Drell-Yan data and NNLO QCD fits of parton distribution functions. *Phys. Rev. D*, 74(054033), 2006.

[18] A. Pich. Quantum chromodynamics, 1995.

[19] T. Sjostrand. Monte Carlo Generators, 2006. arXiv:0611247 [hep-ph].

[20] Silvia Ferreres-Solé and Torbjörn Sjöstrand. The space–time structure of hadronization in the Lund model. *Eur. Phys. J. C*, 78(11):983, 2018.

[21] Jan-Christopher Winter, Frank Krauss, and Gerhard Soff. A Modified cluster hadronization model. *Eur. Phys. J. C*, 36:381–395, 2004.

[22] The LHC Higgs Cross Section Working Group. *Handbook of LHC Higgs Cross Sections: 4. Deciphering the Nature of the Higgs Sector.* CERN, Geneva, 2016. arXiv:1610.07922 [hep-ph].

[23] L3 ALEPH, DELPHI and The LEP Working Group for Higgs Boson Searches OPAL Collaborations. Search for neutral MSSM Higgs bosons at LEP. *European Physical Journal C - Particles and Fields*, 47(3):547–587, September 2006.

[24] The TEVNPH Working Group of the CDF and D0 Collaboration. Combined cdf and d0 upper limits on standard model higgs-boson production with up to 6.7 fb^{-1} of data. *FERMILAB-CONF-10-257-E*, 2010.

[25] ATLAS Collaboration. Observation of a new particle in the search for the Standard Model Higgs boson with the ATLAS detector at the LHC. *Phys. Lett. B*, 716(1):1–29, September 2012.

[26] CMS Collaboration. Observation of a new boson at a mass of 125 GeV with the CMS experiment at the LHC. *Physics Letters B*, 716(1):30–61, September 2012.

[27] ATLAS and CMS Collaboration. Measurements of the Higgs boson production and decay rates and constraints on its couplings from a combined ATLAS and CMS analysis of the LHC pp collision data at $\sqrt{s} = 7$ and 8 TeV. *JHEP*, 08:045, 2016.

[28] R. Frederix et al. Higgs pair production at the LHC with NLO and parton-shower effects, 2014. arXiv:1401.7340 [hep-ph].

[29] T. D. Lee. A Theory of Spontaneous T Violation. *Physical Review D*, 8(1226), August 1973.

[30] S. Dimopoulos and H. Georgi. Softly broken supersymmetry and SU(5). *Nuclear Physics B*, 193(1):150–162, December 1981.

[31] R. Grober and M. Muhlleitner. Composite Higgs boson pair production at the LHC. *Journal of High Energy Physics*, 2011(20), June 2011. arXiv:1012.1562 [hep-ph].

[32] J. Mrazek et al. The other natural two Higgs doublet model. *Nuclear Physics B*, 853(1):1–48, December 2011.

[33] M. Papucci Z. Chacko, Y. Nomura and G. Perez. Natural little hierarchy from a partially goldstone twin Higgs. *Journal of High Energy Physics*, 2006(01), January 2006. arXiv:0510273 [hep-ph].

[34] G. Branco et al. Theory and phenomenology of two-Higgs-doublet models, 2011. arXiv:1106.0034 [hep-ph].

[35] J. Baglio et al. The measurement of the Higgs self-coupling at the LHC: theoretical status. *Journal of High Energy Physics*, 1304(151), 2013.

[36] ATLAS Collaboration. Combination of searches for Higgs boson pairs in pp collisions at $\sqrt{s}$ =13 TeV with the ATLAS detector. *Phys. Lett. B*, 800:135103, 2020.

[37] CMS Collaboration. Combination of searches for higgs boson pair production in proton-proton collisions at $\sqrt{s}$=13tev. *Physical Review Letters*, 122(12), Mar 2019.

[38] Planck Collaboration. Planck 2015 results. XIII. Cosmological parameters. *Astron. Astrophys.*, 594(A13), 2016.

[39] F.J. Hasert et al. Search for elastic muon-neutrino electron scattering. *Physics Letters B*, 46(1):121–124, 1973.

[40] F.J. Hasert et al. Observation of neutrino-like interactions without muon or electron in the gargamelle neutrino experiment. *Physics Letters B*, 46(1):138–140, 1973.

[41] P. M. Watkins. Discovery of the W and Z bosons. *Contemp. Phys.*, 27:291–324, 1986.

[42] G. Baur et al. Observation of antihydrogen production in flight at CERN. *Hyperfine Interact.*, 109(1-4):191–203, 1997.

[43] Heinrich Wahl. First observation and precision measurement of direct cp violation: the experiments na31 and na48. *Physics Reports*, 403-404:19–25, 2004.

[44] G. B .Andresen,M. D. Ashkezari, Y. Yamazaki . Trapped antihydrogen. *Nature*, 2010.

[45] The ALPHA Collaboration. Confinement of antihydrogen for 1,000 seconds. *Nature*, 2011.

[46] ATLAS Collaboration. Observation of a new particle in the search for the standard model higgs boson with the atlas detector at the lhc. *Physics Letters B*, 716(1):1–29, 2012.

[47] CMS Collaboration. Observation of a new boson at a mass of 125 gev with the cms experiment at the lhc. *Physics Letters B*, 716(1):30–61, Sep 2012.

[48] L. Evans and P. Bryant. LHC Machine. *Journal of Instrumentation*, 3(08):S08001, 2008.

[49] F. Fayette. Strategies for precision measurements of the charge asymmetry of the W boson mass at the LHC within the ATLAS experiment, 2009. arXiv:0906.4260 [hep-ex].

[50] L. Evans. The Large Hadron Collider. *Philosophical Transactions of the Royal Society A*, 2012.

[51] ATLAS Collaboration, "Run 2 Luminosity Public Plots.". `https://twiki.cern.ch/twiki/bin/view/AtlasPublic/LuminosityPublicResultsRun2/`.

[52] Miroslav Myska. Inelastic proton cross section at 13 TeV with ATLAS. *PoS*, ICHEP2016:1127, 2017.

[53] ATLAS collaboration. The ATLAS Experiment at the CERN Large Hadron Collider. *Journal of Instrumentation*, 3(08):S08001, 2008.

[54] Alessandro La Rosa. The ATLAS Insertable B-Layer: from construction to operation, 2016.

[55] Karolos Potamianos. The upgraded Pixel detector and the commissioning of the Inner Detector tracking of the ATLAS experiment for Run-2 at the Large Hadron Collider. *PoS*, EPS-HEP2015:261, 2015.

[56] John Neil Jackson. The ATLAS semiconductor tracker (SCT). *Nucl. Instrum. Meth. A*, 541:89–95, 2005.

[57] ATLAS Collaboration. The ATLAS Inner Detector commissioning and calibration. *The European Physical Journal C*, 70(3):787–821, Aug 2010.

[58] ATLAS Collaboration. Public Liquid-Argon Calorimeter Plots on Detector Status.

[59] ATLAS Collaboration. ATLAS detector and physics performance: Technical Design Report, 1. Technical Report ATLAS-TDR-14; CERN-LHCC-99-014 (1999), CERN, Geneva, 1999. https://cds.cern.ch/record/391176.

[60] ATLAS Collaboration. Performance of the ATLAS trigger system in 2015. *The European Physical Journal C*, 77(5), may 2017.

[61] T. Berners-Lee. Information management: a proposal. Technical Report CERN-DD-89-001-OC, CERN, 1989.

[62] The Worldwide LHC Computing Grid. Wlcg-tiersjun14, 2016.

[63] T. Cornelissen et al. Concepts, Design and Implementation of the ATLAS New Tracking (NEWT). Technical Report ATL-SOFT-PUB-2007-007, CERN, March 2007.

[64] R.Fruhwirth. Application of Kalman filtering to track and vertex fitting. *Nucl. Instrum. Meth.*, A262:444 – 450, 1987.

[65] P. Vanlaer R. Fruhwirth, W. Waltenberger. Adaptive vertex fitting. *J.Phys.*, G34, 2007.

[66] ATLAS Collaboration. Study of the material of the ATLAS inner detector for Run 2 of the LHC. *Journal of Instrumentation*, 12(12):P12009–P12009, Dec 2017.

[67] ATLAS Collaboration. Measurements of the Higgs boson inclusive and differential fiducial cross-sections in the diphoton decay channel with *pp* collisions at $\sqrt{s} = 13$ TeV with the ATLAS detector. Technical report, CERN, Geneva, Feb 2022. 95 pages in total, author list starting page 79, 38 figures, 7 tables, submitted to JHEP. All figures including auxiliary figures are available at https://atlas.web.cern.ch/Atlas/GROUPS/PHYSICS/PAPERS/HIGG-2019-13/.

[68] ATLAS Collaboration. Electron and photon performance measurements with the ATLAS detector using the 2015–2017 LHC proton-proton collision data. *Journal of Instrumentation*, 14(12):P12006–P12006, Dec 2019.

[69] W. Lampl et al. Calorimeter Clustering Algorithms: Description and Performance. Technical Report ATL-LARG-PUB-2008-002, CERN, 2008.

[70] T Cornelissen and et al Elsing. The global 2 track fitter in atlas. *Journal of Physics: Conference Series*, 119:032013, 07 2008.

[71] ATLAS Collaboration. Measurement of the photon identification efficiencies with the ATLAS detector using LHC Run-1 data. *Eur. Phys. J. C*, 76, 2016.

[72] Leonor Cerda Alberich. Photon and electron identification with the ATLAS detector. Technical report, CERN, Geneva, Nov 2016.

[73] ATLAS Collaboration. Photon identification in 2015 ATLAS data, 2016. ATL-PHYS-PUB-2016-014.

[74] ATLAS Collaboration. Photon Identification Efficiencies using 2016 Data with radiative Z boson decays, 2016. EGAM-2016-003.

[75] ATLAS Collaboration. Topological cell clustering in the ATLAS calorimeters and its performance in LHC Run 1. *Eur. Phys. J. C*, 77, 2017. arXiv:1603.02934 [hep-ex].

[76] G. P. Salam M. Cacciari and S. Sapeta. On the characterisation of the underlying event. *JHEP*, 04, 2010. arXiv:0912.4926 [hep-ph].

[77] ATLAS Collaboration. Electron and photon energy calibration with the ATLAS detector using 2015–2016 LHC proton-proton collision data. *Journal of Instrumentation*, 14(03):P03017–P03017, mar 2019.

[78] ATLAS Collaboration. Electron and photon energy calibration with the ATLAS detector using LHC Run 1 data. *Eur. Phys. J. C*, 74(10):3071, 2014.

[79] ATLAS Collaboration. Improved electron reconstruction in ATLAS using the Gaussian Sum Filter-based model for bremsstrahlung. Technical Report ATLAS-CONF-2012-047, CERN, May 2012.

[80] ATLAS Collaboration. Electron efficiency measurements with the ATLAS detector using the 2012 LHC proton-proton collision data. Technical Report ATLAS-CONF-2014-032, CERN, 2014.

[81] ATLAS Collaboration. Electron efficiency measurements with the ATLAS detector using the 2015 LHC proton-proton collision data. Technical Report ATLAS-CONF-2016-024, CERN, 2016.

[82] ATLAS Collaboration. Electron and photon performance measurements with the ATLAS detector using the 2015–2017 LHC proton-proton collision data. *JINST*, 14(12):P12006, 2019.

[83] ATLAS Collaboration. Measurement of the muon reconstruction performance of the ATLAS detector using 2011 and 2012 LHC proton-proton collision data. *Eur. Phys. J. C*, 74, 2014. arXiv:1407.3935 [hep-ex].

[84] ATLAS Collaboration. Muon reconstruction performance of the ATLAS detector in proton–proton collision data at $\sqrt{s} = 13$ TeV. *Eur. Phys. J. C*, 76, 2016. arXiv:1603.05598 [hep-ex].

[85] J. Illingworth and J. Kittler. A survey of the Hough transform. *Computer Vision, Graphics, and Image Processing*, 44:87 – 116, 1988.

[86] G. P. Salam M. Cacciari and G. Soyez. The anti $-$ $\mathrm{k_t}$ jet clustering algorithm. *JHEP*, 04(63), 2008. arXiv:0802.1189 [hep-ph].

[87] ATLAS Collaboration. Jet energy measurement and its systematic uncertainty in proton–proton collisions at $\sqrt{s} = 7$ tev. *Eur. Phys. J. C*, 75(17), 2015. arXiv:1406.0076 [hep-ex].

[88] ATLAS Collaboration. Jet reconstruction and performance using particle flow with the ATLAS Detector. *Eur. Phys. J. C*, 77(466), 2017. arXiv:1703.10485 [hep-ex].

[89] ATLAS Collaboration. Local Hadronic Calibration. Technical Report ATL-LARG-PUB-2009-001, CERN, 2009.

[90] ATLAS Collaboration. Jet energy scale measurements and their systematic uncertainties in proton-proton collisions at $\sqrt{s} = 13$ tev with the atlas detector. *Phys. Rev. D*, 96(072002), 2017. arXiv:1703.09665 [hep-ex].

[91] ATLAS Collaboration. Jet global sequential corrections with the ATLAS detector in proton-proton collisions at $\sqrt{s} = 8$ TeV. Technical Report ATLAS-CONF-2015-002, CERN, 2015.

[92] ATLAS Collaboration. Jet Calibration and Systematic Uncertainties for Jets Reconstructed in the ATLAS Detector at $\sqrt{s} = 13$ TeV. Technical Report ATLAS-PHYS-PUB-2015-015, CERN, 2015.

[93] ATLAS Collaboration. Jet energy scale and resolution measured in proton–proton collisions at $\sqrt{s} = 13$ TeV with the ATLAS detector. *Eur. Phys. J. C*, 81(8):689, 2021.

[94] ATLAS Collaboration. JES Public Plots for Moriond 2017. Technical Report JETM-2017-003, CERN, 2017.

[95] ATLAS Collaboration. Calibration of light-flavour b-jet mistagging rates using ATLAS proton-proton collision data at $\sqrt{s} = 13$ TeV. Technical Report ATLAS-CONF-2018-006, CERN, 2018.

[96] ATLAS Collaboration. Optimisation and performance studies of the ATLAS b-tagging algorithms for the 2017-18 LHC run. Technical Report ATL-PHYS-PUB-2017-013, CERN, Jul 2017. All figures including auxiliary figures are available at https://atlas.web.cern.ch/Atlas/GROUPS/PHYSICS/PUBNOTES/ATL-PHYS-PUB-2017-013.

[97] Sebastian Heer. The secondary vertex finding algorithm with the ATLAS detector. Technical report, CERN, Geneva, Oct 2017.

[98] ATLAS Collaboration. Measurement of the c-jet mistagging efficiency in $t\bar{t}$ events using pp collision data at $\sqrt{s} = 13$ tev collected with the atlas detector, 2021.

[99] G. Aad, B. Abbott, D. C. Abbott, A. Abed Abud, K. Abeling, D. K. Abhayasinghe, S. H. Abidi, O. S. AbouZeid, N. L. Abraham, and et al. Atlas b-jet identification performance and efficiency measurement with $t\bar{t}$ events in pp collisions at $\sqrt{s} = 13$ tev. *The European Physical Journal C*, 79(11), Nov 2019.

[100] ATLAS Collaboration. Performance of pile-up mitigation techniques for jets in pp collisions at $\sqrt{s} = 8$ TeV using the ATLAS detector. *Eur. Phys. J. C*, 76(581), 2016. arXiv:1510.03823 [hep-ex].

[101] ATLAS Collaboration. Forward Jet Vertex Tagging: A new technique for the identification and rejection of forward pileup jets. Technical Report ATL-PHYS-PUB-2015-034, CERN, 2015.

[102] ATLAS Collaboration. 2015–2016 TST Systematic and Forward Pileup Suppression in MET. Technical Report JETM-2017-001, CERN, 2017.

[103] ATLAS Collaboration. Missing Transverse Momentum Distribution and Performance in 2016 data. Technical Report JETM-2016-008, CERN, 2016.

[104] G. Apollinari, O. Brüning, T. Nakamoto, and Lucio Rossi. High Luminosity Large Hadron Collider HL-LHC. *CERN Yellow Rep.*, (5):1–19, 2015.

[105] G. Barrand, I. Belyaev, P. Binko, M. Cattaneo, R. Chytracek, G. Corti, M. Frank, G. Gracia, J. Harvey, E.van Herwijnen, P. Maley, P. Mato, S. Probst, and F. Ranjard. Gaudi — a software architecture and framework for building hep data processing applications. *Computer Physics Communications*, 140(1):45–55, 2001. CHEP2000.

[106] P Calafiura, W Lavrijsen, C Leggett, M Marino, and D Quarrie. The Athena Control Framework in Production, New Developments and Lessons Learned. 2005.

[107] P. Calafiura, W. Lampl, C. Leggett, D. Malon, G. Stewart, and B. Wynne. Development of a next generation concurrent framework for the ATLAS experiment. *Journal of Physics: Conference Series*, 664(7):072031, dec 2015.

[108] ATLAS Collaboration. AthenaMT: upgrading the ATLAS software framework for the many-core world with multi-threading. *Journal of Physics: Conference Series*, 898:042009, oct 2017.

[109] Ben Wynne. Implementation of the atlas trigger within the multi-threaded software framework athenamt. *Journal of Physics: Conference Series*, 898:032002, 10 2017.

[110] Technical Design Report for the Phase-II Upgrade of the ATLAS TDAQ System. Technical report, CERN, Geneva, Sep 2017.

[111] Burkhard Schmidt. The high-luminosity upgrade of the LHC: Physics and technology challenges for the accelerator and the experiments. *Journal of Physics: Conference Series*, 706:022002, apr 2016.

[112] Peter van Gemmeren and David Malon. The event data store and i/o framework for the atlas experiment at the large hadron collider. In *2009 IEEE International Conference on Cluster Computing and Workshops*, pages 1–8, 2009.

[113] E. Fullana et al. Optimal Filtering in the ATLAS Hadronic Tile Calorimeter. 2005.

[114] T. D. Lee. A theory of spontaneous t violation. *Phys. Rev. D*, 8:1226–1239, Aug 1973.

[115] Savas Dimopoulos and Howard Georgi. Softly broken supersymmetry and su(5). *Nuclear Physics B*, 193(1):150–162, 1981.

[116] Zackaria Chacko, Yasunori Nomura, Michele Papucci, and Gilad Perez. Natural little hierarchy from a partially goldstone twin higgs. *Journal of High Energy Physics*, 2006(01):126–126, Jan 2006.

[117] J. Mrazek, A. Pomarol, R. Rattazzi, M. Redi, J. Serra, and A. Wulzer. The other natural two higgs doublet model. *Nuclear Physics B*, 853(1):1–48, Dec 2011.

[118] S. Dawson, S. Dittmaier, and M. Spira. Neutral higgs-boson pair production at hadron colliders: Qcd corrections. *Physical Review D*, 58(11), Nov 1998.

[119] S. Borowka, N. Greiner, G. Heinrich, S.P. Jones, M. Kerner, J. Schlenk, U. Schubert, and T. Zirke. Higgs boson pair production in gluon fusion at next-to-leading order with full top-quark mass dependence. *Physical Review Letters*, 117(1), Jun 2016.

[120] Daniel de Florian and Javier Mazzitelli. Higgs boson pair production at next-to-next-to-leading order in qcd. *Physical Review Letters*, 111(20), Nov 2013.

[121] Biagio Di Micco, Maxime Gouzevitch, Javier Mazzitelli, and Caterina Vernieri. Higgs boson potential at colliders: Status and perspectives. *Reviews in Physics*, 5:100045, Nov 2020.

[122] J. Baglio, F. Campanario, S. Glaus, M. Mühlleitner, J. Ronca, and M. Spira. gg→hh : Combined uncertainties. *Physical Review D*, 103(5), Mar 2021.

[123] M. Grazzini, G. Heinrich, S. Jones, S. Kallweit, M. Kerner, J. M. Lindert, and J. Mazzitelli. Higgs boson pair production at nnlo with top quark mass effects. *Journal of High Energy Physics*, 2018(5), May 2018.

[124] R. Frederix, S. Frixione, V. Hirschi, F. Maltoni, O. Mattelaer, P. Torrielli, E. Vryonidou, and M. Zaro. Higgs pair production at the lhc with nlo and parton-shower effects. *Physics Letters B*, 732:142–149, May 2014.

[125] Luca Di Luzio, Ramona Gröber, and Michael Spannowsky. Maxi-sizing the trilinear higgs self-coupling: how large could it be? *The European Physical Journal C*, 77(11), Nov 2017.

[126] Graham D. Kribs, Andreas Maier, Heidi Rzehak, Michael Spannowsky, and Philip Waite. Electroweak oblique parameters as a probe of the trilinear higgs boson self-interaction. *Physical Review D*, 95(9), May 2017.

[127] ATLAS Collaboration. ATLAS data quality operations and performance for 2015–2018 data-taking. *Journal of Instrumentation*, 15(04):P04003–P04003, Apr 2020.

[128] ATLAS Collaboration. Luminosity determination in pp collisions at $\sqrt{s} = 13$ TeV using the ATLAS detector at the LHC. Technical report, CERN, Geneva, Jun 2019. All figures including auxiliary figures are available at https://atlas.web.cern.ch/Atlas/GROUPS/PHYSICS/CONFNOTES/ATLAS-CONF-2019-021.

[129] J. Alwall, R. Frederix, S. Frixione, V. Hirschi, F. Maltoni, O. Mattelaer, H.-S. Shao, T. Stelzer, P. Torrielli, and M. Zaro. The automated computation of tree-level and next-to-leading order differential cross sections, and their matching to parton shower simulations. *Journal of High Energy Physics*, 2014(7), Jul 2014.

[130] Manuel Bähr and et al. Herwig++ physics and manual. *The European Physical Journal C*, 58(4):639–707, Nov 2008.

[131] Johannes Bellm and et al. Herwig 7.0/herwig++ 3.0 release note. *The European Physical Journal C*, 76(4), Apr 2016.

[132] Paolo Nason and Carlo Oleari. Nlo higgs boson production via vector-boson fusion matched with shower in powheg. *Journal of High Energy Physics*, 2010(2), Feb 2010.

[133] Jon Butterworth and et al. PDF4LHC recommendations for LHC Run II. *Journal of Physics G: Nuclear and Particle Physics*, 43(2):023001, Jan 2016.

[134] Xiaohu Sun, Arnaud Ferrari, Elizabeth Brost, Benjamin Tobias Rottler, Tulin Varol, Tyler James Burch, Danilo Enoque Ferreira de Lima, Yuta Sano, Petar Bokan, Bowen Zhang, Puja Saha, Katharine Leney, and Biagio Di Micco. Validation of signal Monte Carlo event generation in searches for Higgs boson pairs with the ATLAS detector. Technical report, CERN, Geneva, Feb 2019.

[135] S. Amoroso and et al. Les houches 2019: Physics at tev colliders: Standard model working group report, 2020.

[136] A. Djouadi, J. Kalinowski, and M. Spira. Hdecay: a program for higgs boson decays in the standard model and its supersymmetric extension. *Computer Physics Communications*, 108(1):56–74, Jan 1998.

[137] Tanju Gleisberg and Stefan Höche. Comix, a new matrix element generator. *Journal of High Energy Physics*, 2008(12):039–039, Dec 2008.

[138] Federico Buccioni, Jean-Nicolas Lang, Jonas M. Lindert, Philipp Maierhöfer, Stefano Pozzorini, Hantian Zhang, and Max F. Zoller. Openloops 2. *The European Physical Journal C*, 79(10), Oct 2019.

[139] F. Cascioli, P. Maierhöfer, and S. Pozzorini. Scattering amplitudes with open loops. *Physical Review Letters*, 108(11), Mar 2012.

[140] Ansgar Denner, Stefan Dittmaier, and Lars Hofer. Collier: A fortran-based complex one-loop library in extended regularizations. *Computer Physics Communications*, 212:220–238, Mar 2017.

[141] S Schumann and F Krauss. A parton shower algorithm based on catani-seymour dipole factorisation. *Journal of High Energy Physics*, 2008(03):038–038, Mar 2008.

[142] Stefan Höche, Frank Krauss, Marek Schönherr, and Frank Siegert. A critical appraisal of NLO+PS matching methods. *Journal of High Energy Physics*, 2012(9), Sep 2012.

[143] Stefan Höche, Frank Krauss, Marek Schönherr, and Frank Siegert. QCD matrix elements + parton showers. The NLO case. *Journal of High Energy Physics*, 2013(4), Apr 2013.

[144] Frank Siegert. A practical guide to event generation for prompt photon production with sherpa. *Journal of Physics G: Nuclear and Particle Physics*, 44(4):044007, Mar 2017.

[145] S. Agostinelli, J. Allison, K. Amako, J. Apostolakis, H. Araujo, P. Arce, M. Asai, D. Axen, S. Banerjee, G. Barrand, F. Behner, L. Bellagamba, J. Boudreau, L. Broglia, A. Brunengo, H. Burkhardt, S. Chauvie, J. Chuma, R. Chytracek, G. Cooperman, G. Cosmo, P. Degtyarenko, A. Dell'Acqua, G. Depaola, D. Dietrich, R. Enami, A. Feliciello, C. Ferguson, H. Fesefeldt, G. Folger, F. Foppiano, A. Forti, S. Garelli, S. Giani, R. Giannitrapani, D. Gibin, J.J. Gómez

Cadenas, I. González, G. Gracia Abril, G. Greeniaus, W. Greiner, V. Grichine, A. Grossheim, S. Guatelli, P. Gumplinger, R. Hamatsu, K. Hashimoto, H. Hasui, A. Heikkinen, A. Howard, V. Ivanchenko, A. Johnson, F.W. Jones, J. Kallenbach, N. Kanaya, M. Kawabata, Y. Kawabata, M. Kawaguti, S. Kelner, P. Kent, A. Kimura, T. Kodama, R. Kokoulin, M. Kossov, H. Kurashige, E. Lamanna, T. Lampén, V. Lara, V. Lefebure, F. Lei, M. Liendl, W. Lockman, F. Longo, S. Magni, M. Maire, E. Medernach, K. Minamimoto, P. Mora de Freitas, Y. Morita, K. Murakami, M. Nagamatu, R. Nartallo, P. Nieminen, T. Nishimura, K. Ohtsubo, M. Okamura, S. O'Neale, Y. Oohata, K. Paech, J. Perl, A. Pfeiffer, M.G. Pia, F. Ranjard, A. Rybin, S. Sadilov, E. Di Salvo, G. Santin, T. Sasaki, N. Savvas, Y. Sawada, S. Scherer, S. Sei, V. Sirotenko, D. Smith, N. Starkov, H. Stoecker, J. Sulkimo, M. Takahata, S. Tanaka, E. Tcherniaev, E. Safai Tehrani, M. Tropeano, P. Truscott, H. Uno, L. Urban, P. Urban, M. Verderi, A. Walkden, W. Wander, H. Weber, J.P. Wellisch, T. Wenaus, D.C. Williams, D. Wright, T. Yamada, H. Yoshida, and D. Zschiesche. Geant4—a simulation toolkit. *Nuclear Instruments and Methods in Physics Research Section A: Accelerators, Spectrometers, Detectors and Associated Equipment*, 506(3):250–303, 2003.

[146] ATLAS Collaboration. The simulation principle and performance of the ATLAS fast calorimeter simulation FastCaloSim. Technical report, CERN, Geneva, Oct 2010. All figures including auxiliary figures are available at https://atlas.web.cern.ch/Atlas/GROUPS/PHYSICS/PUBNOTES/ATL-PHYS-PUB-2010-013.

[147] ATLAS Collaboration. Performance of electron and photon triggers in ATLAS during LHC Run 2. *The European Physical Journal C*, 80(1), Jan 2020.

[148] ATLAS Collaboration. Electron and photon performance measurements with the ATLAS detector using the 2015–2017 LHC proton-proton collision data. *Journal of Instrumentation*, 14(12):P12006–P12006, Dec 2019.

[149] ATLAS Collaboration. Search for pair production of higgs bosons in the $b\bar{b}b\bar{b}$ final state using proton-proton collisions at $\sqrt{s} = 13$ tev with the atlas detector.

Journal of High Energy Physics, 2019(1), Jan 2019.

[150] Helge Voss, Andreas Höcker, Jörg Stelzer, and Fredrik Tegenfeldt. Tmva, the toolkit for multivariate data analysis with root. In *XI International Workshop on Advanced Computing and Analysis Techniques in Physics Research*, volume 50, page 040. SISSA Medialab, 2009.

[151] ATLAS Collaboration. Search for Higgs boson pair production in the two bottom quarks plus two photons final state in *pp* collisions at $\sqrt{s} = 13$ TeV with the ATLAS detector, 2021.

[152] Glen Cowan, Kyle Cranmer, Eilam Gross, and Ofer Vitells. Asymptotic formulae for likelihood-based tests of new physics. *The European Physical Journal C*, 71(2), feb 2011.

[153] Tianqi Chen and Carlos Guestrin. Xgboost. *Proceedings of the 22nd ACM SIGKDD International Conference on Knowledge Discovery and Data Mining*, Aug 2016.

[154] ATLAS Collaboration. Measurement of isolated-photon pair production in pp collisions at $\sqrt{s} = 7\ TeV$ with the ATLAS detector. *Journal of High Energy Physics*, 2013(1), Jan 2013.

[155] ATLAS Collaboration. Measurement of Higgs boson production in the diphoton decay channel in *pp* collisions at center-of-mass energies of 7 and 8 TeV with the ATLAS detector. *Physical Review D*, 90(11), Dec 2014.

[156] ATLAS Collaboration. Measurement of Higgs boson production in the diphoton decay channel in *pp* collisions at center-of-mass energies of 7 and 8 TeV with the ATLAS detector. *Phys. Rev. D*, 90:112015, Dec 2014.

[157] M BatiĈ, A M Paganoni, A Pfeiffer, M G Pia, and A Ribon. A new development cycle of the statistical toolkit. *Journal of Physics: Conference Series*, 396(5):052010, Dec 2012.

[158] ATLAS Collaboration. Search for resonances in diphoton events at $\sqrt{s} = 13$ TeV with the ATLAS detector. *Journal of High Energy Physics*, 2016(9), Sep 2016.

[159] Calibration of light-flavour b-jet mistagging rates using ATLAS proton-proton collision data at $\sqrt{s} = 13$ TeV. Technical report, CERN, Geneva, Apr 2018. All figures including auxiliary figures are available at https://atlas.web.cern.ch/Atlas/GROUPS/PHYSICS/CONFNOTES/ATLAS-CONF-2018-006.

[160] E. Gross G. Cowan, K. Cranmer and O. Vitells. Asymptotic formulae for likelihood-based tests of new physics. *Eur. Phys. J. C*, 71, 2011. arXiv:1007.1727 [physics.data-an].

[161] A. L. Read. Presentation of search results: the CL_S technique. *J. Phys. G*, 28, 2002.

[162] ATLAS Collaboration. Combination of searches for non-resonant and resonant Higgs boson pair production in the $b\bar{b}\gamma\gamma$, $b\bar{b}\tau^+\tau^-$ and $b\bar{b}b\bar{b}$ decay channels using pp collisions at $\sqrt{s} = 13$ TeV with the ATLAS detector. Technical report, CERN, Geneva, Oct 2021. All figures including auxiliary figures are available at https://atlas.web.cern.ch/Atlas/GROUPS/PHYSICS/CONFNOTES/ATLAS-CONF-2021-052.

[163] CMS Collaboration. Search for non-resonant higgs boson pair production in final states with two bottom quarks and two photons in proton-proton collisions at $\sqrt{s} = 13$ tev. *Journal of High Energy Physics*, 2021(3), Mar 2021.

[164] Projected sensitivity of Higgs boson pair production combining the $b\bar{b}\gamma\gamma$ and $b\bar{b}\tau^+\tau^-$ final states with the ATLAS detector at the HL-LHC. Technical report, CERN, Geneva, Feb 2022. All figures including auxiliary figures are available at https://atlas.web.cern.ch/Atlas/GROUPS/PHYSICS/PUBNOTES/ATL-PHYS-PUB-2022-005.

[165] ATLAS Collaboration. *ATLAS Technical Proposal for a General-Purpose pp experiment at the Large Hadron Collider at CERN*. CERN, Geneva, 1994. CERN-LHC-94-43.

[166] CMS Collaboration. *Technical Proposal*. CERN, Geneva, 1994. CERN-LHCC-94-38 ; LHCC-P-1.

[167] LHCb Collaboration. *LHCb: Technical Proposal*. CERN, Geneva, 1998. CERN-LHCC-98-004; LHCC-P-4.

[168] ALICE Collaboration. *ALICE : Technical proposal for a Large Ion collider Experiment at the CERN LHC*. CERN, Geneva, 1995. CERN-LHCC-95-71; LHCC-P-3.

[169] ATLAS Collaboration. Search for resonant and non-resonant Higgs boson pair production in the $b\bar{b}\tau^{+}\tau^{-}$ decay channel using 13 TeV pp collision data from the ATLAS detector. Technical report, CERN, Geneva, Jul 2021. All figures including auxiliary figures are available at https://atlas.web.cern.ch/Atlas/GROUPS/PHYSICS/CONFNOTES/ATLAS-CONF-2021-030.